Fracture Characterization of Wood Adhesive Joints

Wernersson, Håkan

1994

Document Version:
Publisher's PDF, also known as Version of record

[Link to publication](#)

Citation for published version (APA):
Wernersson, H. (1994). *Fracture Characterization of Wood Adhesive Joints*. Division of Structural Mechanics, LTH.

Total number of authors:
1

FRACTURE CHARACTERIZATION
OF WOOD ADHESIVE JOINTS

HÅKAN WERNERSSON

FRACTURE CHARACTERIZATION
OF WOOD ADHESIVE JOINTS

HÅKAN WERNERSSON

To

Eva, Karl, Ragnar
and Gunnar

ACKNOWLEDGEMENTS

Lund in April 1994

Håkan Wernersson

ABSTRACT

Failure in wood is commonly considered as a sign of properly chosen adhesive for wood adhesive joints. It is argued that as the adhesive is stronger than the surrounding wood material, no concern has to be given to the adhesive properties in joint design. However, by means of theoretical arguments in combination with experimental experience in the present study, it is stated that local bond line properties are of great consequence to global joint load capacity, also in case of failure in wood. Furthermore, it may be concluded that for many joints, optimal strength can be expected if the failure is located in the adhesive material instead of the surrounding wood material.

A nonlinear fracture mechanics model, including gradual softening, for strength analysis of adhesive joints is presented. It is a unified theory which incorporates linear and nonlinear elastic analysis as well as conventional stress criteria and linear elastic fracture mechanics as special cases. Closed-form solutions are given for pure shear analysis. For mixed-mode a coupled deformation based model is developed which exhibits path-independence in stresses but path-dependence in fracture energy. The model is implemented in a finite element code and used for analysis of some of the proposed test specimens in-glued steel plates and for a parametric study of finger joints. A major outcome is that both local bond strength and fracture energy are of importance in strength evaluation of regular wooden joints.

The complete stress-deformation curve for bond lines is determined for pure shear, pure tension perpendicular to the bond line and in mixed-mode. To perform stable tests for brittle adhesives, large demands are placed on the test specimen, setup and testing machine. New small size material test methods have been developed with emphasis on stiffness and on uniform and univocal stress states. In the material test series resorcinol/phenol, PVAc and one-component polyurethane were used.

Larger specimens to verify and to study fracture propagation are developed in the study. For the adhesives used in the test programmes, failure in wood occured more frequently for increased amount of peel stresses. This make the evaluation more complicated, as the fracture energy is a mixture of wood and adhesive properties and as the fracture area may be difficult to determine. In shear-dominated failure processes the correspondence between calculated and experimental results is good.

NOTATIONS

Notations and symbols are explained in the text when they first occur. In addition, a list of main notations is given below in SI-units:

A	area	$[m^2]$
b	bond width	$[m]$
b'	adherend width	$[m]$
C	compliance	$[m/N]$
c	displacement ratio, δ_s/δ_n	$[-]$
D	stiffness variable	$[Pa/m]$
E	Young's modulus	$[Pa]$
E_w	Young's modulus of wood	$[Pa]$
G	energy release rate	$[Nm/m^2]$
G_c	critical energy release rate	$[Nm/m^2]$
G_f	fracture energy	$[Nm/m^2]$
G_{fn}	fracture energy in normal direction	$[Nm/m^2]$
G_{fs}	fracture energy in shear direction	$[Nm/m^2]$
G_w	shear modulus of wood	$[Pa]$
J_c	critical J-integral	$[Nm/m^2]$
K	stress intensity factor	$[Pa/\sqrt{m}]$
K_c	critical stress intensity factor	$[Pa/\sqrt{m}]$
ℓ	length	$[m]$
ℓ_{ch}	characteristic length	$[m]$
ℓ_e	element length	$[m]$
ℓ_{fr}	length of the fracture zone	$[m]$
M	moment	$[Nm]$
m, n	powers in strength criteria	$[-]$
N	normal force	$[N]$
P	applied load	$[N]$
t	thickness	$[m]$
u	horizontal displacement	$[m]$
V	volume	$[m^3]$
v	vertical displacement	$[m]$
W	external energy	$[Nm/m^2]$
w_s	strain energy function	$[Pa]$

α	adherend stiffness ratio	[-]
β	crossectional parameter	[-]
γ	boundary condition factor	[-]
δ	displacement	[m]
δ_n	normal displacement	[m]
δ_s	shear displacement	[m]
$\delta_{nk,a}$	breakpoint on the multi-linear $\sigma - \delta_n$ curve for a given ψ	[m]
$\delta_{sk,a}$	breakpoint on the multi-linear $\tau - \delta_s$ curve for a given ψ	[m]
ϵ	strain	[%]
ϵ_ℓ	longitudinal strain in bond element	[%]
ν	Poisson's ratio	[-]
σ	stress	[Pa]
σ_f	local normal strength	[Pa]
τ	shear stress	[Pa]
τ_f	local shear strength	[Pa]
Φ	strain energy	[Nm]
ψ	mixed-mode angle	[°]
ψ_b	bond line mixed-mode angle	[°]
ψ_G	fracture energy based mixed-mode angle	[°]
ψ_g	global mixed-mode angle of the test setup	[°]
ψ_K	stress intensity based mixed-mode angle	[°]
ω	brittleness ratio	[-]

CONTENTS

1. INTRODUCTION

1.1. General Remarks

1.1.1. Development of adhesive technology

Adhesive bonding is an old skill which has been practiced by man since the birth of civilization. Numerous natural materials are characterized by their tacky performance, such as clay, wax, resin, egg, etc. These were used for various purposes, producing e.g. tools or ornaments in the primitive household.

In early days man learnt how to produce adhesives from natural waste products like animal bones and skin. During the Egyptian era, skilled craftsmen produced laminated articles of worship and furniture with animal based adhesives of the same type still used in many handicraft applications [77]. What we refer to today as structural adhesives were first produced from casein, a waste product in the dairy industry. These were used in the early glulam industry, and there are numerous examples of structures built with this technique, e.g. the great halls of many railway stations with glued laminated beams as load bearing structure, built at the beginning of the century. After many years of service these large glulam beams and arches exhibit little or no sign of deterioration.

The modern cross-linked adhesives used for structural applications have, with few exceptions, been developed during the present century. The pioneers were found in the airplane industry where the diverse advantages of adhesive bonding were recognized. The airplane industry is still considered as a frontier in the development of structural adhesive technology. In this progress, the properties of the adhesive are allowed to play an active part in structural design. However, as the airplane industry abandoned wood as the major structural material in favour of aluminium, and more recently, composites, the development of the wood glueing industry has, from a mechanical point of view, stagnated.

Large efforts have, however, been made to improve durability, glueing performance and other important but more chemistry related qualities, since the development of wood adhesive technology is almost extensively run by chemists. In this development the governing strength criterion has, in general, not been to optimize the total joint or the bonded structure, but from some standardized test try to ensure a sufficient strength of the bond line. If such a test is passed it has been argued that further concern about bond line properties would be unnecessary in joint design. In contrast to this it will be stated in this report that there are other

3

bond line mechanical properties than strength that are often of greater significance for the load carrying capacity of a joint.

1.1.2. Wood and adhesive joints

Wood fulfills many of the requirements made on modern materials. It has a nice appearance , is easy to work with and it is a renewable natural resource. Additionally, wood has a reasonable price, a low weight in comparison to its strength and favourable fatigue properties [11]. In spite of this, wood is regularly more associated with unfavourable qualities such as sensitivity to moisture changes, insufficient durability, cracking and relatively large deviations in mechanical properties, which has resulted in large safety margins in the building codes and to some extent caused a general lack of confidence in wood as a structural material. However, this lack of confidence and emphasis on disadvantageous qualities only reflects the need for research in the area of wood science and technology.

Correspondingly, this may also be true for structural adhesive wooden joints. They offer a number of favourable qualities, but their reliability is frequently questioned. Again this may be interpreted as a need for research on properties, modelling and structural analysis. In order to widen the applicability and to fully utilize their favourable qualities, wood adhesive joints should be recognized as highly technological, demanding skilled design and craftsmanship.

There are some factors that in certain situations may be considered as disadvantageous in using adhesive fasteners. One is the toxicity of many adhesives, involving problems in the working environment; another is that adhesive bonds need curing pressure and, probably more important, curing time, and a third is that it is generally difficult to dismantle a glued connection in a gentle manner.

Fig. 1.1 exhibits four different situations in which adhesive joints may be used. Adhesive bonding can be one of several methods of fastening, as for the various lap joints given in Fig. 1.1a. The glued joint will in comparison to various mechanical joints reveal a more rigid behaviour.

Fig. 1.1b illustrates situations where adhesives may be considered as principally the only adaptable bonding agent. Similar components produced with alternative fasteners will not obtain comparative performance characteristics.

Adhesive bonds yield high stiffness to the bonded component compared to mechanical fasteners. In many cases, such as the lightweight beam and the floor structure in Fig. 1.1c, stiffness properties of a component may be of great importance in design. From a strength evaluation point of view, the bond line in the floor structure might often not be considered the critical point in design; however, the bond line may, in case of glueing, significantly increase the composite action of the beam and the board, inferring considerably larger stiffness of the floor.

A fourth application of adhesive bonding technique is to use the adhesive joint as a reinforcement, illustrated in Fig. 1.1d. Additional materials of wood, steel, fibres, etc. can be joined to highly stressed parts of a structure, or even more interesting,
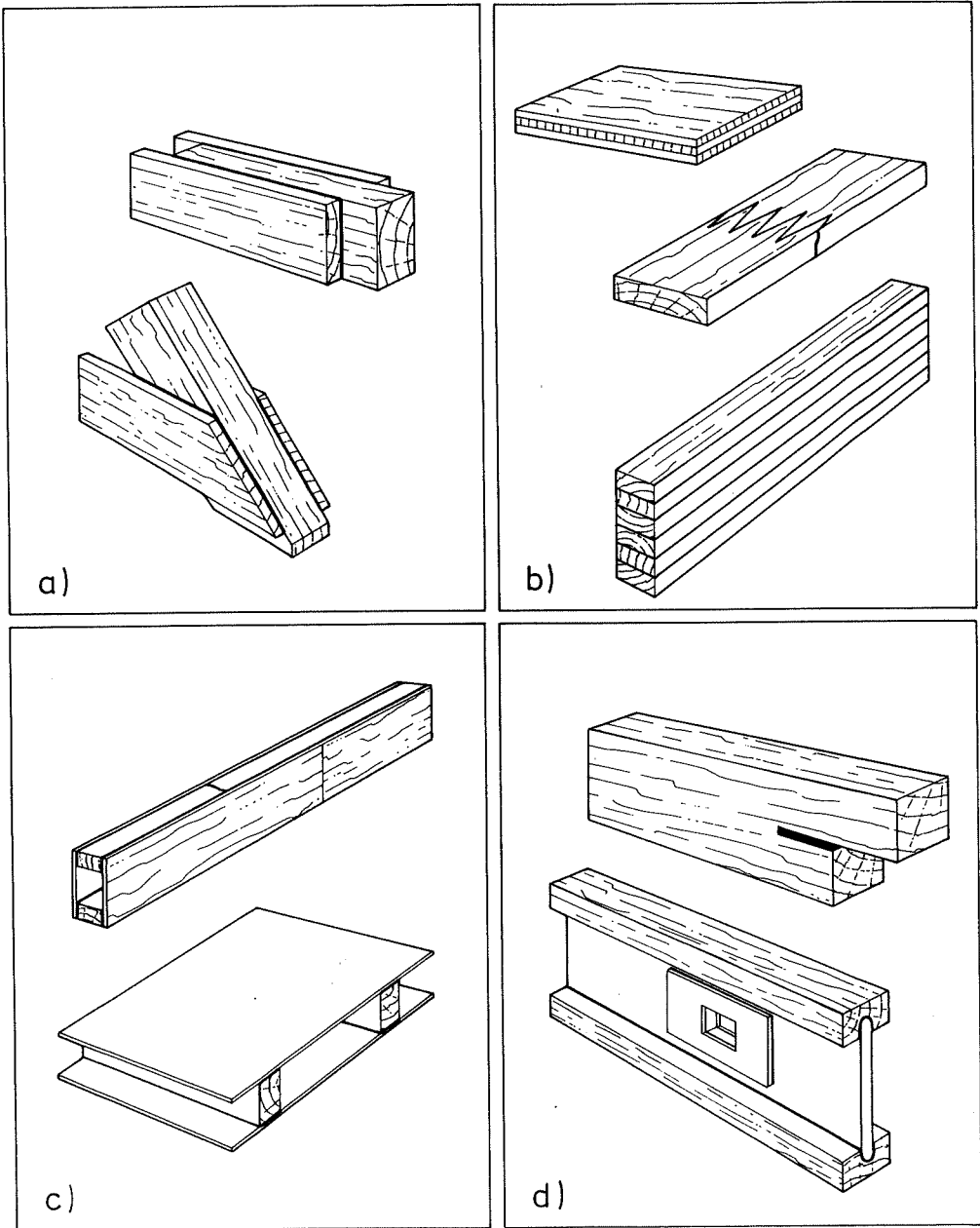
Figure 1.1: *Various applications of adhesive bonding. The bond line may serve as;* a) *an alternative to other types of fastener* b) *the only fastener adaptable* c) *a stiffener, by supplying increased composite action* d) *reinforcements.*

the bond line itself may act as a reinforcing agent. Stress concentrations in the notch of the beam can be more evenly distributed if a kerf is made in the notch and filled with a rather ductile adhesive. *Suzuki* and *Sasaki* [91] report that a small kerf filled with toughened epoxy at the notch apex approximately doubles the maximum load capacity of notched beams.

Using adhesive bonding, where in the design the bond line is allowed to play a more active part in the structural performance, may decrease the effect of deviation in wood components and strengthen wooden structural elements. Adhesive bonded wood elements do have a large potential as high technological, lightweight, strong and fatigue-resistant products, to be used and relied on in many demanding situations.

1.2. Components of Adhesive Bond Lines

At first sight an adhesive joint may be considered as being composed of only three components, the two adherends and the adhesive, cf. Fig 1.2. However, a closer look reveals that the bond layer is constituted of several characteristic zones, including interface layers between the adhesive and the adherend.

Preparing a wooden joint, the first thing to be done is to cut the wood blocks into the required size. Cutting wood infers damage to the surface, broken or loose fibres, burns, stains, etc. Planing the surface will likely make the surface smoother and more uniform, which will improve the gluability. The next step is to apply the adhesive. This should be done as soon as possible to prevent airborn dirt from staining the surface and preventing natural oils, resins, etc., within the wood material from migrating to the surface. The penetration of the adhesive depends on its viscosity in combination with the wettability of the wood surface and also on the amount of adhesive applied. The curing mechanisms are quite distinct for different types of adhesive; one-component types cure by emitting or absorbing moisture and solvents from the surrounding, while typical two-component adhesives interact with the adherend surface only to a minor extent.

The finished joint consists of two adherends joined by a thin adhesive layer. Although thickness is in the range of only 0.1 to 0.5 mm, the bond line may have properties that completely govern the performance of the joint, also for very strong joints. Additionally, bond line properties may extensively depend on the characteristics of a nearly infinitely thin interfacial layer, or the very extreme wood fibre layer, with a thickness of maybe a thousandth of a millimeter. Accordingly, it is appropriate to determine bond line properties in situ, including the interfaces, which may then be a function of e.g. the wood species or surface preparation of the adherends.

Adherend 1 | Adhesive | Adherend 2
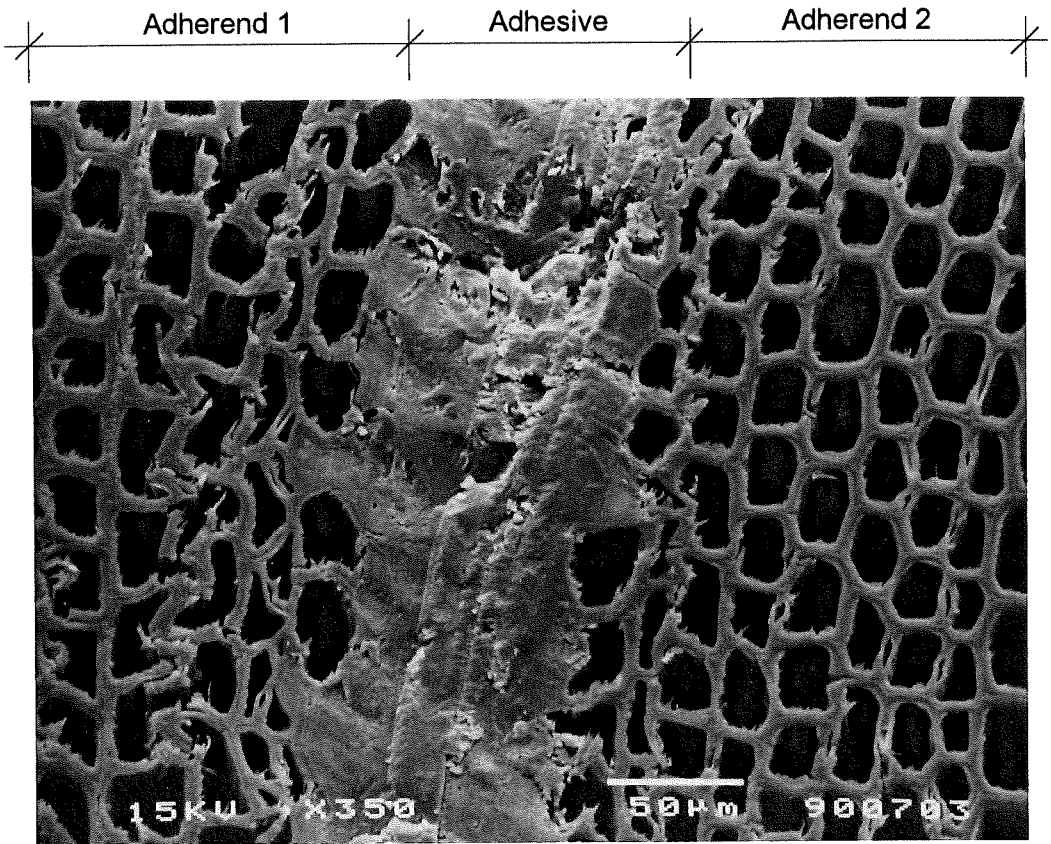
Figure 1.2: *A wood adhesive bond line. Scots Pine and resorcinol/phenol.*

1.3. Topic

The development in adhesion science and technology is mainly conducted by chemists, which may seem in order, since adhesive properties are matters of chemical compound, choice of constituents, degree of cross linking, etc. For the adhesive manufacturer, sales are promoted by topics such as applicability, handling, working environment, cost, wear on machinery, etc. Mechanical properties are commonly implied as the manufacturer vouches that adequate strength according to valid codes are fulfilled. Adequate strength is generally referred to as a sufficiently high value of the failure load of a joint with standardized geometry or, alternatively, that the failure of a tested joint is localized to the adherends, i.e. wood failure.

The estimate of strength for many standard test joints is only valid for the joint actually tested. If the results are to be generalized to some other geometry, the outcome may be rather different, with much lower strength than expected. Addi-

tionally, for a large number of joints, local bond strength is no proper bond line parameter for determination of the load capacity of a joint. Instead, some measure of energy dissipation at failure will be the most important bond line factor.

The often unexpected performance of adhesive joints may to a large extent be explained by the lack of sufficient fracture mechanics knowledge in joint design. The difficulties of predicting strength of bonded components and structures followed by unexpected failures will undermine the reliability of adhesives as bonding agents. This is serious, as adhesively bonded wood structures have a large potential. Accordingly, this should be a concern not only for the adhesive manufacturers, but to an even larger extent for the wood industry.

There is a pronounced need for improved knowledge of the mechanical behaviour of adhesive joints, which should be a task for structural engineers. Thorough investigations have to be performed to find proper methods for analysing joints and to determine which bond line properties are of significance in joint design. Such methods should involve fracture mechanics in one way or another. In addition, new testing methods have to be developed to facilitate an accurate determination of such material properties.

A general objective of this thesis is to contribute to the progress of developing new knowledge on mechanical behaviour of adhesive joints. The results presented are intended to provide more realistic and accurate approaches for analysis and design of bonded joints and, hence, contribute to the promotion of the use of adhesive bonding in wood structural design.

1.4. Scope

This thesis is a further development of an earlier report *"Wood Adhesive Joints - Fracture softening properties in shear and in tension"* [98]. This previous report dealt with properties in pure shear and pure tension perpendicular to the bond line. The present work has been expanded to also include mixed-mode material models and analysis. Major parts of the earlier report are included in this publication.

The objective of this report is, in general terms, to elucidate the importance of appropriately considering adequate bond line properties in the design of adhesive joints. A minimum bond strength criterion is generally insufficient. Different strategies for joint analysis, including stress analysis but with emphasis on fracture mechanics analysis, are discussed. In addition, a nonlinear fracture mechanics approach is presented which involves conventional stress criteria and linear fracture mechanics as special cases. Existing test methods for evaluation of mechanical characteristics of bonds are briefly discussed, and new better-adapted test methods to determine and verify bond line material models in shear, tension and in mixed-mode are proposed and evaluated.

The tests as well as the theoretical analyses are restricted to short term mechanical behaviour during monotonical loading. Consequently, duration of load,

climate, environmental aspect, and effects of cyclic loading, etc., are if considered only treated to a minor extent. The concept of the present research is new, and may in the future be generalized to include e.g. creep and moisture effects.

Different adhesives have been used in the test programme. The choice of adhesives was primarily not an attempt to find the most commonly used or the "best" glues. Instead, as the chemical composition, curing mechanisms, ductility, etc., of the chosen adhesives are quite different, they are expected to cover a wide span of wood adhesives on the market.

Except for the small tension test series, the wood species used was Scots Pine (Pinus sylvestris). In the tension series, Beech (Fagus sylvatica) was chosen as adherend material in order to reduce the amount of wood failure.

Theoretical analysis and methods for material modelling are in principle not restricted to a specific choice of adhesive and adherend material. Accordingly, the analysis, modelling and, to a major extent, also the test methods presented may also be relevant for other types of materials than wood.

1.5. Overview of the Present Work

1.5.1. Overall characterization of adhesive joints

The mechanical characteristic of a material is determined by its chemical compound and composition, which in turn is dependent on the physical condition during curing as well as the environment in which it is supposed to act. From a practical point of view it is, however, not possible to perform a direct translation of micro scale, chemical composition into mechanical properties of full-size structural members. To evaluate mechanical properties of a material it is commonly more convenient to act at some intermediate level of scale. A hierarchic, micro to macro scale system of material properties applied to adhesive bonding is given in Fig. 1.3.

The response of a full-scale structure, for example an adhesively bonded roof truss, is possible to calculate if the mechanical properties of the components are well defined. The quality of the joint can be experimentally determined for the geometry and load case to be expected for the structure. With a proper method of analysis it may, however, more conveniently be determined from known bond line and adherend characteristics. In this manner the properties of an arbitrary joint can be established. Correspondingly, bond line characteristics may be determined from experiments or, by descending one level in the scale and by methods of analysis, evaluating the requested properties from known qualities of the bulk material and the interface of the two materials. Finally, the adhesive bulk properties will be a function of the chemical composition and the physical conditions involved.

The mechanical properties in adhesive wood bonding are usually experimentally determined as joint characteristics at the fourth level in Fig. 1.3. The results are then often generalized to be valid for joints with other geometry and possibly with other adherend materials to be comprised in some full-size bonded structure.
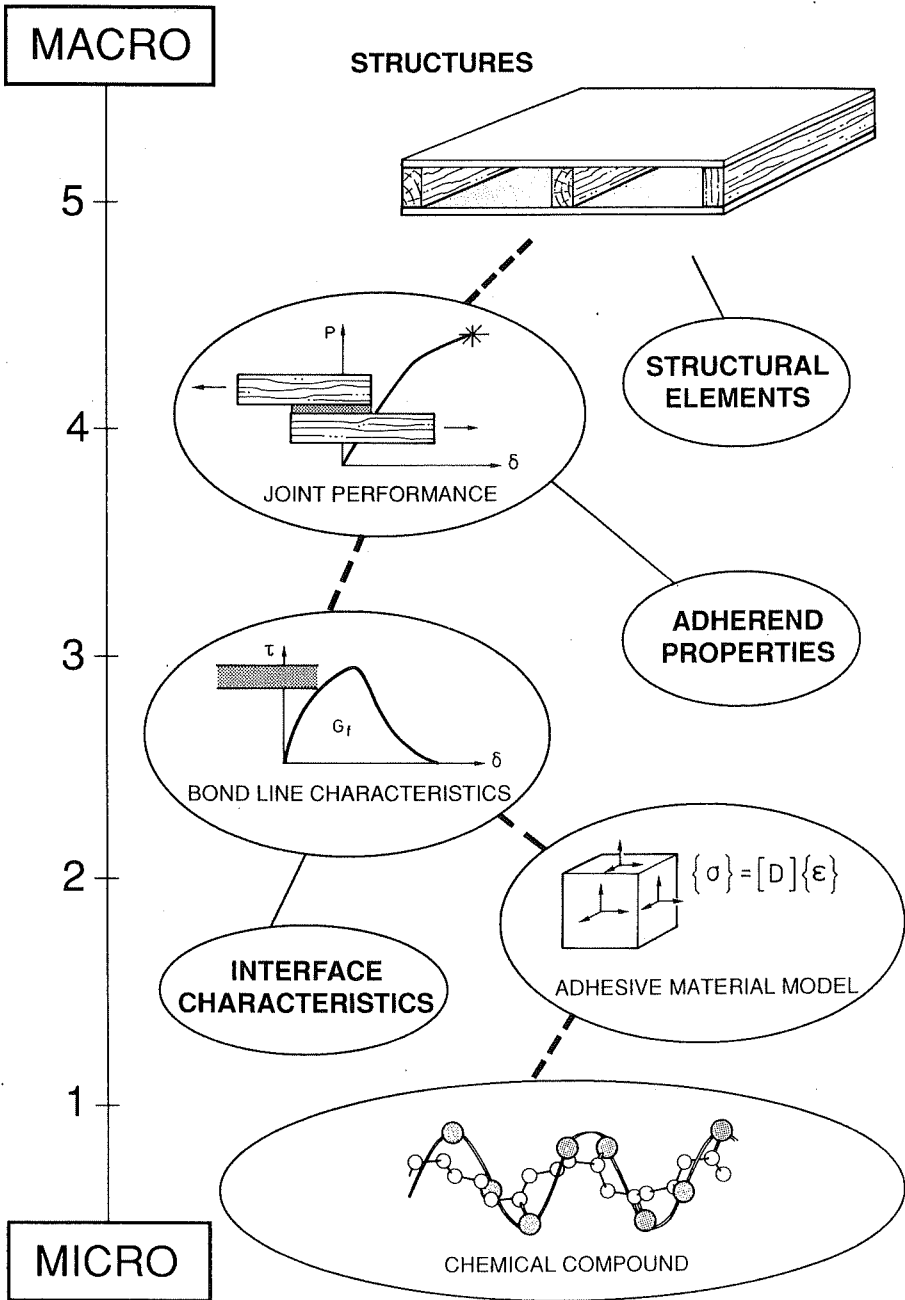
Figure 1.3: *System levels for characterization of mechanical properties in adhesive bonding design.*

Recordings from the most common joint tests are, however, generally not possible to straightforwardly transform into some measure of material quality.

In structural mechanics the material is usually modelled as a continuum on level 2. However, in accordance with the previous discussion it is doubtful whether a bond line should be considered to be a continuum and, furthermore, strain instability and localization within the bond line may cause numerical difficulties if the bond line is considered to be a continuum. In the present report, the characterization of mechanical properties is focused on level 3, i.e. on the bond line. These properties will be influenced by parameters such as bond thickness, adherend material, surface treatment, etc. With a proper bond line model, this infers the feasibility of accurately calculating the response of an arbitrary thin joint.

1.5.2. Strategy

The strategy that forms the base of the present study is illustrated in Fig. 1.4 where the system levels correspond to those in Fig 1.3. The bond line properties are governed by chemical composition and are also influenced by physical conditions such as curing condition, loading history, duration of load, age, moisture, temperature, etc. There are no proper test methods available for direct determination of the requested properties, i.e. stress-deformation relations of bond lines. These properties are therefore evaluated from global mechanical response of joints, tested at different constant physical conditions. The specimens are designed to facilitate a rather simple procedure of transforming joint response into bond line properties.

To verify the results, the first step is to use the bond line model obtained to calculate the response of the specimen. The result from such a calculation should coincide with the experimental results to verify the method of evaluation. The second step is to prove the generality of the model. This is done by tests on full-scale joints on which proper methods of analysis have been applied to determine the load-displacement response. If there is agreement between calculated and experimental results, the bond line model may be considered as verified.

1.5.3. Disposition of the report

In Chapter 2 methods of fracture analysis are discussed. A brief discussion of conventional methods with emphasis on fracture mechanics is given. The main feature is the presentation of a coupled mixed-mode non-linear fracture mechanics model for analysis of adhesive joints.

Chapter 3 deals with test methods. Stable fracture performance in relation to testing machines and standard test specimens are discussed, and for some specimens the stress distribution along the bond line is analysed. However, as a main topic, new methods for evaluation and verification of non-linear fracture mechanics bond line properties are presented. The test programme includes six major test specimens. Three methods are given for determination of the complete stress-deformation rela-

LEVEL

MACRO

STRUCTURE
5

JOINT
4

| P - δ RESPONSE OF SPECIMEN |

TESTS OF FULL
SIZE JOINTS

b   c

c

BOND LINE
3

| REPRESENTATION OF τ - δ RELATION OF BOND LINE |

a

ADHESIVE +
INTERFACE
2

ADHESIVE
CONSTITUENTS
1

| CHEMICAL COMPOSITION AND PHYSICAL CONDITIONS |

MICRO
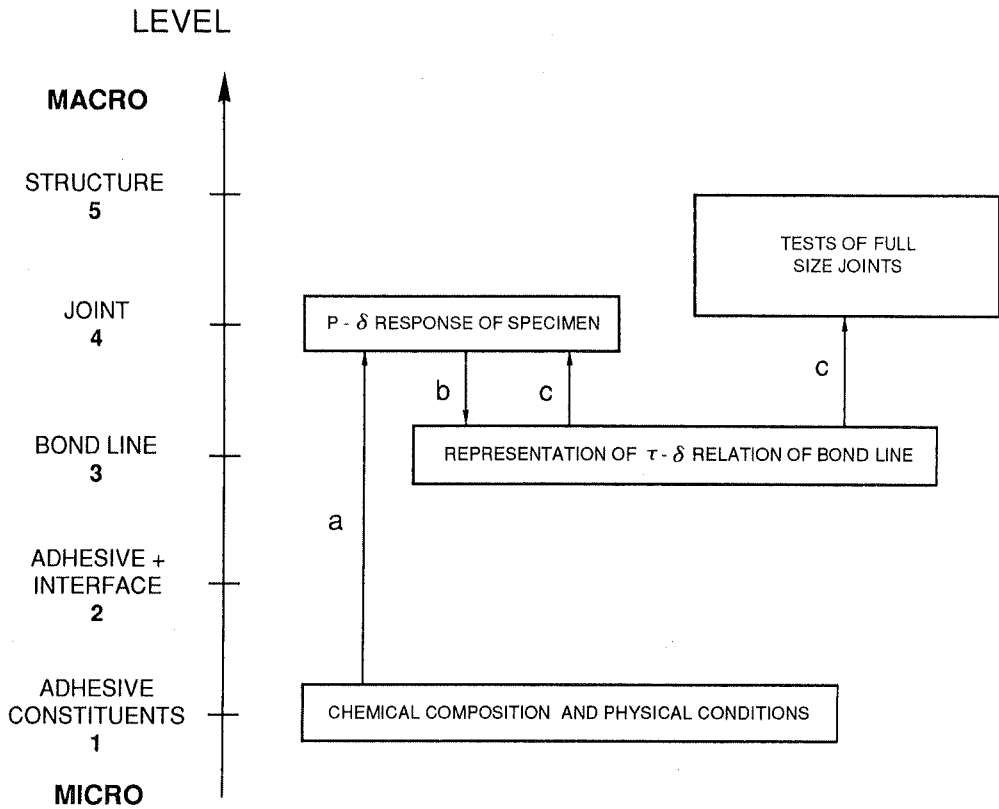
Figure 1.4: *Strategy of the present study by means of; a) testing methods, b) evaluation methods and c) calculation methods.*

tions, in pure shear, in pure tension and in mixed-mode. In addition, specimens are given for verification or crack propagation tests in the corresponding modes. Test results are presented and discussed in Chapter 4.

Numerical analysis is the topic of Chapter 5. The finite element implementation of the mixed-mode bond line model is presented. Analyses on different applications are given with emphasis on the bond line characteristics. The strengths of different standard finger joints are calculated and a parametric study of the influence of different material and geometrical properties on the finger joint strength is given. In the same manner a set of steel to wood joints is studied.

Conclusions and final remarks are found in Chapter 6, including a discussion of the influence of bond properties on joint strength and future research needs.

2. METHODS OF FRACTURE ANALYSIS

2.1. General Remarks

2.1.1. Definitions

In the following a *joint* is considered to be the entire connection, i.e. composed of the bonding agent and the materials to be joined, which are called the *adherends*. The *adhesive* is the applied glue material, and the *bond line* includes the adhesive as well as the interface between the adhesive and the adherends. In Fig. 2.1 the geometry of a typical single lap joint is given.

2.1.2. Methods of analysis

What may be regarded as the first analyses of adhesive joints are those of *Bleich* [10] in 1924 and *Volkersen* in 1938 [94]. They analysed the shear force distribution of a riveted joint by modelling the rivets as an elastic layer followed by an integration of the shear stress neighbouring each rivet. In the analysis they assumed the bond line to be a linear elastic shear medium and the adherends to be pure tension bars. The theory yields very pleasant solutions and it exposes surprisingly good validity for analysis of many joints with predominating shear stresses. Hence, Volkersen theory is often used as a reference for more sophisticated methods of analysis but it is not further discussed here. A more thorough discussion can be found in e.g. [98].

Since the analysis of Bleich was published, a large number of more refined analytical models for adhesive joints have been published. Such analytical methods provide closed-form solutions suited for parametric studies, but the adaptability is in general restricted to ideal geometries and rather simple material models.

As the ability of computers rapidly improves, it is by means of numerical methods possible to solve more complicated problems with regard to geometry, material models, boundary conditions, etc. The predominating and most general numerical approach to solving differential equations in structural mechanics is the finite element method (FEM) [69, 104] further discussed in Chapter 5. The method can be employed in the analysis of adhesive joints. By means of FEM, arbitrary geometries can be analysed and more effort can be put into the development and implementation of for instance proper material models.

FEM is a powerful tool in structural analysis, but there are some special features to be considered in analysis of adhesive joints, e.g. that the stress distribution will be dependent on element-size. If a more accurate stress distribution is required in
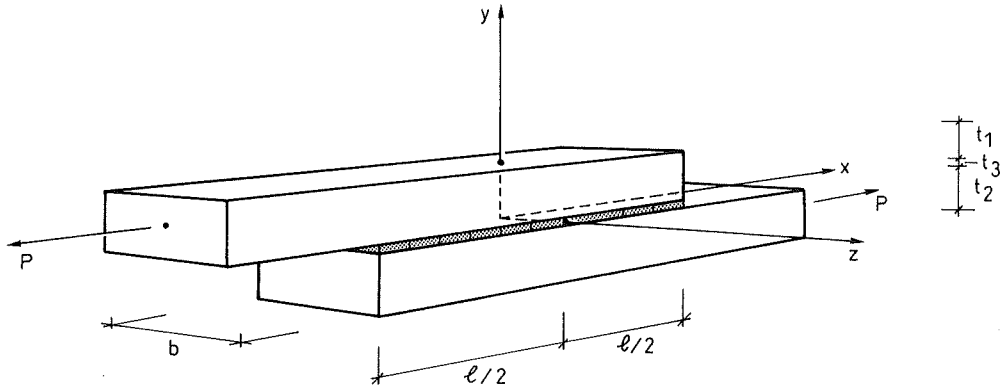
Figure 2.1: *Single-lap joint geometry.*

the analysis, more and smaller elements should be added in regions of concentrated stresses. It may then be desired to use larger elements in areas with small gradients to reduce the total number of elements. Then, if the bond is modelled as a thin layer, this may give rise to numerical problems due to the shape of the elements.

Regardless of whether analytical or numerical methods are used, the bond layer may be considered in three major ways. The simplest is to assume that the stiffness properties of the thin bond line have a negligible influence on the stress distribution. Accordingly, both the thickness and the deformations of the bond may be neglected. The stress and strain components to be introduced in a strength or fracture criterion of the bond will be equal to those of the adjacent material in the adherends.

If the bond line thickness is of considerable size in comparison to other dimensions, it will be of significance in the equations of equilibrium and should then be included in a proper analysis. More sophisticated material descriptions may be introduced, considering the local stiffness within the bond line. Using FEM, the bond line can then be modelled as one or several layers of two- or three-dimensional elements of some finite thickness.

The most common approach used in analytical analysis is a compromise of these two approaches, where the thickness but not the deformations of the bond line is neglected. In FEM this approach is also possible by modifying the nodal connections of the adherend-to-adherend interface according to required bond line properties and, hence, the problem of aspect ratio will vanish. However, using a standard FE-code the simplest approach is often to model the bond layer as being of finite thickness. This approach is employed in the present study and will be further discussed below.

A more thorough discussion of the bond line modelling is given in [98], including some relevant references.

2.2. Stress Analysis

Theoretical considerations based on fracture mechanics imply that there is in general some measure of fracture toughness that will partly or totally govern the strength of adhesive joints. For ductile joints and for joints with a homogeneous state of stress this property will be of less significance, while for brittle joints it will be the predominanting bond line property.

For a ductile joint which exhibits a rather uniform stress distribution, it may be adequate to use stress or strain analysis in connection with some proper failure criterion. However, various stress or strain based criteria, such as a conventional or modified von Mises criterion, have not proved to be of general use in adhesive joint design.

For brittle joints, an adequate failure criterion should include fracture toughness in one way or another. This can be done by using so-called *softening* models, which includes the gradual softening of the material during increasing deformation, i.e. the complete stress-deformation curve including its descending branch. From the stress-deformation performance of the material the work required to bring the material to complete failure can be determined. Such an analysis will henceforth be referred to as *non-linear fracture mechanics*, NLFM, and will be further discussed in Sec. 2.4.

Since the work of *Bleich*, significant contributions have been made in the field of stress analysis of bonded systems. A good résumé is given by *Adams and Wake* [1]. Of later work, papers by *Bigwood and Crocombe* [8, 9] can be mentioned, in which a sixth order differential equation is describing an overlap joint. The adherends are assumed to be linear elastic cylindrically bent plates, and the adhesive is a non-linear layer modelled according to the theory of nonlinear elasticity with a prescribed stress-strain curve approximated as a continuous mathematical function. In design, the main problem remains; no adequate and general strength criterion has been proposed. For very ductile joints, *Crocombe* [21] suggests a yield criterion, corresponding to the theory of limit load for perfectly plastic material.

One major benefit of conventional stress analysis is that it makes the analysis quite straightforward. A linear-elastic stress analysis of a joint may sometimes give qualitatively valuable information in a design situation and may be used to study the visco-elastic effect on the stress distribution, see for example [37, 46, 82].

2.3. Fracture Mechanics

2.3.1. General

Fracture mechanics focuses on the failure process of a body and can be beneficially used for in analysis of bodies with various kinds of stress concentrations. Fracture mechanics theories are sometimes considered to be inconclusive, assuming real or fictitious cracks and involving a large number of parameters such as G_c, G_f, R, K_c, Q_c, J_c, etc., with curious dimensions and unclear diversities. However, as a
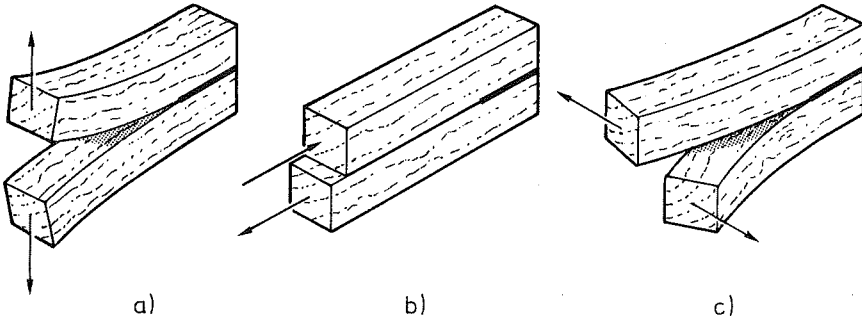
Figure 2.2: *Modes of cracking: a) mode I, b) mode II, c) mode III.*

phenomenon fracture mechanics is part of daily life for most of us, for instance the sometimes frustrating exercise of opening a candy bag. It may seem impossible until a small cut is created in the bag followed by a rapid and unexpected slit propagation with a total collapse of the bag. Prior to the crack, the stresses are distributed over a large area, but as soon as the crack is formed, there will be very high stress concentrations at the vicinity of the crack, which will totally govern the failure process. Hence, to design an optimal candy bag, information on the strength but more important the resistance to crack propagation of the bag material is required.

Commonly the fracture process is divided into three separate modes, given in Fig. 2.2. Mode *I* represents the symmetric opening perpendicular to the crack surface, while mode *II* and *III* denote antisymmetric shear separations, as indicated in Fig. 2.2.

In conventional linear elastic fracture mechanics, LEFM, it is assumed that the analysed body is infected with some real or fictive initial crack. Fig. 2.3 shows a cracked body with a crack length a. Linear elastic analysis will entail the stress state at the crack tip to be singular, which cannot be handled by conventional stress based criteria. The process zone is assumed to be small in comparison to other dimensions and the local failure will be brittle. There are a number of textbooks dealing with linear fracture mechanics in general, e.g. [43, 54], and with emphasis on adhesive joints, e.g. [3, 53].

2.3.2. Stress intensity approach

In LEFM there are two prevalent approaches for characterization of crack growth. One is based on stress intensity factors K by which the stress state close to the crack tip can be described. The stress intensity factors are defined as

$$
\begin{aligned}
K_I &= \lim_{r \to 0} \sqrt{2\pi r}\,\sigma_{yy}(r) \\
K_{II} &= \lim_{r \to 0} \sqrt{2\pi r}\,\sigma_{xy}(r)
\end{aligned}
\tag{2.1}
$$
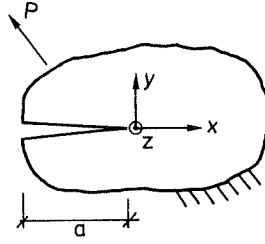
Figure 2.3: *Bonded body with initial crack.*

$$K_{III} = \lim_{r \to 0} \sqrt{2\pi r} \sigma_{yz}(r)$$

for the modes I, II, III respectively, where r is the distance from the crack tip to a point straight ahead of the crack, σ_{yy} is the normal stress and σ_{xy} and σ_{yz} are the two shear stress components. K has the dimension force/(length)$^{\frac{3}{2}}$ or stress$\cdot\sqrt{\text{length}}$ and may be quantified for instance in the unit MPa$\sqrt{\text{m}}$. The magnitude of the stress intensity factors depends on the load, the geometry and the material properties of the cracked body. For isotropic materials, K-values for different geometries are given in handbooks, see e.g. [43]. The total action of the separate K-values are added in accordance to the chosen fracture criterion and compared to some critical stress intensity factor, denoted K_c. This takes the general form

$$K_{tot} = K_{tot}(K_I, K_{II}, K_{III}) \leq K_c \qquad (2.2)$$

A frequently used way of adding the action of K-values is according to a quadratic rule

$$K_{tot}^2 = K_I^2 + K_{II}^2 + \frac{K_{III}^2}{1 + \nu} \leq K_c^2 \qquad (2.3)$$

A modified stress intensity approach, using a generalized bi-material intensity factor for adhesive joints with non-sharp interface corners, is presented by *Groth* [36].

2.3.3. Energy approach

The second major crack growth approach is based on energy considerations. The crack expansion is characterized in terms of the energy necessary to create a new unit area of crack surface. The applied energy is called energy release rate or sometimes crack driving force, G, which may be given in the units Nm/m^2 or N/m. This fracture energy is to be compared to its critical value, G_c. This critical value may in addition to surface energy also be generalized to include plastic energy dissipation and is then often denoted J_c [43, 70].

Assuming quasi-static elastic behaviour, the energy released during crack propagation, G, will be equal to the change in applied external energy, W, minus the
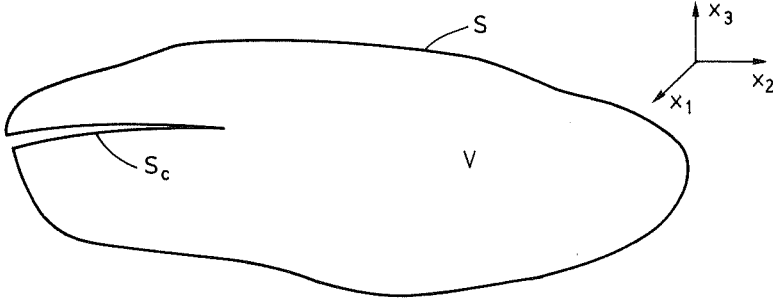
Figure 2.4: *A cracked body with volume V and surface S.*

change in stored strain energy, $d\Phi$, per increase of fracture surface, dA, in the body during a crack propagation, [43], i.e.

$$G = W - \frac{d\Phi}{dA} \qquad (2.4)$$

and the change in applied external energy is defined by

$$W = \int_S t_i \frac{du_i}{dA} dS + \int_V b_i \frac{du_i}{dA} dV \qquad (2.5)$$

where t_i are the tractions on the surface S, u_i are displacements and b_i are the body forces. The change in strain energy is

$$\frac{d\Phi}{dA} = \frac{d}{dA} \left(\int_V \sigma_{ij} \frac{du_i}{dx_j} dV \right) \qquad (2.6)$$

A simple illustration of Eq. (2.4) is given in Fig. 2.5 and is valid for a linear elastic body, loaded by a single load, P, and with $\Phi = 0$ when $P = 0$. The specimen elongation goes from u to $u + du$ as the crack propagates from a size A to $A + dA$ at constant load. The strain energy is interpreted as the area below the $P - u$ curve at the present crack length, i.e.

$$\begin{cases} \Phi(A) = \frac{1}{2} P \cdot u \\ \Phi(A+dA) = \frac{1}{2} P \cdot (u + du) \end{cases} \qquad (2.7)$$

which for the limit of $dA \to 0$ may be expressed as

$$\frac{d\Phi}{dA} = \frac{P}{2} \frac{du}{dA} \qquad (2.8)$$
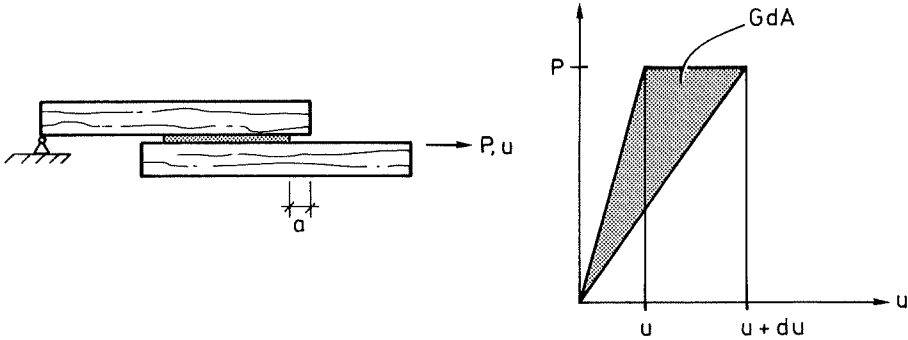
Figure 2.5: *Graphical interpretation of the energy release rate, G.*

and the change in applied external energy per increase dA is

$$W = P\frac{du}{dA} \tag{2.9}$$

if zero body forces are assumed and Pdu is the work of the external load at a crack propagation, dA. Hence, the energy release rate takes the form

$$G = \frac{1}{2}P\frac{du}{dA} \tag{2.10}$$

From Fig. 2.5 and Eq. (2.10) and with the displacement at the point of load application defined as $u = CP$, C being the compliance of the specimen, the energy release rate can be expressed as

$$G = \frac{1}{2}P^2\frac{dC}{dA} = -\frac{1}{2}u^2\frac{(dC^{-1})}{dA} \tag{2.11}$$

which for a body loaded with a single load forms the base of the *compliance method*, commonly used in fracture mechanics analysis. Accordingly, G can be expressed as a function of the change in compliance of a body during unit growth of a crack. The compliance can be calculated by means of arbitrary methods, such as beam theory or FEM. Explicit expressions for Eq. (2.11) for a number of simple geometries are given in [53] and several applications for notched beams has been presented by *Gustafsson* [38, 40].

A possible outcome from the compliance method is to express G in terms of sectional forces. This is done by *Petersson* [71] and expressed as a critical load multiplication factor, α_c, given by the formula

$$\alpha_c = \sqrt{\frac{2b_cG_c}{\dfrac{\beta V_1^2}{GA_1} + \dfrac{\beta V_2^2}{GA_2} - \dfrac{\beta V^2}{GA} + \dfrac{M_1^2}{EI_1} + \dfrac{M_2^2}{EI_2} - \dfrac{M^2}{EI} + \dfrac{N_1^2}{EA_1} + \dfrac{N_2^2}{EA_2} - \dfrac{N^2}{EA}}} \tag{2.12}$$
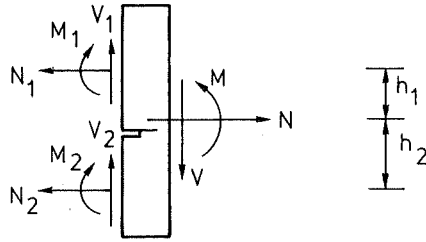
Figure 2.6: *Sectional forces close to the crack tip.*

where signs and indices are given in Fig. 2.6 and β is a cross-sectional parameter considering the non-uniform shear stress distribution across the cross section. The simplicity of the expression is obtained by assuming the flexibility matrix to be diagonal. Accordingly, this simple expression is an approximation based on beam theory, and it may serve as a sufficiently accurate formula in many engineering applications.

Based on the compliance method, *Krenk* [57] derives an uncoupled mixed-mode energy release rate for a symmetric single lap joint in terms of local stress concentrations σ_{max} and τ_{max} which are determined from beam theory. For sufficiently slender joints the analysis will correspond to that of Eq. (2.12) but in a general case it also gives an expression for shorter and more ductile joints, as Eq. (2.24) does for the case of pure shear.

2.3.4. Mixed-mode fracture criteria

Of the two fracture mechanics approaches discussed above, the energy approach is considered to have the clearest physical interpretation. It will in the following be the approach most referred to and discussed in relation to the present theory.

As for stress intensity factors, G is sometimes separated into the three crack modes and superposed to a total energy release rate, G_{tot}, in a straightforward manner

$$G_{tot} = G_I + G_{II} + G_{III} \tag{2.13}$$

For isotropic materials in plane stress the relation between G and K is given by

$$\left\{ \begin{array}{c} G_I \\ G_{II} \\ G_{III} \end{array} \right\} = \left(\frac{1}{E} \right) \left\{ \begin{array}{c} K_I^2 \\ K_{II}^2 \\ (1 + \nu)K_{III}^2 \end{array} \right\} \tag{2.14}$$

Hence, for isotropic materials in plane stress Eq. (2.13) corresponds to the left hand part of Eq. (2.3). For wood and other orthotropic materials the separate stiffness

properties should be accounted for. A relation of G and K for orthotropic and anisotropic materials was given by *Sih et al.* [87] and conveniently expressed for mode-*I* and mode-*II* in orthotropic plane stress by *Suo* [90] as

$$\left\{ \begin{array}{c} G_I \\ G_{II} \end{array} \right\} = \left(\sqrt{\frac{1+\rho}{2E_x E_y}} \right) \left\{ \begin{array}{c} \lambda^{-\frac{1}{4}} K_I^2 \\ \lambda^{\frac{1}{4}} K_{II}^2 \end{array} \right\} \tag{2.15}$$

where λ and ρ are defined in engineering constants as

$$\lambda = \frac{E_y}{E_x}, \qquad \rho = \frac{\sqrt{E_y}}{2G_{xy}} - \sqrt{\nu_{xy}\nu_{yx}} \tag{2.16}$$

and where the coordinates x and y are defined in Fig. 2.3. Due to material symmetry, there is a relation between the two Poisson's ratios, i.e. $\nu_{xy}/E_x = \nu_{yx}/E_y$. In case of plane strain the elastic constants will change to

$$E_x^* = \frac{E_x}{(1 - \nu_{xz}\nu_{zx})} \quad , \quad \nu_{xy}^* = \frac{(\nu_{xy} + \nu_{xz}\nu_{zy})}{(1 - \nu_{xz}\nu_{zx})}$$

$$\tag{2.17}$$

$$E_y^* = \frac{E_y}{(1 - \nu_{yz}\nu_{zy})} \quad , \quad \nu_{yx}^* = \frac{(\nu_{yx} + \nu_{yz}\nu_{zx})}{(1 - \nu_{yz}\nu_{zy})}$$

The fracture process in mode-*I* and mode-*II* does not in general consume the same amount of energy. For mode-*II*, the crack growth characteristics seem to be governed by the ductility of the adhesive. By studying composites in a scanning electron microscope (SEM), *Bradley* [13] reports that, for brittle resins in mode-*II* dominated mixed mode, sigmodial shaped microcracks form a considerable distance ahead of the crack tip, giving significant load redistribution, while for mode-*I* dominated cracks the process will be a more discreet crack opening. The result is that the G_{IIc}/G_{Ic} ratio of such composites is usually in the range of 3 to 10. For composites with very ductile resins, G_c is similar in mode-*I* and mode-*II* and consequently, the G_{IIc}/G_{Ic} ratio may be expected to be close to 1.0. However, for very ductile materials it is doubtful whether G is a relevant design property. *Chai* [15] has shown that while G_{Ic} is little influenced by bond thickness, the magnitude of G_{IIc} is significantly affected by thickness, for thin bonds of both brittle and toughened epoxies.

A common mixed-mode parameter is the phase angle, $\psi_K = \psi_K(K_I, K_{II})$. ψ_K is a relevant mixed-mode parameter as it is, for linear elastic materials, directly related to the stress state at the vicinity of the crack tip, cf. Eq. (2.1). If, however, the governing parameter in the analysis is G, it may be adequate to express ψ_K as a function of the corresponding energies $\psi_K = \psi_K(G_I, G_{II})$, which is straightforward from Eq. (2.15), and we get

$$\psi_K = \arctan\left(\frac{K_{II}}{K_I}\right) = \arctan\left(\sqrt{\sqrt{\frac{E_x}{E_y}}\frac{G_{II}}{G_I}}\right) \tag{2.18}$$
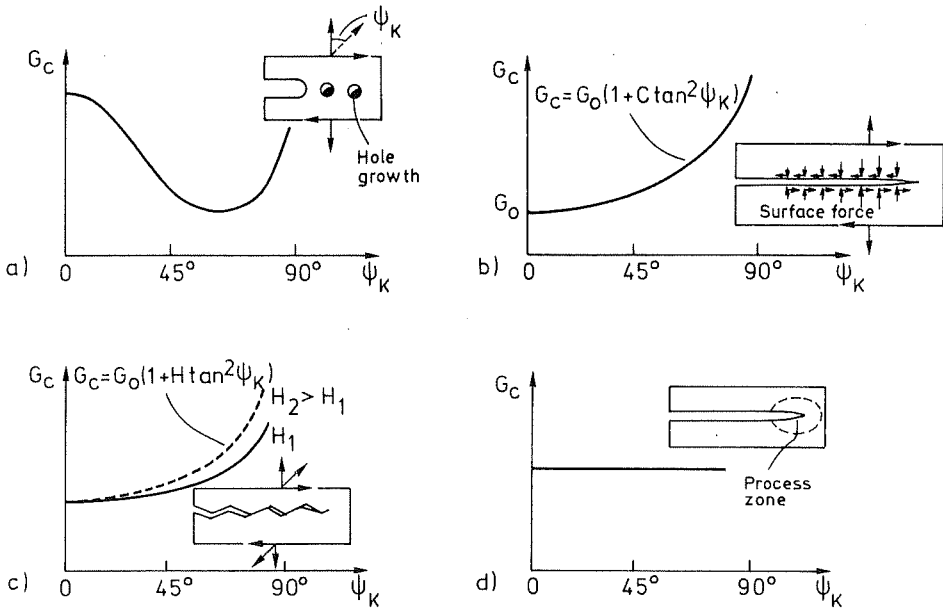
Figure 2.7: *Classification of ductile to brittle materials with regard to energy release rate in mixed-mode, based on [42]. a) ductile material. b) and c) brittle material. d) intermediate toughness material.*

He et al. [42] defines three types of material with respect to the total fracture energy in a mixed-mode space, see Fig. 2.7. The total critical energy release rate, G_c, including nonlinear effects, is plotted versus ψ_K. Ductile materials (a) fracture by hole coalescence and expose a minimum G_c in the intermediate region. Brittle materials (b) fracture without any crack tip blunting. As *Bradley* stated, G_c increases significantly with the increase of ψ_K. This behaviour could include or be analogously analysed as a frictional problem which is characterized by the the roughness parameter H (c). For the third type of material, G_c can be considered to be independent of the mode mixity (d).

Wood may be considered to be a brittle material, cf. Tab. 3.1; the ratio G_{IIc}/G_{Ic} is in the range of 2-5 [93]. *Wu* [101] suggested a stress intensity based failure criterion for a crack along the grain in balsa wood in the form:

$$\left(\frac{K_I}{K_{Ic}}\right)^m + \left(\frac{K_{II}}{K_{IIc}}\right)^n \leq 1.0 \qquad (2.19)$$

where m and n are set to 1 and 2 respectively. For $K_{Ic} = K_{IIc} = K_c$ and m=n=2, Eq.(2.19) equals Eq.(2.3). The *Wu*-criterion was later experimentally verified by *Mall et al.* [64] in evaluation of experimental results of eastern red spruce for cracking along the grain. It was also in principal supported by the results of *Woo and Chow* [100] from tests of tropical hardwoods, while *Williams and Birch* [99] suggest from
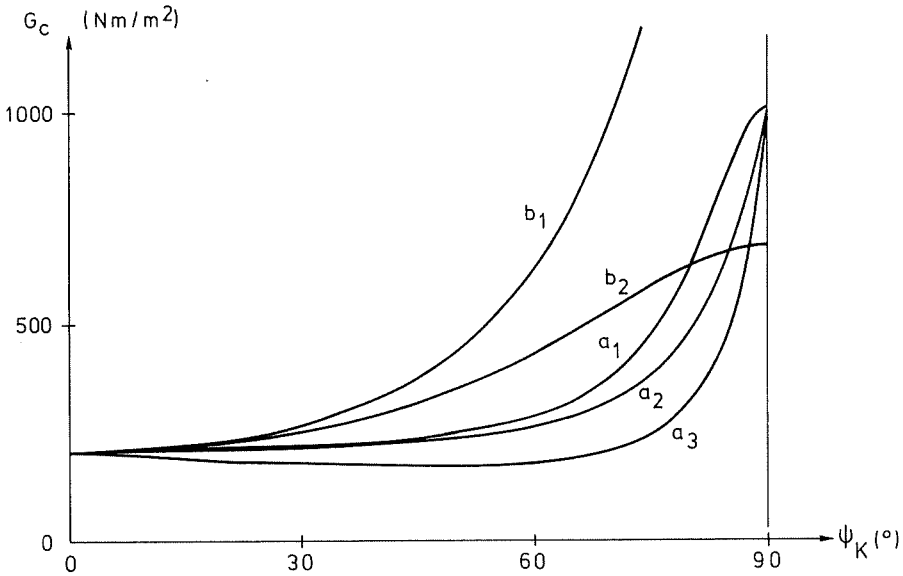
Figure 2.8: *Comparison of two different proposed failure criteria for brittle materials.* $a_1 - a_3$ *Represents Eq. (2.19) [101] with* $m=n=2$, $m=1$ $n=2$, $m=n=1$, *respectively.* $b_1 - b_2$ *Represents Eq. (2.20) [48] with* $\lambda_2=0.1$ *and 0.3.*

tests of Scots pine that K_{II} has no or little influence on the fracture criterion in the range of $\tan \psi_K \leq 3$ but some influence on the hardwood utile. Neither of the two latter references presents pure mode-II tests, and it is thus not possible to quantitatively apply the criterion in Eq. (2.19).

By using Eq. (2.15), the criterion in Eq. (2.19) can be transformed into energy release rates and plotted in a $G_c - \psi_K$ diagram. This is presented in Fig. 2.8, where the Wu-criterion is represented by the curve a_2. In the transformation of Eq. (2.19) by means of Eq. (2.15) the stiffness properties are assumed to be: $E_x = 12$ GPa, $E_y = 0.4$ GPa, $G_{xy} = 0.75$ GPa and $\nu_{yx} = 0.015$. The fracture properties, taken from *Mall et al.* [64] were assumed to be 0.42 and 2.18 MPa$\sqrt{m}$ for K_{Ic} and K_{IIc}, respectively, which corresponds to $G_{Ic} = 205$ Nm/m^2 and $G_{IIc} = 1011$ Nm/m^2. For the Wu-criterion, G_c may be considered to be constant in the range of $0°$ to $60°$, followed by an approximately five times increase. Accordingly, G_c is relatively insensitive to changes in shear stress for a mode-I dominated failure, while a small increase in normal stress will have a severe effect on G_c for a mode-II dominated fracture process.

For adhesive joints, the mixed-mode G_c characteristics will differ for each individual joint, depending on the brittleness. Hence, in the literature there are references that support the characteristic of the Wu-criterion in Fig. 2.8, e.g. [16, 45, 95], while others report deviating mixed-mode behaviour [78, 103].

A strength criterion to fit the increase of G_c with ψ_K for delamination of thin films, was suggested by *Jensen et al.* [48], in the form

$$G_c(\psi_K) = \frac{G_{Ic}}{1 - (1 - \lambda_2)\sin^2\psi_K} \tag{2.20}$$

where λ_2 is a material constant in the range of typically 0.1 to 0.3, for which a lower value indicates a more brittle material. Eq. (2.20) is plotted in Fig. 2.8, facilitating a comparison to Eq. (2.19) which is based on recorded wood data. For the present wood recordings a simple and perhaps sufficient criterion would be a bi-linear relation in the $G_c - \psi_K$ diagram. This is suggested by *Chai* [15] for epoxy bonds for which the interaction point is experimentally shown to be influenced by the brittleness and the thickness of the bond.

2.4. Present Analysis including Bond Line Softening

2.4.1. General

The failure process in a small material volume when the material has reached the peak stress and subsequently will attain a state of complete failure will be studied. The material degradation is not necessarily abrupt, as it may involve a considerate amount of energy dissipation. However, due to instabilities, such characteristics are rarely recorded in direct material testings. This topic will be further discussed in the following chapter.

The present theory has its origin in the *Fictitious Crack Model*, FCM, presented by *Hillerborg et al.* in 1976 [44]. This model has reached vast acceptance in the analysis of fracturing concrete [38, 72], but it has also been applied to other materials such as fibre-reinforced plastics and laminates [4, 84] and wood [12, 38].

The concept of FCM is presented in Fig. 2.9. As load is applied to the specimen, it will initially behave linear elastic (A), but as the load is increased there will be micro-cracks in the specimen yielding nonlinear behaviour (B). At peak stress a localized fracture zone will be formed, which gradually will open during increasing deformation but decreasing external load on the specimen (C). The surrounding material will unload when the process zone softens and, hence, to facilitate stable performance during the complete test, the softening deformations must be larger than the unloading recovery.

2.4.2. One-dimensional analysis

In the literature there are a few references on joint analysis, including bond line softening, to be found. For joints loaded perpendicular to the bond line, mode-I analyses have been presented by *Ungsuwarungsri* and *Knauss* [92] and by *Stigh* [88].

A pure shear analysis has been performed by *Ottosen* and *Olsson* [68] using the same basic assumptions as in Volkersen theory, i.e. pure tension adherends and
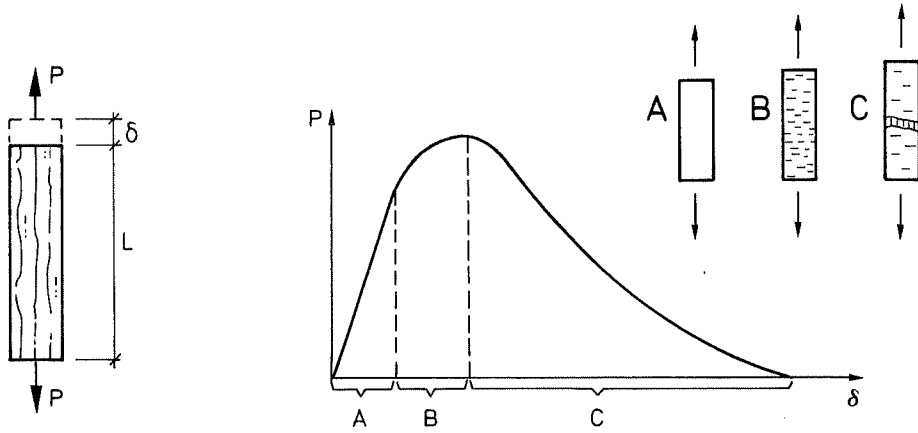
Figure 2.9: *Stable test result for a brittle material. The fracture process may be divided into three characteristic stages: A linear elastic, B micro-cracking, C localized failure.*

pure shear adhesive, but using a bi-linear stress-strain bond model including either plastic hardening or softening. A parametric study on how different characteristic joint parameters influence joint strength was performed.

The present pure shear analysis is based on a paper presented by *Gustafsson* in 1987 [39], which was further discussed in [98]. This non-linear fracture mechanics approach is found to be a unified theory incorporating linear elastic fracture mechanics, linear and nonlinear elastic analysis including some maximum strain or stress criterion, and limit load ideal plasticity as special cases. By means of the present theory, it is possible to handle the special cases of linear elastic fracture mechanics and conventional maximum stress analysis, as well as an intermediate region where these special models cannot singly describe the failure process. Furthermore, it is possible to determine if or when the special models are applicable. The present
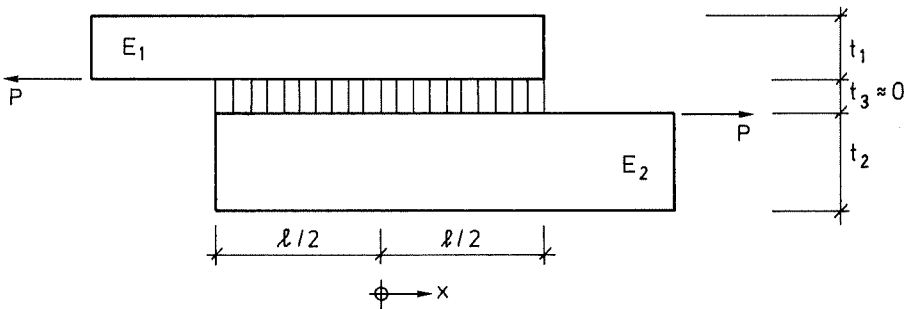
Figure 2.10: *Single lap joint with constant width $b_1 = b_2 = b_3$.*
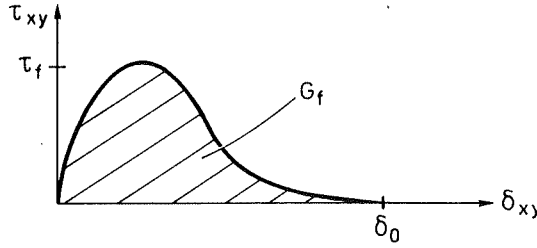
Figure 2.11: *Constitutive relation of a bond line in pure shear.*

model is nonlinear in the sense that it has a nonlinear stress-deformation relation, and it is a fracture mechanics model, since it gives a description of the local mechanical performance of the bond line all the way to its complete separation. Moreover, major material properties can be expressed in terms of critical energies related to those in conventional fracture mechanics.

In softening analysis of adhesive joints it is legitimate to consider the bond line to have no initial thickness. Hence, the deformations will be described as relative openings across and slips along the bond and the longitudinal strain will equal that of the adjacent material. A single lap joint of the type in Fig. 2.10 is considered, for which the bond line is assumed to have no initial thickness. The mechanical properties of a bond line, given in Fig. 2.11, are constituted by the relation between the local shear stress, τ_{xy}, and the local shear displacement, δ_{xy}, across the adhesive layer.

The predominant bond parameters are strength, τ_f, and fracture energy, G_f, which is defined as the energy required to bring a unit area of the bond surface to complete fracture. This corresponds to the area under the $\tau_{xy} - \delta_{xy}$ curve, i.e.

$$G_f = \int_0^{\delta_0} \tau_{xy} d\delta_{xy} \qquad (2.21)$$

In case of self-similar crack propagation, i.e. if the process zone will maintain its size and shape during the propagation, the critical energy release rate, G_c can be expected to coincide with G_f.

Joint strength, i.e. the load carrying capacity, is defined as the maximum load, P_{max}, during gradual increase of joint deformation, and as the $\tau_{xy} - \delta_{xy}$ curve is bounded, no special fracture criterion is required. The normalized load carrying capacity or normalized mean shear stress at failure may be expressed as a function of only three variables [39]

$$\frac{P_{max}}{\tau_f b \ell} = \mathcal{F} \left[\frac{\ell^2 \tau_f^2}{E_1 t_1 G_f}, \alpha, g \right] \qquad (2.22)$$

where $\alpha = t_1 E_1 / t_2 E_2 \leq 1.0$ and g is the shape function of the normalized $\tau_{xy} - \delta_{xy}$
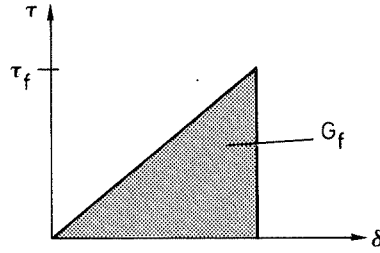
Figure 2.12: *Simplified constitutive relation of a bond line in pure shear.*

curve, τ_{xy}/τ_f versus $\delta_{xy}/(G_f/\tau_f)$. If α and g are not changed, the normalized load carrying capacity is governed by the ratio

$$\omega_1^2 = \frac{\ell^2 \tau_f^2}{E_1 t_1 G_f} \tag{2.23}$$

which in the following will be referred to as the *brittleness ratio*. It depends on the absolute size of the joint through ℓ, on its geometric shape through ℓ/t_1, on the stiffness of the adhering material through E_1 and on the bond line properties through ratio τ_f^2/G_f.

The inverse of the brittleness ratio may be separated into $E_1 G_f/\tau_f^2$ and t_1/ℓ^2. $E_1 G_f/\tau_f^2$ has the dimension length; it may be regarded as a combined inherent length parameter for joint materials and it is related to the characteristic length parameter, $\ell_{ch} = EG_f/f_t^2$, used in analysis of fracture softening solid materials [44], which relates to the size of the process zone, cf. Eq. (4.3). Ratio t_1/ℓ^2 can be directly compared to the empirically determined *joint factor*, $\sqrt{t}/\ell$, given by *de Bruyne* [14].

For a symmetric joint, $t_1 = t_2 = t$ and $E_1 = E_2 = E$, with the simplified constitutive curve shape given in Fig. 2.12 the explicit expression for Eq. (2.22) is [98]

$$\frac{P_{max}}{\tau_f b \ell} = \frac{\gamma}{\omega_1} \tanh\left(\frac{\omega_1}{\gamma}\right) \tag{2.24}$$

where γ is given by the present load case, shown in Fig. 2.13. In Fig. 2.14, Eq. (2.24) is plotted. By means of the brittleness ratio it is possible to distinguish three zones characterizing joint performance. For the limit case of the brittleness ratio approaching zero, the right hand expression of Eq. (2405) will approach 1, and P_{max} will be equal to $\tau_f b \ell$. A small brittleness ratio corresponds to uniform yielding, and for an increasing joint loading the entire joint will obtain its maximum stress, τ_f, simultaneously. Accordingly, for small brittleness ratios the single bond variable affecting joint strength is the local bond strength, τ_f. The strength criterion will correspond to the limit load ideal plasticity suggested by *Crocombe* [21], see Sec. 2.2.

For large brittleness ratios the tanh expression in Eq. (2405) reaches 1, and the normalized maximum load capacity will become directly proportional to the inverse
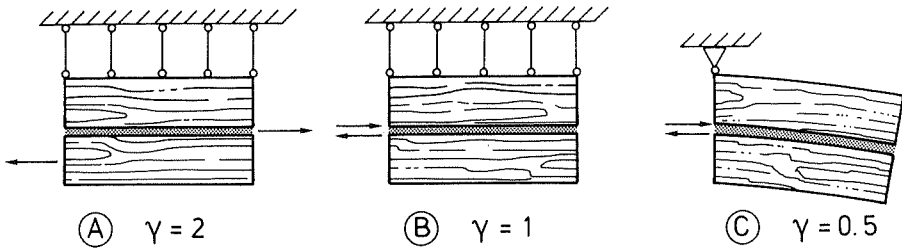
Figure 2.13: *Different load cases of a symmetric lap joint: a) tension-tension loading, b) anti-symmetric loading, c) anti-symmetric loading, including adherend bending.*

square root of the brittleness ratio, i.e.

$$P_{max} = \gamma b \sqrt{tEG_f} \tag{2.25}$$

This corresponds to analysis based on linear elastic fracture mechanics, and P_{max} will be proportional to $\sqrt{tEG_f}$. Notice that bond line fracture energy, G_f, and the adherend stiffness modulus, E, have the same dignity in the strength function.

In the intermediate range, P_{max} will be a function of both τ_f and $\sqrt{tEG_f}$ as well as of the shape of the $\tau_{xy} - \delta_{xy}$ curve. In [39], corresponding curves are given for some different simplified shapes of the $\tau_{xy} - \delta_{xy}$ relation for the case of $\gamma = 2$. A corresponding analysis based on the J-integral approach has later been performed by *Hu et al.* [47].

2.4.3. Mixed-mode analysis

It is a well established rule of thumb that adhesive joints should, if possible, be designed so that the force transferring will be dominated by shear stresses [41]. In practical applications, many joints cannot be considered to be in a state of pure shear and should hence be analysed with respect to a combined stress state. Such analysis should in a general case include mixed-mode criteria for stresses as well as for fracture energy.

A mixed-mode joint analysis for thin and flexible joints is presented by *Edlund* [27]. The adhesive layer is modelled as a material surface with coupled elastic-plastic material description including isotropic hardening and damage. *Schellekens* [84] presents a similar model for composite structures taking into account the orthotropic behaviour with regards to stiffness and strength properties. These models are based on theory of plasticity and coupled in the sense that the yield condition is dependent on the mixed-mode stress state. Hardening and softening is accounted for by expanding and shrinking the yield surface, respectively, through some scalar multiplication factor.
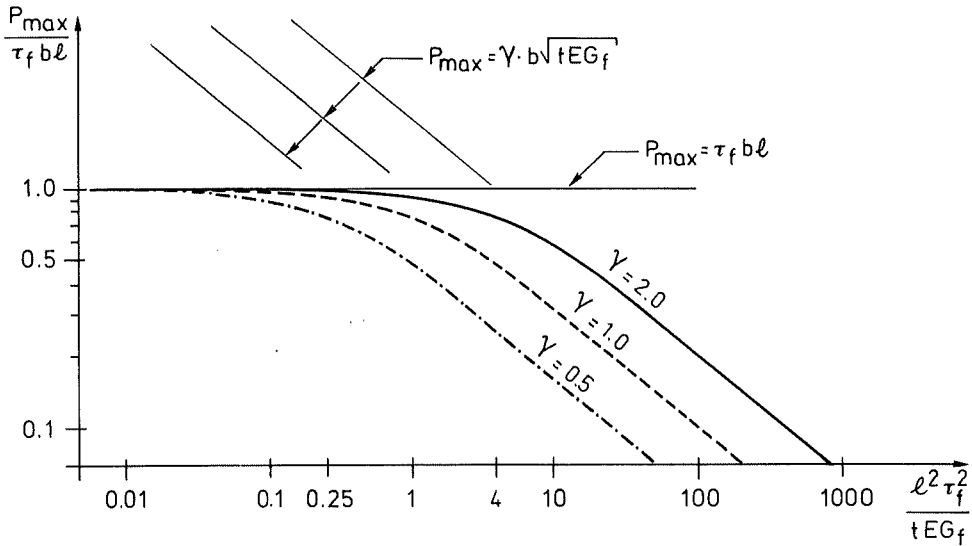
Figure 2.14: *Normalized joint strength versus brittleness ratio for symmetric lap joints with different loading conditions.*

In the general theory of elasticity three main groups of materials may be distinguished, namely *hyper-elastic, Caucy elastic* and *hypo-elastic*. For hyper-elastic materials the strain energy function $w_s = \int \sigma_{ij} d\epsilon_{ij}$ is independent of path and is hence a potential for stress, while for Caucy elastic materials w_s is path dependent. For hyper-elastic as well as for Caucy elastic materials the stress state is uniquely defined by the state of strain. The total fracture energy, G_f, is for the in-plane mixed-mode fracture determined by

$$G_f = \int_\Gamma (\sigma d\delta_n + \tau d\delta_s) \qquad (2.26)$$

where Γ is the deformation path that results in complete separation of the actual bond line. For hyper-elastic materials Eq. (2.26) suggests that $G_f = G_f(\psi)$ is constant.

Hypo-elastic means elastic in a lower sense, but all elastic materials (hyper-elastic or Caucy elastic) are not hypo-elastic. However, every isotropic elastic material with invertible stress-strain relation is indeed hypo-elastic. In hypo-elasticity increments of stress are linear related to increments of strain (as in common incremental theories of plasticity), and it is possible to enlarge the hypo-elastic approach to account for inelastic behaviour as well.

In the application to adhesive joints, there is a lack of experimental recordings able to verify any of the models mentioned above. Furthermore, simple models of analysis may be valid for certain sets of material but not involve a general cogency, cf. the classification of mixed-mode fracture resistance by means of brittleness in

Fig. 2.7. In the present analysis total fracture energy is in general path dependent (depends on the mode of mixity), and materials involved may be characterized as Caucy elastic.

As a consequence of assuming negligible bond thickness, the stress components acting parallel to the bond surface, i.e. with coordinates given in Fig. 2.1, σ_x and σ_z, will not be considered in the fracture modelling. This may be a rational simplification if the adhesive layer is thin and flexible in comparison to the adjoining substrates. In case of wooden joints the difference in stiffness is not always so pronounced and, depending on the load case, σ_x may be of considerable magnitude. If these components are considered to be of significance in the analysis, for instance in some strength criterion based on principal stresses, the strain components can be set equal to those of the adjacent material.

An additional consequence of neglecting the bond thickness is that the strain as a measure has no interpretation, as it is to be related to a zero thickness. Instead, corresponding deformation components should be used. If, however, a linear displacement field is assumed over a fictitious thickness, t', a fictitious strain parameter, $\gamma' = \delta/t'$, may be used in a FE-code with regular 2-D elements.

For a bond line with negligible thickness a general stress-deformation description may be given in the form

$$
\begin{bmatrix} \dot{\sigma}_y \\ \dot{\tau}_{xy} \\ \dot{\tau}_{yz} \end{bmatrix} = \begin{bmatrix} D_{11} & D_{12} & D_{13} \\ D_{21} & D_{22} & D_{23} \\ D_{31} & D_{32} & D_{33} \end{bmatrix} \begin{bmatrix} \dot{\delta}_y \\ \dot{\delta}_{xy} \\ \dot{\delta}_{yz} \end{bmatrix} \tag{2.27}
$$

where D_{ij} are stiffness variables which may be functions of the current state of stress or deformation. By prescribing δ_{yz} to be zero, the equations are reduced to

$$
\begin{bmatrix} \dot{\sigma}_y \\ \dot{\tau}_{xy} \end{bmatrix} = \begin{bmatrix} D_{11} & D_{12} \\ D_{21} & D_{22} \end{bmatrix} \begin{bmatrix} \dot{\delta}_y \\ \dot{\delta}_{xy} \end{bmatrix} \tag{2.28}
$$

The corresponding relation for the case of $\tau_{yz} = 0$ is

$$
\begin{bmatrix} \dot{\sigma}_y \\ \dot{\tau}_{xy} \end{bmatrix} = \begin{bmatrix} D_{11} - \dfrac{D_{13}D_{31}}{D_{33}} & D_{12} - \dfrac{D_{13}D_{32}}{D_{33}} \\ D_{21} - \dfrac{D_{23}D_{31}}{D_{33}} & D_{22} - \dfrac{D_{23}D_{32}}{D_{33}} \end{bmatrix} \begin{bmatrix} \dot{\delta}_y \\ \dot{\delta}_{xy} \end{bmatrix} \tag{2.29}
$$

For the condition of only two stress and deformation components considered, the notation will be changed in the following to σ and τ for stresses and δ_n and δ_s for opening normal and shear deformations, respectively.

A further assumption that may be introduced is that there is no coupling between normal and shear stresses and the shear stresses are mutually uncoupled, i.e. the off-diagonal terms in Eq. (2.27) are zero and Eqs. (2.28) and (2.29) are identical. This
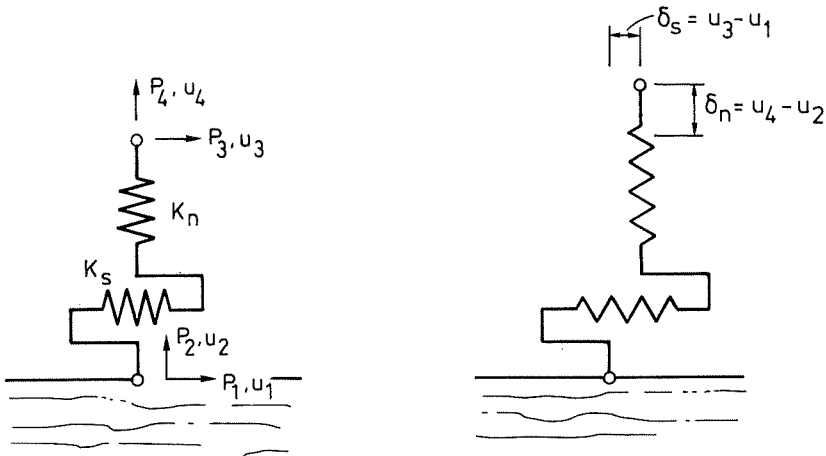
Figure 2.15: *Spring model of the present mixed-mode bond line model.*

assumption is often acceptable in the elastic state, but in softening such coupling may be significant. In the present analysis no coupling is assumed in the initial elastic region but in the softening region there will be a full coupling. Furthermore, the softening criterion is determined by the mixed-mode deformation state.

The bond line model may be described as two coupled springs, illustrated in Fig. 2.15. The springs connect two adjacent nodal points of the adherend material. One tension/compression spring acts perpendicular to the bond surface and one shear spring acts along the bond line. Whether or not in-plane normal stresses and strains are included in the analysis, the thin adhesive layer will have a negligible contribution to the longitudinal global joint stiffness. It is hence not motivated to add such a stiffness component.

The applied model is a mixed-mode expansion of multi-linear one-dimensional stress-displacement curves, given in Fig. 2.16. The stress components σ and τ are defined by the relative displacements δ_n and δ_s.

$$\sigma = \sigma(\delta_n, \delta_s) \qquad (2.30)$$

$$\tau = \tau(\delta_n, \delta_s) \qquad (2.31)$$

Along the positive δ_n-axis, the $\sigma - \delta_n$ relation is equal to its uniaxial curve and the shear stress is zero. Correspondingly, along the shear deformation axis the normal stress, σ, will be zero and the shear stress, τ, will coincide with that of the one-dimensional pure shear relation.

The most severe load case for many joints is the combined opening mode, i.e. for $\delta_n \geq 0$, and most emphasis has consequently been placed on making a refined material description in this region. If in the model $\delta_n < 0$ the $\sigma - \delta_n$ relation is assumed to be linear elastic, independent of δ_s and the $\tau - \delta_s$ relation is taken to be equal to that for $\delta_n = 0$, i.e. in the pure shear state. The constitutive model is
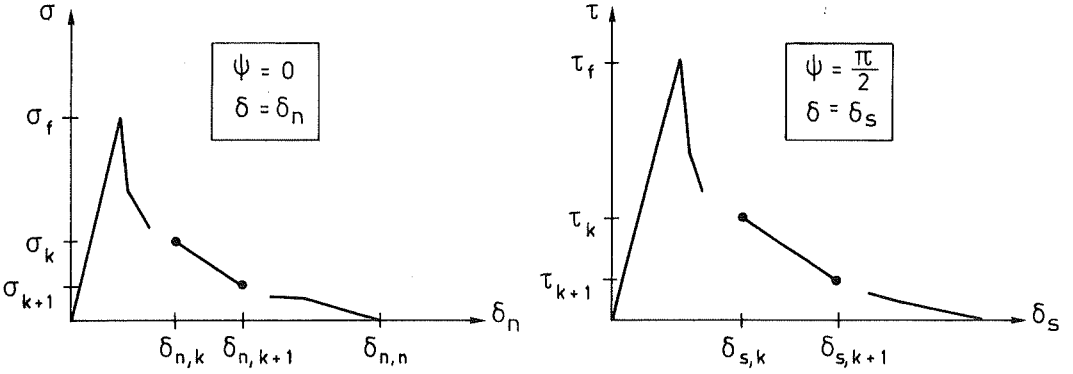
Figure 2.16: *One-dimensional multi-linear stress-displacement relations.*

further symmetric in the sense that

$$\sigma(\delta_n, \delta_s) = \sigma(\delta_n, -\delta_s) \qquad (2.32)$$

$$\tau(\delta_n, \delta_s) = -\tau(\delta_n, -\delta_s) \qquad (2.33)$$

Focusing on the first quadrant, i.e. $\delta_n \geq 0$ and $\delta_s \geq 0$, some typical examples are given in Figs. 2.17 - 2.18 of assumed stress representations. The stress surfaces in the examples are generated by use of bi- and tri-linear stress-displacement relations, respectively.

In order to describe how the stresses σ and τ depend on the relative displacements δ_n and δ_s, it is convenient to introduce a polar coordinate system, see Fig. 2.19. Eqs. (2.30) and (2.31) can then be expressed as

$$\sigma = \sigma(\delta, \psi) \qquad (2.34)$$

$$\tau = \tau(\delta, \psi) \qquad (2.35)$$

where

$$\delta = \sqrt{\delta_n^2 + \delta_s^2} \qquad (2.36)$$

$$\psi = \arctan(\frac{\delta_s}{\delta_n}) \qquad (2.37)$$
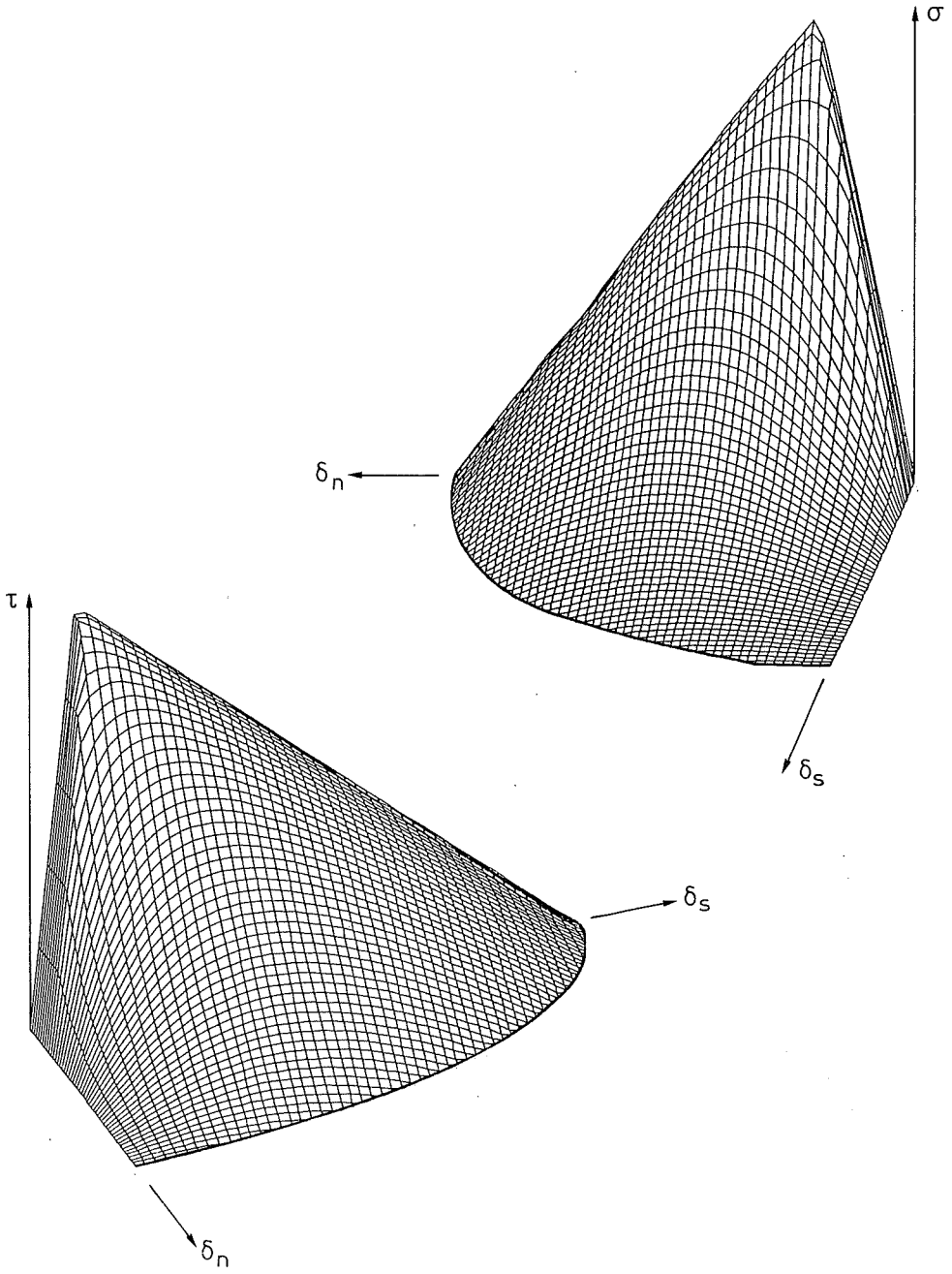
Figure 2.17: *Example of assumed bi-linear mixed-mode stress-deformation relations.*
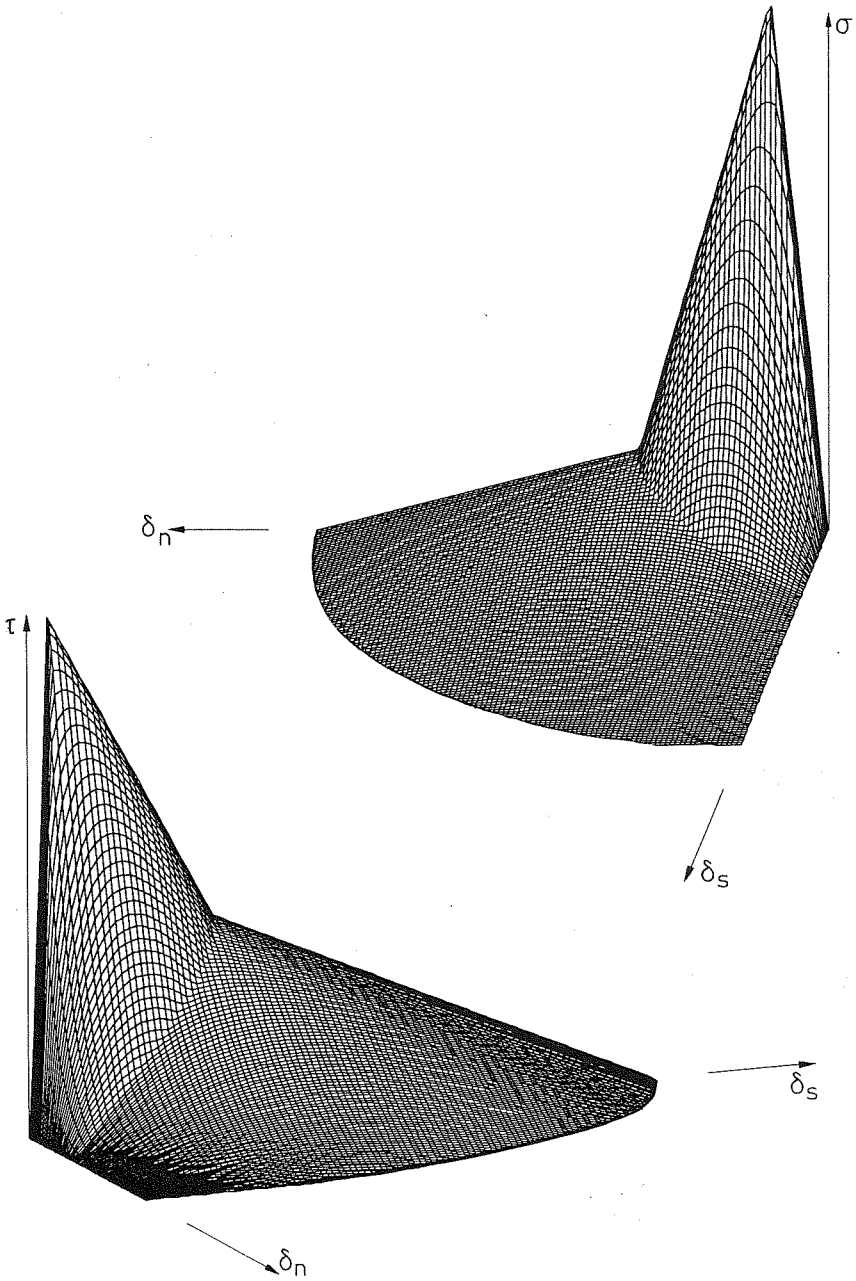
Figure 2.18: *Example of assumed tri-linear mixed-mode stress-deformation relations.*
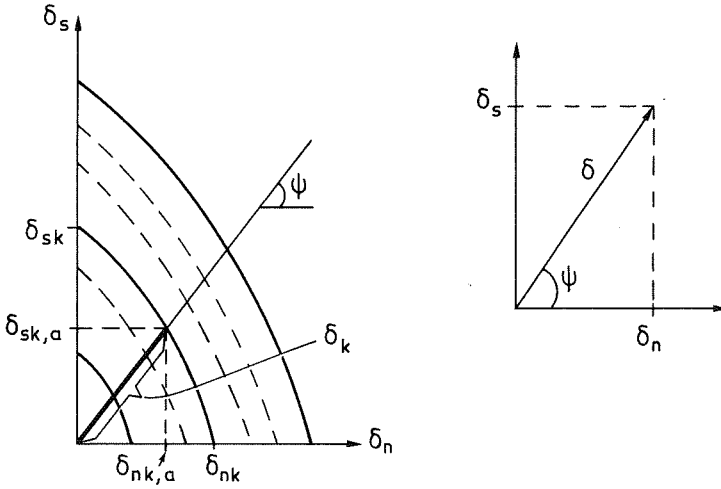
Figure 2.19: *Polar coordinate description.*

The mixed-mode stress-deformation relations for $\sigma - \delta$ and $\tau - \delta$ are for constant ψ supposed to maintain its stepwise linear shape, but vary smoothly with the angle ψ. Accordingly, for increasing value of ψ, the $\sigma - \delta$ curve will shrink from a maximum at $\psi = 0$, while the $\tau - \delta$ relation will expand towards a maximum for $\psi = \frac{\pi}{2} (= 90°)$.

Let first δ_k be a δ-value describing the beginning or the end of a linear part of the stress-deformation curve according to Fig. 2.16. The displacement components, $\delta_{nk,a} = \delta_k \cos \psi$ and $\delta_{sk,a} = \delta_k \sin \psi$ are used in the relation

$$\left(\frac{\delta_{nk,a}}{\delta_{nk}} \right)^m + \left(\frac{\delta_{sk,a}}{\delta_{sk}} \right)^n = 1.0 \tag{2.38}$$

in order to define a proper function for $\delta_k = \delta_k(\psi)$, cf. Eq. (2.19). Eq. (2.38) can be solved easily when $m = n$,

$$\delta_k(\psi) = \left[\left(\frac{\cos \psi}{\delta_{nk}} \right)^m + \left(\frac{\sin \psi}{\delta_{sk}} \right)^m \right]^{-\frac{1}{m}} \tag{2.39}$$

For the four different combinations of m and n being 1 and 2, the expressions for $\delta_k(\psi)$ are

$$\delta_k(\psi) = \frac{\delta_{sk}}{c_k \cos \psi + \sin \psi} \qquad \text{for } m = n = 1$$

$$\delta_k(\psi) = \frac{\delta_{sk}}{\sqrt{c_k^2 \cos^2 \psi + \sin^2 \psi}} \qquad \text{for } m = n = 2$$

$$\delta_k(\psi) = \frac{1}{2}\delta_{sk}\frac{c_k}{\sin \psi \tan \psi} \left(\sqrt{1 + 4\left(\frac{\tan \psi}{c_k}\right)^2} - 1 \right) \qquad \text{for } m = 1, n = 2$$

$$\delta_k(\psi) = \frac{1}{2}\frac{\delta_{nk}}{c_k}\frac{\tan \psi}{\cos \psi} \left(\sqrt{1 + 4\left(\frac{c_k}{\tan \psi}\right)^2} - 1 \right) \qquad \text{for } m = 2, n = 1$$

where

$$c_k = \frac{\delta_{sk}}{\delta_{nk}} \qquad (2.40)$$

For a given value of δ and for the angle ψ, the present stresses σ_a and τ_a are determined by the relations

$$\sigma_a = \sigma_{k,a} + \frac{\sigma_{k+1,a} - \sigma_{k,a}}{\delta_{k+1} - \delta_k}(\delta - \delta_k) \qquad (2.41)$$

$$\tau_a = \tau_{k,a} + \frac{\tau_{k+1,a} - \tau_{k,a}}{\delta_{k+1} - \delta_k}(\delta - \delta_k) \qquad (2.42)$$

in accordance with Fig. 2.20

The stresses $\sigma_{k,a}$ and $\tau_{k,a}$ are generally defined by the relation

$$\sigma_{k,a} = \left(\frac{c_k}{c_k + \tan \psi}\right)^p \sigma_k \qquad (2.43)$$

$$\tau_{k,a} = \left(\frac{\tan \psi_a}{c_k + \tan \psi}\right)^q \tau_k \qquad (2.44)$$

It is easily seen that

$$\sigma_{k,a} = \begin{cases} \sigma_k & \text{for } \psi = 0 \\ 0 & \text{for } \psi = \frac{\pi}{2} \end{cases}$$

$$\tau_{k,a} = \begin{cases} 0 & \text{for } \psi = 0 \\ \tau_k & \text{for } \psi = \frac{\pi}{2} \end{cases}$$

The values p and q have to be chosen in order to obtain best possible fit to experimental values of σ_k and τ_k for various values of ψ in the interval $0 < \psi < \frac{\pi}{2}$. It was, however, found according to experimental results that even with the simplest choice

$$p = q = 1 \qquad (2.45)$$

a reasonable agreement could be obtained. Due to this and for the sake of simplicity only these values of p and q will be used in this report.
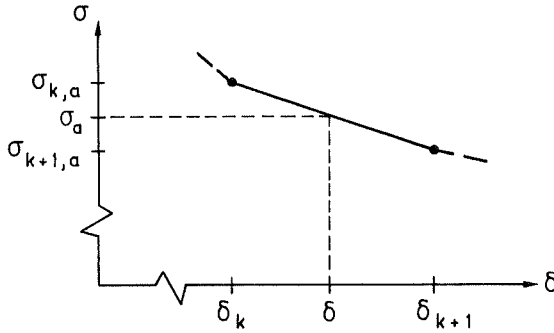
Figure 2.20: *Linear stress-deformation relation in radial direction.*

Contour plots of Figs. 2.17 and 2.18 are given in Figs. 2.21 to 2.24 corresponding to bi-linear and tri-linear models. The material parameters used are: peak stresses $\sigma_f = 6.5$ MPa and $\tau_f = 10.0$ MPa, uniaxial fracture energies $G_{fn} = 360$ Nm/m^2 and $G_{fs} = 980$ Nm/m^2, and the powers in Eq. (2.38) are chosen to be $m = n = 2$, cf. Fig 5.6. The deformation components may be directly interpreted from the contour figures.

In a finite element analysis, the stiffness components D_{ij} given in Eq. (2.28) are required. The present nonlinear analysis is made in incremental form and, hence, the stiffness matrix requested is the tangential stiffness at the actual values of deformation components $\delta_{s,a}$ and $\delta_{n,a}$. The stiffness matrix may hence be written as

$$
\begin{bmatrix} D_{11} & D_{12} \\ D_{21} & D_{22} \end{bmatrix} = \begin{bmatrix} \dfrac{\partial \sigma}{\partial \delta_n} & \dfrac{\partial \sigma}{\partial \delta_s} \\[2mm] \dfrac{\partial \tau}{\partial \delta_n} & \dfrac{\partial \tau}{\partial \delta_s} \end{bmatrix}
\tag{2.46}
$$

As the stresses and deformations are expressed in polar coordinates the stiffness matrix may be expressed by means of the chain rule as

$$
\begin{bmatrix} \dfrac{\partial \sigma}{\partial \delta_n} & \dfrac{\partial \sigma}{\partial \delta_s} \\[2mm] \dfrac{\partial \tau}{\partial \delta_n} & \dfrac{\partial \tau}{\partial \delta_s} \end{bmatrix} = \begin{bmatrix} \dfrac{\partial \sigma}{\partial \delta} & \dfrac{\partial \sigma}{\partial \psi} \\[2mm] \dfrac{\partial \tau}{\partial \delta} & \dfrac{\partial \tau}{\partial \psi} \end{bmatrix} \begin{bmatrix} \dfrac{\partial \delta}{\partial \delta_n} & \dfrac{\partial \delta}{\partial \delta_s} \\[2mm] \dfrac{\partial \psi}{\partial \delta_n} & \dfrac{\partial \psi}{\partial \delta_s} \end{bmatrix}
\tag{2.47}
$$

The second right hand matrix is obtained through standard derivations and it

Figure 2.21: σ-contour of bi-linear mixed-mode model.

Figure 2.22: τ-contour of bi-linear mixed-mode model.
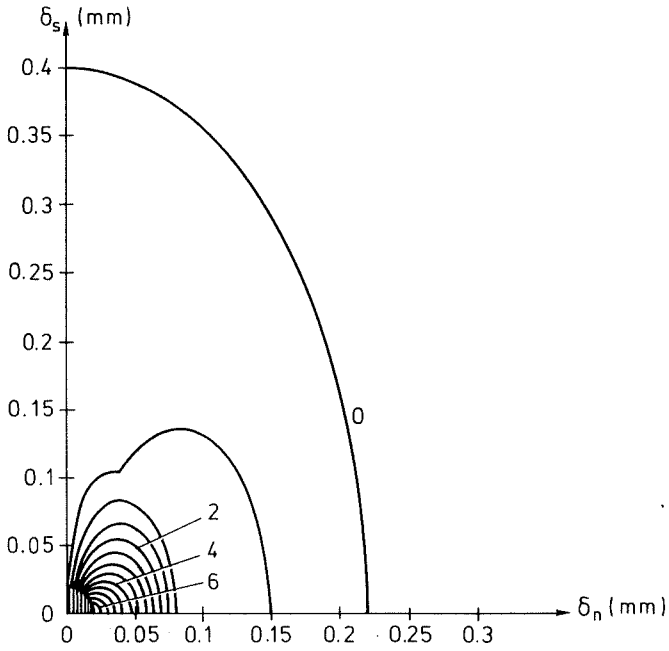
Figure 2.23: *σ-contour of tri-linear mixed-mode model.*
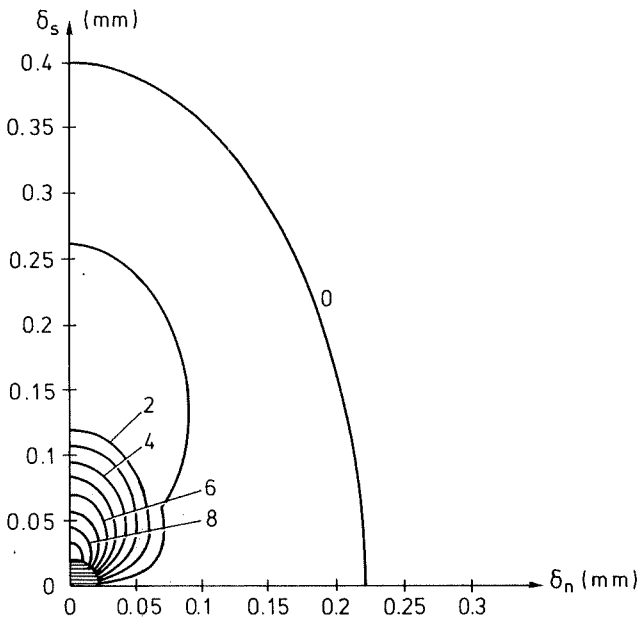
Figure 2.24: *τ-contour of tri-linear mixed-mode model.*

will take the form [52]

$$
\begin{bmatrix} \dfrac{\partial \delta}{\partial \delta_n} & \dfrac{\partial \delta}{\partial \delta_s} \\[3mm] \dfrac{\partial \psi}{\partial \delta_n} & \dfrac{\partial \psi}{\partial \delta_s} \end{bmatrix} = \begin{bmatrix} \cos \psi & \sin \psi \\[3mm] -\dfrac{\sin \psi}{\delta} & \dfrac{\cos \psi}{\delta} \end{bmatrix} \tag{2.48}
$$

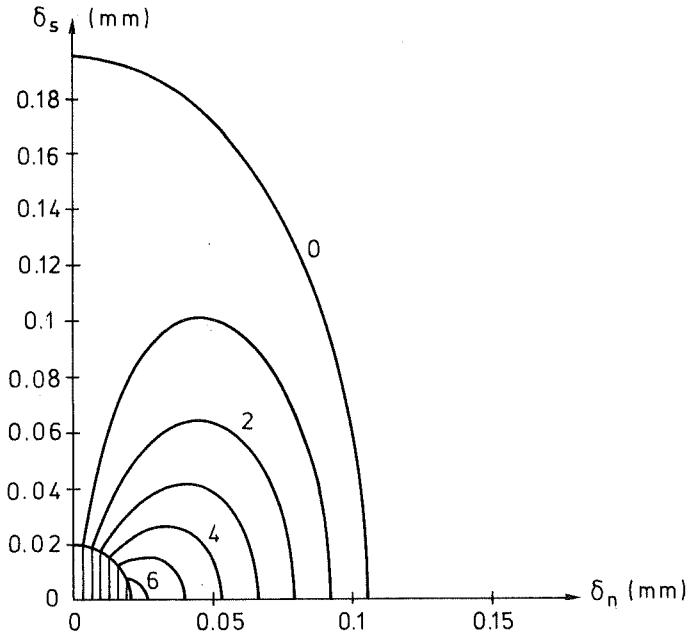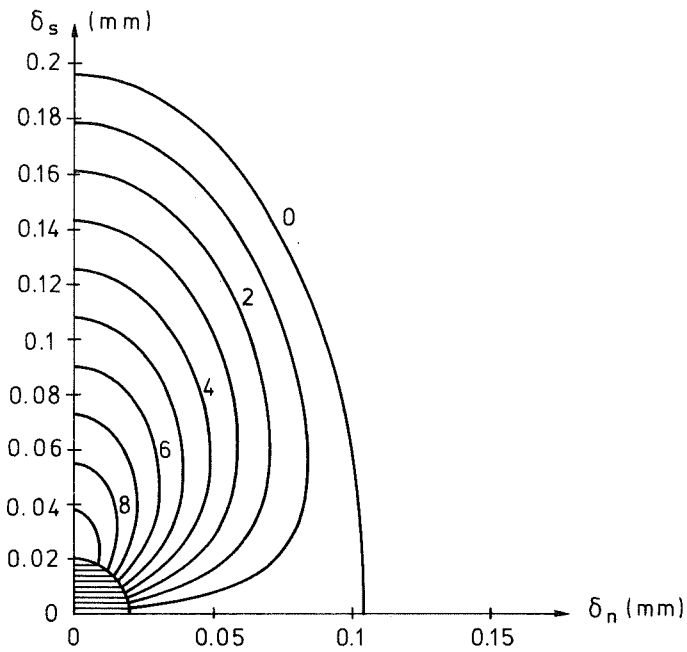The components $\frac{\partial \sigma}{\partial \delta}$ and $\frac{\partial \tau}{\partial \delta}$ are also straightforward to determine, as the stress-deformation relations are assumed to be stepwise linear in the δ-direction. Accordingly, the radial stiffness components are expressed as

$$
\frac{\partial \sigma}{\partial \delta} = \frac{\sigma_{k+1,a} - \sigma_{k,a}}{\delta_{k+1} - \delta_k} \tag{2.49}
$$

$$
\frac{\partial \tau}{\partial \delta} = \frac{\tau_{k+1,a} - \tau_{k,a}}{\delta_{k+1} - \delta_k} \tag{2.50}
$$

where the stress components are given by Eqs. (2.43) and (2.44).

The determination of explicit expressions for the angular stiffness components is more complicated. This could be done for the special cases of integer values of m and n, preferably with some symbolic mathematical computer program such as *Maple* [66]. In the present study, Eqs. (2.49) and (2.50) has been evaluated numerically. The stresses have been calculated for two close angles ψ and $\psi + \Delta \psi$ which directly gives the angular stiffnesses as

$$
\frac{\partial \sigma}{\partial \psi} \approx \frac{\sigma(\psi + \Delta \psi) - \sigma(\psi)}{\Delta \psi} \tag{2.51}
$$

$$
\frac{\partial \tau}{\partial \psi} \approx \frac{\tau(\psi + \Delta \psi) - \tau(\psi)}{\Delta \psi} \tag{2.52}
$$

A basic assumption for the applied model is that the deformations δ will be increasing during the loading process. Using the model in case of unloading means that all deformations are supposed to be recoverable, i.e. at negative deformation increments the stress level will follow the same curve as for the case of loading, see Fig 2.25. This is a violation of the expected physical behaviour, but for the applications in mind in the present study, unloading in the bond are not expected and it is checked that unloading effects are negligible. An implementation of reduced stiffnesses at unloading could be introduced, but this requires knowledge of the unloading characteristics of bond lines in the softening region and such knowledge is presently not available. If softening is supposed to be a pure plastic process, the incremental unloading stiffness could be expected to correspond to the initial elastic stiffness. If on the other hand the softening is due to damage, the unloading path will be expected to revert to the origin. As for other bond properties, the unloading
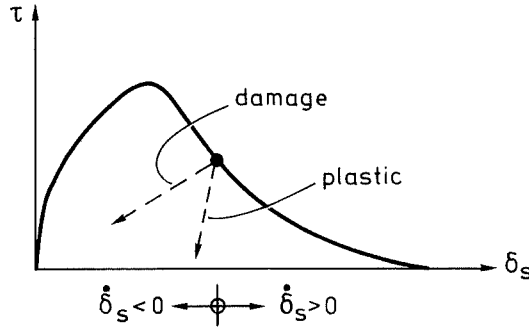
Figure 2.25: *Loading and elastic unloading in pure shear.*

characteristics may vary with the type of material involved, but it has not been within the scope of this study to investigate such effects.

The uniaxial fracture energies are given by the input data. For mixed-mode, the magnitude of G_f is governed by the power parameters m and n and by the deformation path. The total mixed-mode fracture energy is the sum of the contribution from the two modes as given by Eq. (2.26). The mixed-mode angle, ψ_K, given in Eq. (2.18), is not applicable in a straightforward manner. Instead, based on the present model, it is natural to express the mode-mixity as a function of the ratio of the deformation components, cf. Eq. (2.37). In order to obtain a better correspondence to ψ_K an angle ψ_G may alternatively be used, which is defined as

$$\psi_G = \arctan\left(\sqrt{\frac{G_{fs}}{G_{fn}}}\right) \tag{2.53}$$

where G_{fs} and G_{fn} are determined as the energies under the respective stress-deformation curves, using Eq. (2.26).

For a radial deformation paths in the $\delta_n - \delta_s$ field, the mode-*II* component is illustrated as a solid line in Fig. 2.26. In order to indicate the path dependence of the fracture energy, G_f for the cases shown given in Figs. 2.21 and 2.22, two additional paths are calculated and plotted in Fig. 2.27 as a function of the angle ψ. The fracture energy in case A is obtained by following radial paths over the interval $0 \leq \delta_k \leq \delta_0$. The curves B represents the corresponding fracture energy attained by moving first from $\delta = 0$ to $\delta = \delta_{n,0}$ followed by a path in δ_s direction leading to a complete failure. The directions are opposite in case C. It is clear that the use of the model results in a substantial path dependence.

2.5. Discontinuous Performance due to Wood Failure

Wood failure is commonly used as an indication of a proper choice of adhesive. The strength exposed by the adhesive is interpreted as, from the mechanical point
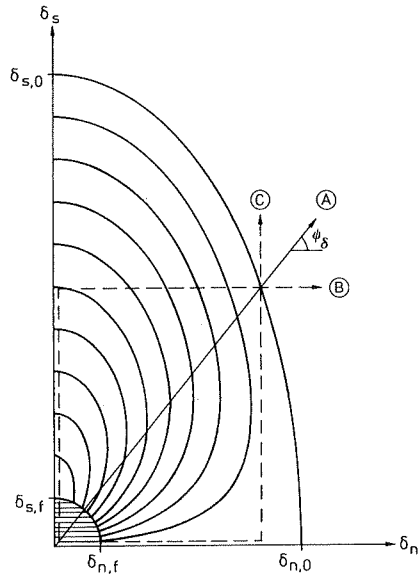
Figure 2.26: *Different paths for G_{fs} determination.*
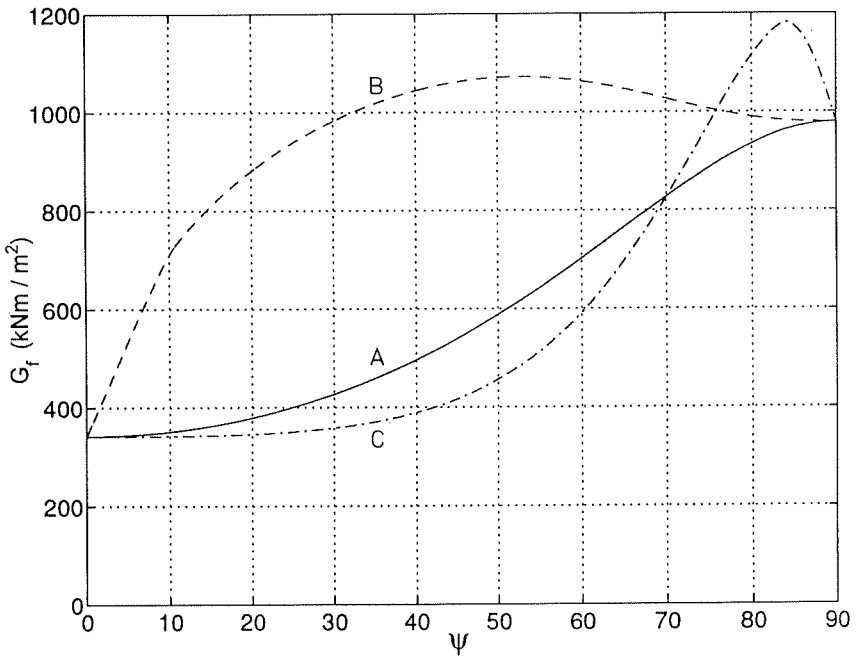
Figure 2.27: *Path dependence of the fracture energy.*
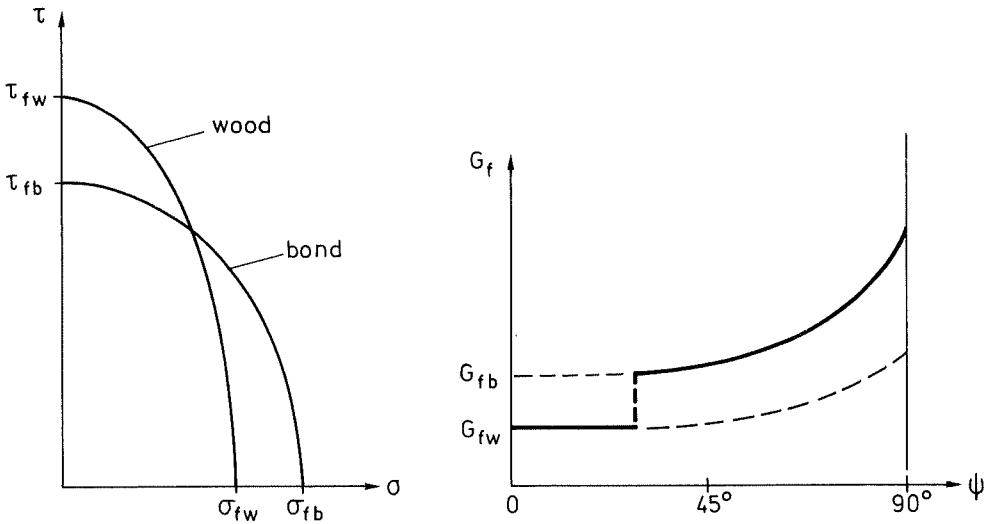
Figure 2.28: *Discontinuous fracture energy function.*

of view, being superior to the wood material, and hence adhesive properties are of no further concern. However, the present test series as well as other tests, e.g. [19, 34, 75], have indicated that even though wood failure occurs, the choice of adhesive affects joint strength and, furthermore, strength may be greater for joints with a small amount of wood failure than for joints with predominating adherend failure. This behaviour is difficult to explain from a conventional maximum stress point of view. Using fracture mechanics it may, however, be expounded in a rather simple and logical way.

Wang and Suo [95] report that for brittle epoxy-aluminium joints in predominant mode-I, the crack often runs within the epoxy layer rather than along the epoxy-aluminium interface, although the fracture energy for the epoxy is more than two times higher than for the interface. As a consequence the mixed-mode fracture energy diagram in Fig. 2.7 will expose discontinuous characteristics. A more thorough examinations of the same observation is given in *Fleck et al.* [32] where the breaking point was observed to be in the range of $\psi_K = 15°$. They derive an expression for crack location by means of a bi-material stress intensity approach and prescribe the crack to follow a path where $K_{II} = 0$.

A more straightforward explanation is that the weakest material will fail, independent of the fracture energy. For a mixed-mode case this is illustrated in Fig. 2.28, in which plausible strength criteria for wood and the bond, respectively, are given. For mode-I dominated failure the bond strength is higher than that of the wood material, yielding wood failure, and vice versa for mode-II dominated failure. If the adhesive layer has a larger fracture energy than the wood material, there will be a discontinuous $G_f - \psi$ diagram, indicating an abrupt change in joint strength if
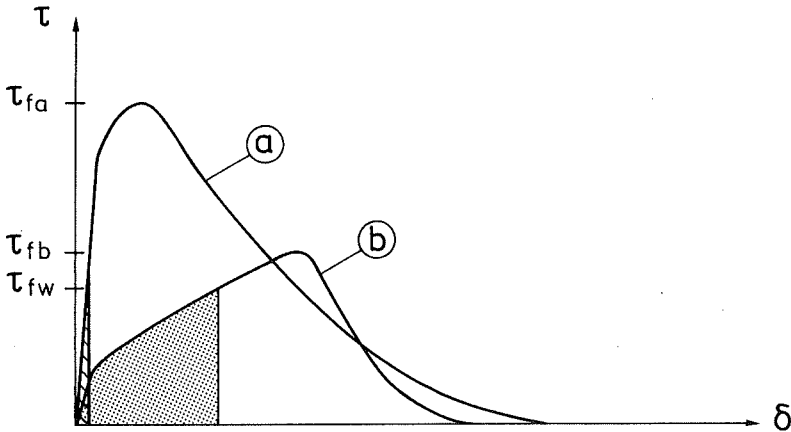
Figure 2.29: *Effective fracture energy, G_f^e, of adhesive bond lines at wood failure.*

fracture energy is the predominating bond property.

With regard to possibility of wood failure, an optimal bond line in a brittle joint should have a large fracture energy but not be stronger than the adjacent wood material. In the analysis, two material models should be included, one for the bond line and one for wood, and the one to be used should be determined by a strength criterion such as in Fig. 2.28. This is not necessarily unique for wooden joints; in e.g. metal joining the same phenomenon may occur but possible failure paths will be in the brittle interface and in the tougher adhesive layer.

A common observation in the literature is that even though there is wood failure, joint strength is clearly influenced by the choice of adhesive. An explanation of this is given by *Gustafsson* [39], and illustrated in Fig. 2.29. In case of wood failure, an effective fracture energy, G_f^e, may be defined as being a combination of bond line and wood fracture energies. Joint strength will be a function of fracture energy, but the magnitude of G_f^e may be a function of bond line material curve shape. Assume two geometrically identical joints bonded by two different adhesives, exposing diverse characteristic properties. Bond line a exhibits higher strength, larger fracture energy and higher initial stiffness properties than bond b. Additionally, the adhering wood material is expected to reveal lower strength, $\tau_{f,w}$, and more brittle behaviour than any of the bond lines. When load is applied, the bond lines will respond according to their respective material curves. At the level when actual stress reaches wood strength, the failure process zone will shift from the bond line to the adhering wood material, and if wood is assumed to involve a fracture energy of minute size, the effective energies will be those marked in Fig. 2.29. Bond line a exposing a considerably larger actual fracture energy than bond b, will, in case of wood failure, exhibit a substantially smaller effective fracture energy, represented by the striped area, than bond b, given by the shaded area.

3. EXPERIMENTAL METHODS

3.1. General Remarks

There is a variety of methods for testing mechanical properties of adhesive joints. It is not possible to pinpoint one of these as optimal, as the objective for testing varies and as each method has its special advantages and perhaps disadvantages. One method may be simple to perform in laboratory, but more complicated to analyse and generalize. Another method might be favourable from the evaluation point of view, but may be very costly and entail high requirements on the laboratory equipment and the personnel who will perform the testing.

There are also different objectives for testing. The most common methods are used to ensure some minimum quality of the bond lines, while the ambition of other methods is higher. They may primarily be used to determine different material moduli of bond lines or adhesive bulk materials. In the determination of such moduli, it is important to refine the state of stress to keep shear properties distinct from tension and compression properties, also when studying the mixed-mode interaction between these stress components.

Many adhesive properties can probably most conveniently be determined in bulk. The adhesive material is then cast into shapes that can be tested in regular standard tension and compression tests. This approach is commonly used to determine properties like Young's modulus and Poisson's ratio of epoxies and other structural adhesives. For many wood adhesives, however, the curing mechanism involves interaction between the adhesive and the wood surface including exchange of moisture, solvents, etc. Consequently, bulk properties can be expected to differ from those of a bond line. For adhesives which set by chemical reaction, too, it is doubtful whether the properties in bulk are comparable to those in bond lines, especially at large plastic deformations. Furthermore, the probably most coveted properties are those in shear. The most commonly used test methods for evaluating shear properties of bulk materials are rather complicated and require fairly large specimens. As adhesives tend to shrink during curing, large-size cast blocks may have significant internal stresses, which may cause micro as well as macro cracks in the specimens. This effect may also occur in bond lines where the shrinkage is partly restrained, but the curing process will differ implying rather small internal stresses in thin bonds. If so, however, the specimen stresses will rather well correspond to those of a real joint.

Accordingly, for wooden joints it is more warranted to test in situ bond lines
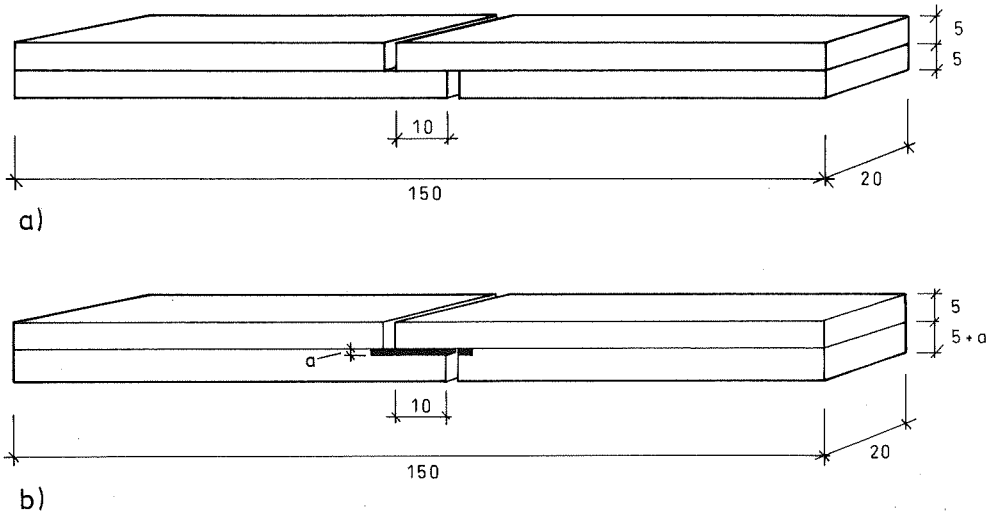
Figure 3.1: *CEN - prEN 302 shear specimen. a) Thin bonds. b) Thick bonds.*

and to define mechanical properties as being those of the bond line, including the interface to the wood material. The material properties of main concern in joint design are strength and fracture energy, to which in situ bond testing is well adopted. The bond line is thin in comparison to the total size of the joint, and even with modern transducers it is difficult to record small relative motions, especially in mixed-mode. Hence, if properties like Young's modulus and Poisson's ratio are requested, these are rather difficult to determine, but the development of optical measuring techniques will most probably facilitate such recordings in the near future.

3.1.1. Standard test methods

For determination of bond line strength there is a number of more or less proper standard or non-standard methods reported in the literature. A discussion of some of these methods can be found in [98]. In the following there will be a short presentation of the *CEN - prEN 302* specimen, given in Fig. 3.1, which is the standard method in connection with Eurocode 5. The specimen is identical to the *DIN 53254* specimen.

In [98] one-dimensional evaluation of some standard shear specimens is performed regarding the uniformity and pure state of stress. According to the one dimensional analysis of Eq.(2.24) with $\gamma = 2.0$, $\tau_f = 10$ MPa, $G_f = 980$ Nm/m^2 and $E = 13$ GPa, the normalized specimen strength, $\bar{\tau} = P_{max}/(\tau_f b \ell)$, is 0.98. The correspondence between specimen and bond line strength can thus be expected to be good. It may, however, be questioned if not the normal stresses in the bond line also will have
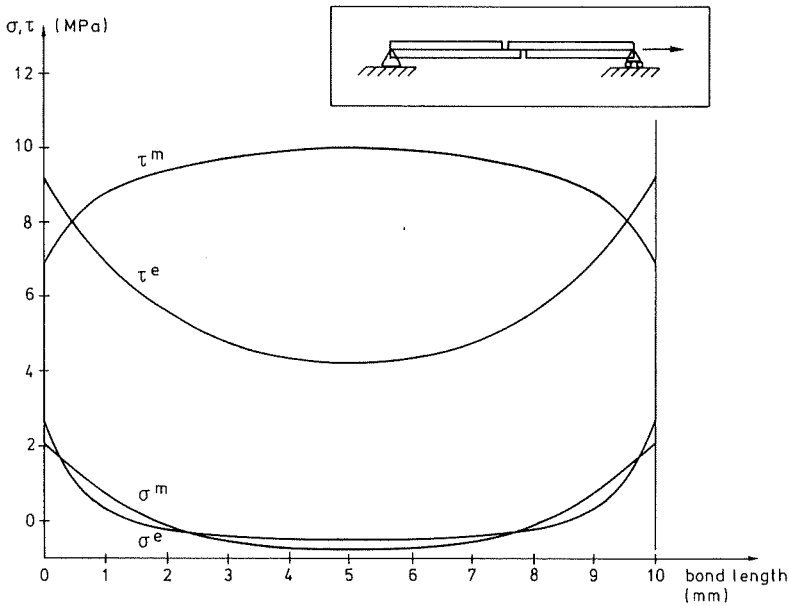
Figure 3.2: *Stress distribution in the CEN - prEN 302 shear specimen. The curves are given for two load levels, $P = 1.12$ kN (elastic) and $P = 1.87$ kN (maximum load).*

an influence on the strength. Fig. 3.2 shows the stress distribution at the limit of the linear elastic state and at maximum load obtained from a mixed-mode FEM analysis (with the trilinear R/P model given in Fig. 5.6 and wood properties in accordance to Eq. (5.38)). The analysis included 50 elements along the bond line. It is clear that there is a considerable mixed-mode stress state at the bond line ends with $\tau/\sigma \approx 4$, and furthermore, the elastic stress state is not quite as uniform as could be expected. The normalized shear strength is 0.93, which is slightly less than for the one-dimensional analysis. However, the load at initial plasticization of the bond line is only about 0.6 times the maximum load carrying capacity for which the stress distribution is rather uniform. The resorcinol/phenol adhesive in the example is a rather brittle adhesive. For more ductile adhesives P_{max}/A will be more equal with the bond line strength τ_f.

The analysis is made assuming pinned and roller support on the bond line symmetry axis at the specimen ends, cf. Fig. 3.2. A rigid support will imply bending moments in the specimen with an average normal stress, $\sigma_{av} \neq 0$. However, in accordance with the analysis, a rigid support would in the example only affect the specimen strength to a minor extent (about 1.5 %, presupposing that no bending is induced at the mounting of the specimen). Correspondingly, a deviation in stiffness of the adherends will be of minute effect. A 10 percent difference in stiffness of the two adherends implies in the example a 0.3 percent decrease of specimen strength.
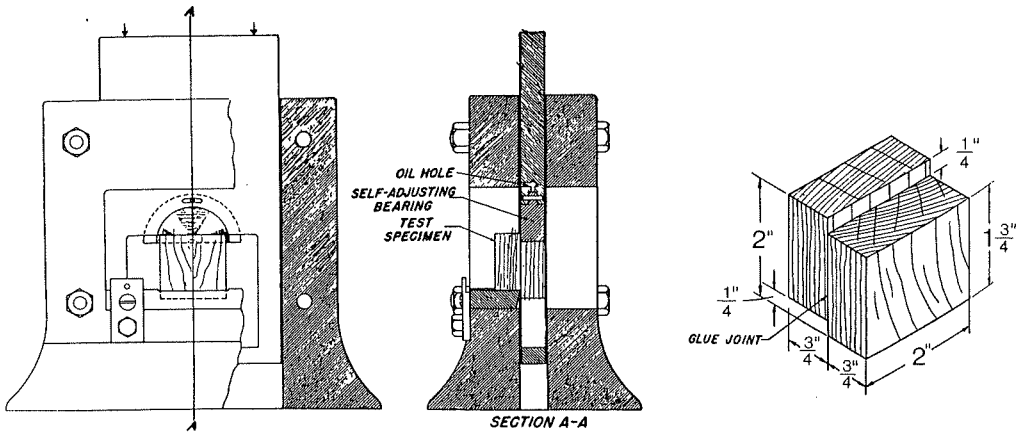
Figure 3.3: *ASTM D-905 shear test configuration and specimen geometry.*
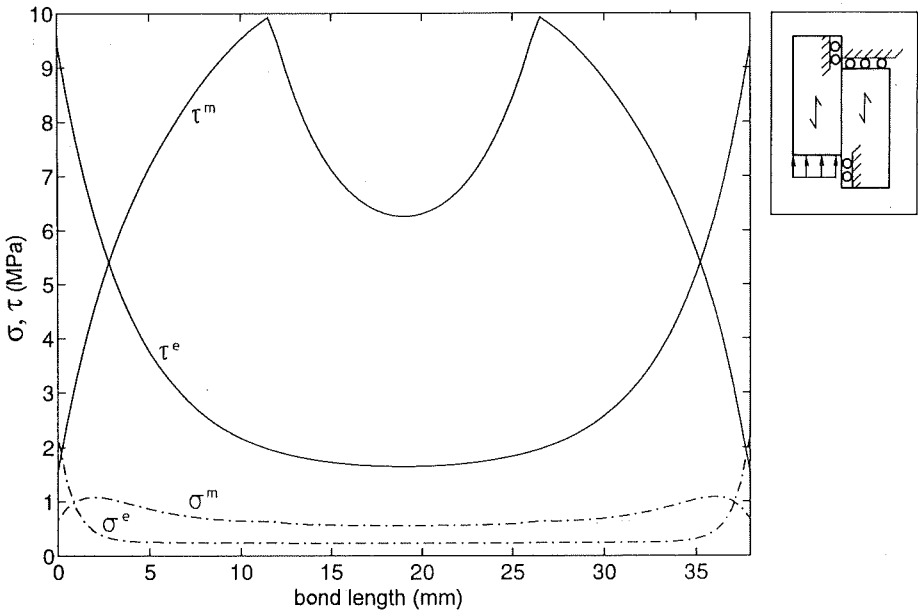
Figure 3.4: *Stress distribution along the bond line of the ASTM D-905 shear specimen at the limit of the linear elastic state (e) and at maximum load (m).*

Another standard shear specimen is found in the ASTM D-905 standard. Specimen geometry and the shearing tool are given in Fig. 3.3. The load is applied at a constant rate of deformation of a movable head. Mean stress at failure as well as the amount of wood failure is reported. A corresponding FE analysis, using identical material properties as for the CEN specimen above and with 76 elements along the bond line was performed. The normalized shear strength was calculated to 0.72, which is a remarkably low value for a shear strength specimen. The low value is partly due to the long overlap length (38 mm), but also because of rather large normal stresses. In Fig. 3.4 the stress distribution is given at the limit of the linear elastic state and at maximum load obtained from a mixed-mode FEM analysis. An analysis on the effect of varying the grain direction of the adherends was performed. The objective was to evaluate the mechanical (stiffness) effects when testing specimens bonded with different grain directions, and to distinguish these from effects associated with adhesion problems. The normalized strength obtained, for the combination of one adherend bonded along the grain and the other bonded on the end grain side was $\bar{\tau} = 0.16$, and for end grain to end grain bonding it was slightly larger, $\bar{\tau} = 0.22$. The stiffness of the end to grain bonded adherend was achieved by changing the positions of the stiffness components D_{11} and D_{22} in Eq. (5.38).

Fracture energy is preferably determined as the area under the complete stress - deformation curve; applicable methods for such recordings for shear are not found in the literature. However, there is a number of methods reported which study the propagating failure in adhesive joints to determine critical stress intensity factors, K_c, critical energy release rate, G_c, etc., which may be suitable for an indirect determination of fracture energy, G_f, see e.g. [53]. The evaluation procedure of the test results must possibly be changed to agree with the definition of fracture energy. One of these standard methods, the commonly used double cantilever beam, DCB, specimen, will be discussed in Sec. 3.3.2.

3.1.2. Stable test performance

To facilitate recordings of the complete stress-deformation curves of brittle adhesive joints or of brittle materials in general, the stiffness of the material surrounding the fracture process zone is crucial. Accordingly, it is important to aim at large stiffnesses of the specimen, the grip arrangements as well as to have a stiff testing machine. The required stiffness of the testing system is determined by the geometry of the specimen, the stiffness and by the brittleness of the material to be tested, cf. [72]. A relevant measure of fracture brittleness of a material is the characteristic length, $\ell_{ch} = EG_f/f_t^2$, which is a part of the brittleness ratio discussed in Sec. 2.4.2. In case of fracture by crack propagation, ℓ_{ch} governs the size of the fracture zone; for small values the fracture zone is small. To perform tests with a uniform stress and gradual softening, the specimens have to be short with regard to ℓ_{ch}. For resorcinol/phenol joints in regular softwoods ℓ_{ch} is in the range of approximately 10 mm in tension perpendicular to grain. Note that E is a modulus of the adherends,

Table 3.1: *Typical fracture mechanics material properties of some materials [38].*

Material	ℓ_{ch}	f_t	E	G_f	$\sqrt{EG_f}$
	mm	MPa	MPa	Nm/m^2	$MPa\sqrt{m}$
Concrete	400	3.5	35000	140	2
Wood fibre board	120	7	4000	1500	2
Gypsum	20	1	4000	5	0.14
Steel	20	1000	200000	100000	150
Wood $\perp$ grain	10	4	500	400	0.5
Carbon fibre/epoxy laminate	8	600	70000	40000	50
Glass	0.5	30	75000	5	0.6

not of the adhesives.

For comparison values of ℓ_{ch} and other fracture mechanics material properties are listed for some different materials in Table 3.1. For large specimens with deep initial cracks, the parameter $\sqrt{EG_f}$ corresponds accordingly to Eq. (2.14) to the critical stress intensity factor, K_c, and hence also describe the stress state close to the crack tip.

The values in Tab. 3.1 are approximate but give a qualitative measure of the test performance for the materials involved. In Fig. 3.5 a plausible test result of e.g. the CEN-specimen in Fig. 3.1 is illustrated. The total deformation (t) of a specimen is the sum of the deformations in the bond line (b) and those of the surrounding material and the testing machine (s). The test is assumed to be carried out being able to control the grip displacements. At the state where the load has passed the peak, the bond line begins to soften and concurrently the surrounding material begins to unload as the applied load decreases. If the unloading deformations are less than the softening, the test will perform in a stable manner. If not, the specimen needs to decrease its deformations while the testing machine forces the deformation to increase. Hence, the specimen will fail in a brittle manner. Possibly the specimen will not fail completely and the last part of the curve will be recorded. However, the area below the curve, expressed by G_f, remains unknown.

In accordance with Fig. 3.5 it is possible, from static stiffness considerations, to establish expressions for stability requirements of the components of the testing machine, or to determine which specimens can be tested in a stable manner with a given testing machine.

Modern material testing machines are usually equipped with a computerized closed-loop control system, see Sec. 3.1.3. In combination with improved optical transducers that we might expect to be available in a future, the feasibility of recording brittle failure will increase. It will then be possible to choose a controlling length on the specimen close to the size of the fracture zone.
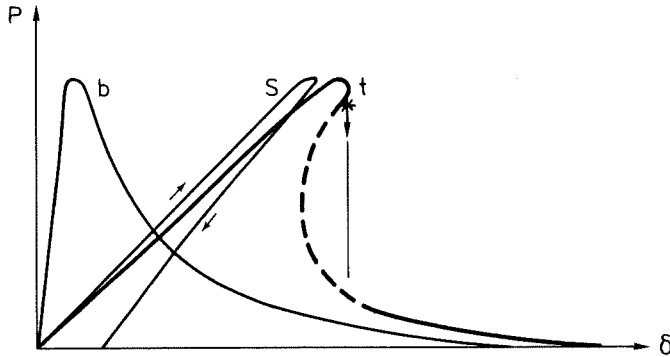
Figure 3.5: *Requirements for stable test performance for a setup with serial stiffnesses.*

3.1.3. Testing machines

The two most important properties of a testing machine, when testing for the complete stress-deformation curve of brittle materials, are response rate and stiffness. One of the earliest and most cited stable test series on brittle materials is that of *Petersson* [72]. He recorded the normal stress versus the widening of a crack in plain concrete with a very stiff testing machine. It consisted of two concrete blocks connected by three insulated aluminium columns. By heating the columns the aluminium expanded, yielding a rigid but slow separation of the concrete blocks.

In the uniaxial test programme of the present study, a closed-loop, MTS 810, 100 kN testing machine was used. The machine is characterized by being rather stiff (total stiffness including actuator and 100 kN load cell is in the range of 40 MN/m) but primarily by being fast, with a responding time of a few milliseconds. This facilitates a fast response of the machine at rapid stiffness changes of the specimen. This kind of machine is primarily designed for high frequency dynamic testing, where the oil under high pressure is forced into and out of the actuators by servo valves. In a closed-loop system the actual displacement or load in the actuator or external transducers is commanded by a function generator. The feedback is then read and subtracted from the command signal and the result is used to drive the servo valve so that a state of equilibrium is maintained. The servo hydraulic system facilitates very fast responses, but the perpetual opening and closing of the servo valves may imply a rather nervous behaviour of the testing machine if it is not carefully calibrated for the test setup in question.

Mixed-mode tests were performed on a biaxial testing machine with electromechanical actuators, shown in Figs. 3.6-3.8. The main feature of the machine is its large stiffness; approximately 50 MN/m in the horizontal direction and 100 MN/m for vertical loading. The machine has at the present date not obtained its final ver-
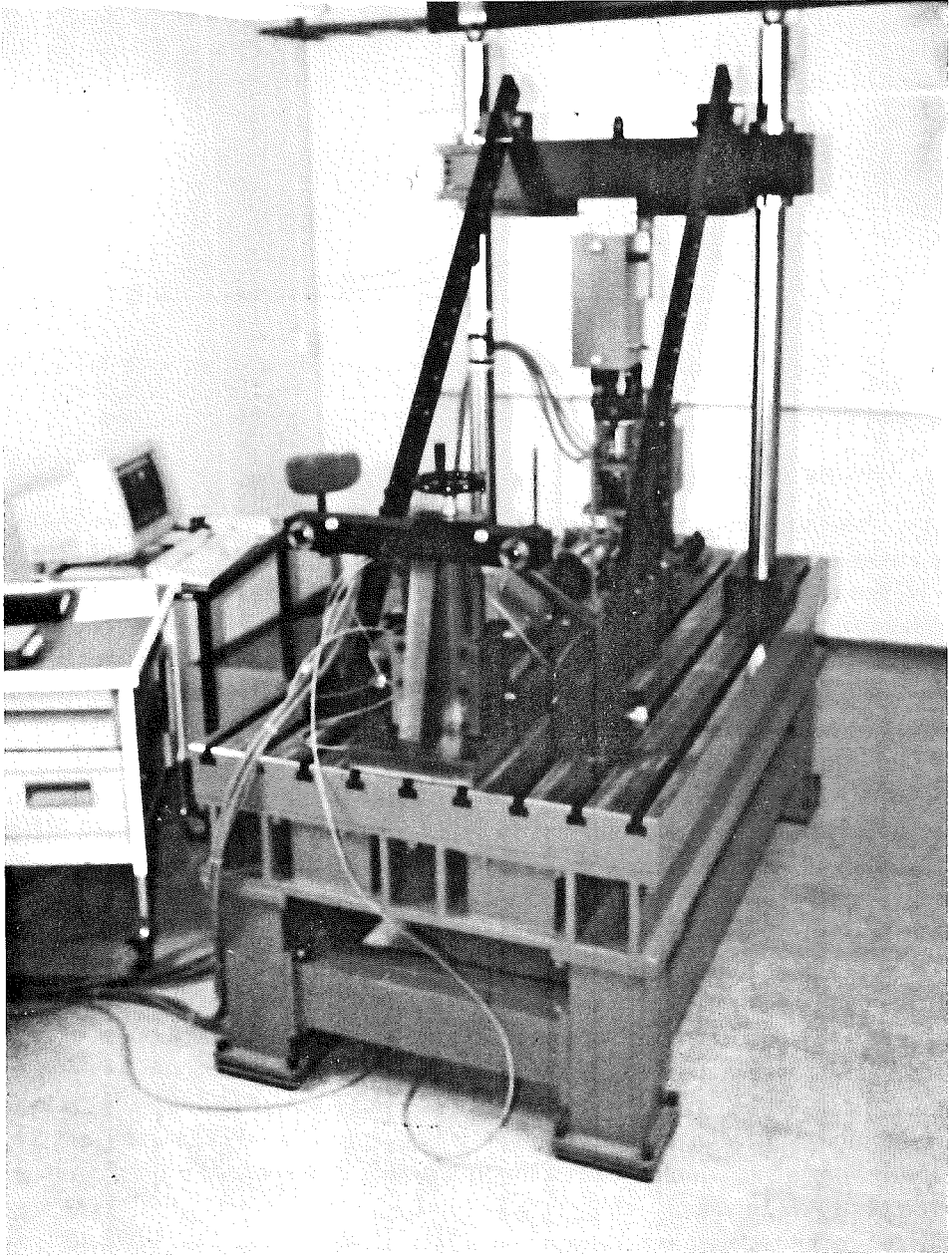
Figure 3.6: *Bi-axial testing machine.*
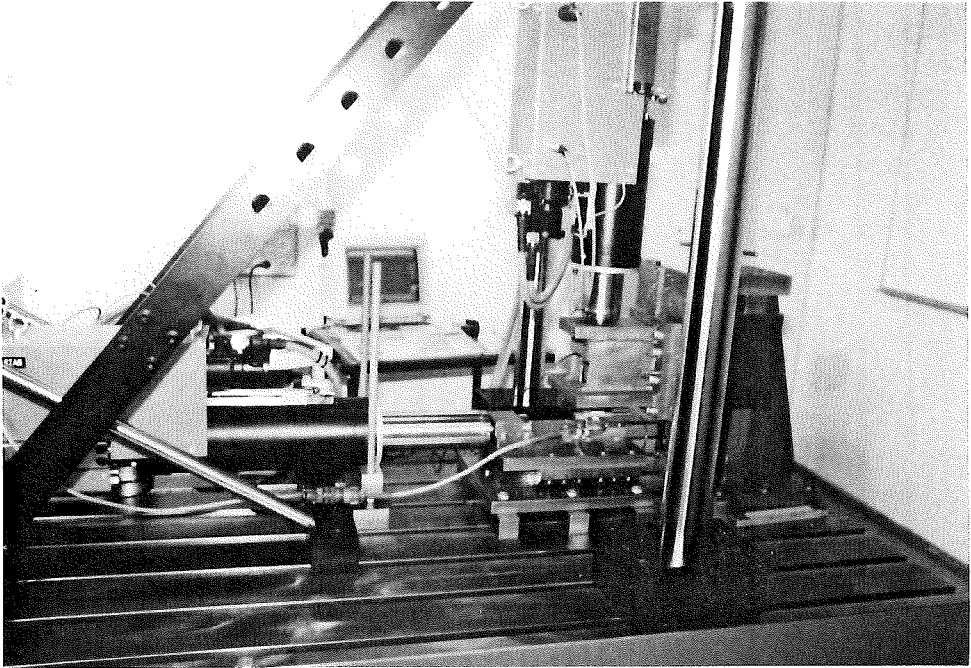
Figure 3.7: *Setup of the bi-axial testing machine.*
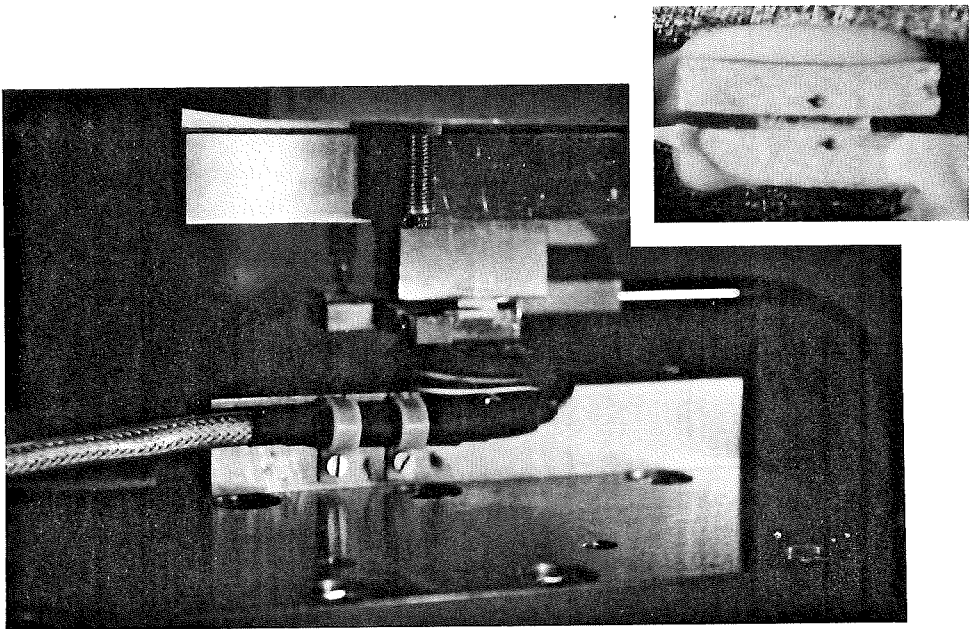
Figure 3.8: *Mounted specimen on the bi-axial testing machine.*
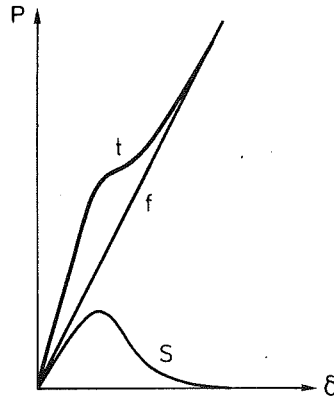
Figure 3.9: *Load-deformation curve with parallel stiffness.*

sion. It still remains to increase the stiffnesses to approximately 200 MN/m in both directions, primarily by improving the actuators and the load cell. The response time is longer than for the servohydraulic machine (MTS 810) but still in the range of only 10 ms for short strokes. The testing table has a size of approximately $2 \cdot 1$ m^2; it is made of solid steel with T-slots to attach the actuators, load frames, etc. One actuator is mounted on the table and the other in perpendicular direction on a crosshead. On each actuator there is also a set of linear bearings on which the test specimen and a bi-axial load cell are mounted, vouching for well-defined movements in the two perpendicular directions. The displacements are recorded with LVDT transducers mounted on the grip arrangements.

In cases where the stiffness of the testing machine is too small, an additional stiffness may be mounted parallel to the specimen, e.g. by a steel rod frame [31, 72]. For a given deformation, the parallel system means that the total load (t) will be the sum of the load in the specimen (s) and the parallel frame (f). This is illustrated in Fig. 3.9 for a case where a softening material curve may be determined in load control of the testing machine. If the stiffness of the parallel frame (f) is well-known, the evaluation of the specimen load-deformation curve is straightforward. Alternatively, a load cell may be placed in series to the specimen, giving a direct value of the specimen load. However, load cells tend to be rather weak as they must deform to give a signal, and hence the gain of mounting the parallel frame will partly vanish. The concept of parallel frame has not been used in this study.

3.2. Bond Line Stress vs. Deformation Fracture Tests

The objective in the development of material test methods has been to find methods to determine the complete stress - deformation curves in one single test. The
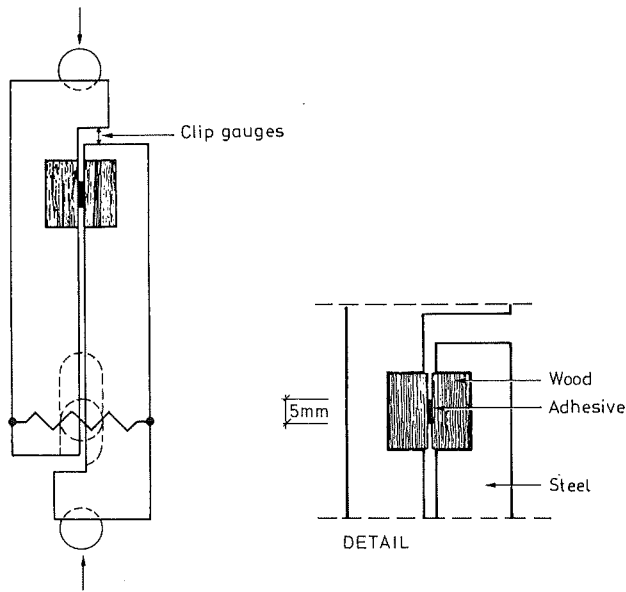
Figure 3.10: *Setup of the small shear test.*

approach has been to use a short bond line to obtain a uniform stress distribution. Further, by using a small specimen and stiff setup, instabilities can be avoided when the bond line softens. The load is applied on the specimens so that the stress components in the bond line will be well defined and possible to distinguish. To facilitate recordings of the complete failure process, high requirements have to be placed on the testing machine, the grip arrangements and the test specimen design.

3.2.1. Small shear specimen setup

The test configuration of the pure shear specimen is shown in Fig. 3.10. It was first presented in [96] and also more thoroughly discussed in [98]. It consists of two steel grips in which the wooden specimen is attached by epoxy resin. To stabilize the setup, a steel ball is placed in a slot and tightened by a rubber band. This counteracts possible bending, torsion and peeling during the test and the previous handling. Load is applied in compression to simplify the mounting to the test machine and to reduce the risk of instabilities during loading. Moment across the specimen is primarily avoided by enforcing the applied load to act through the symmetry axis of the bond.

   Pure shear is achieved through an anti-symmetric loading of the specimen. Ideal anti-symmetry requires that the steel grips are infinitely stiff in comparison to the
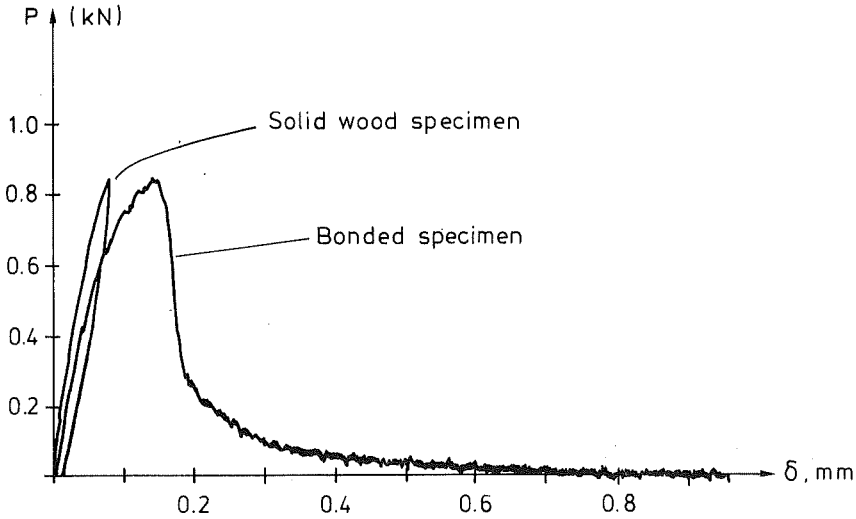
Figure 3.11: *Typical recorded load-deformation curve of bonded specimen and load-ing/unloading curve of solid specimen.*

wood specimen, and that the connection between steel and wood is perfect.

Uniform stress distribution is obtained by using a short bond line, only 5 mm. In addition, the bond line is shorter than the specimen, which reduces the possibility of wood failure and simplifies the attachment of the specimen to steel. Non-adhering PTFE-film (Teflon) was used to limit the length and to control the thickness of the bond. Linear elastic FE-analysis of the specimen verifies that a uniform stress distribution is satisfactorily obtained [7]. The adherend size was in the present test series $10 \cdot 20 \cdot 20$ mm^3, see Fig. 3.10. It was experienced that the test performance was improved if the wood volume was reduced. In later tests, see e.g. [79] such improvement was utilized.

In the present setup the deformation was recorded as the relative slip of the two steel grips, by clip gauges, which also were used for control of the testing machine. To transform the recorded force-slip curve of the specimen to a corresponding stress-deformation curve of the bond line, the specimen deformations outside of the bond line must be regarded. Therefore, loading/unloading tests were also performed on specimens of solid wood with cuts at the sides of the specimens in order to simulate the geometry of the glued specimens. In the evaluation of the
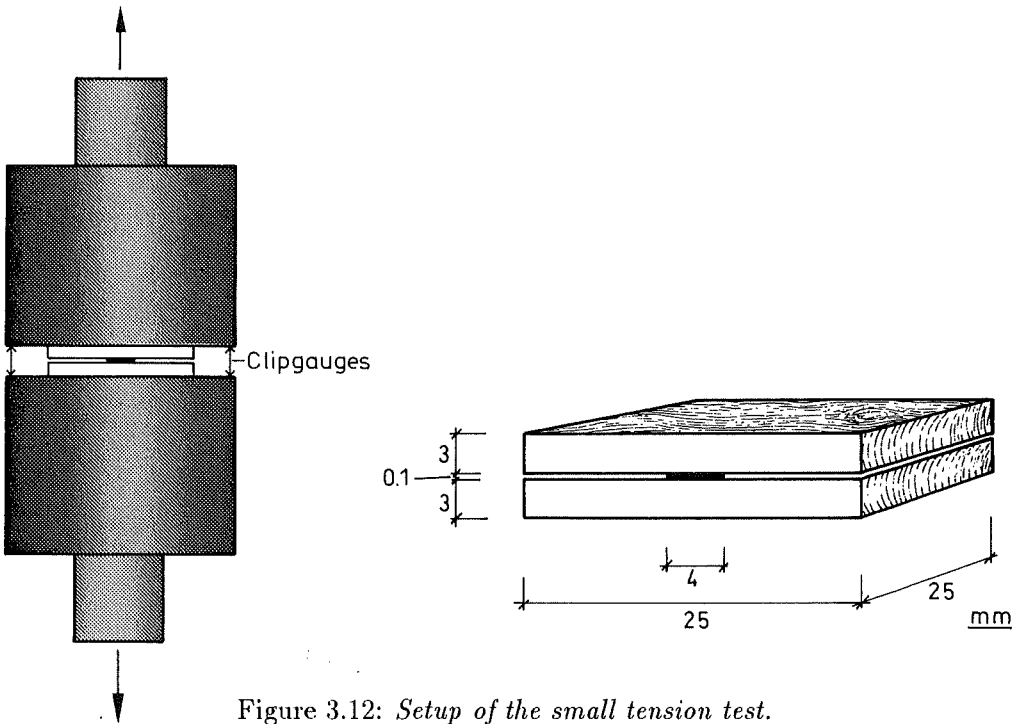
Figure 3.12: *Setup of the small tension test.*

stress-deformation curves of the bonded specimens, cf. Fig. 3.11, the deformation of the loading/unloading curves for solid wood is subtracted from the bond curves (the loading curve for the ascending branch and the unloading curve for the softening part). The possible small error in this evaluation will not affect the peak stress, τ_f. If the specimen outside of the bond line is assumed to be ideally elastic, the area below the curve, i.e. G_f, will not change. Hence, only the shape of the material curve might be slightly changed.

3.2.2. Small tension specimen setup

As for the shear specimen, the objective of the small tension specimen is to determine the complete stress-deformation relation in one single test. The method is more thoroughly presented in [98] and the setup and specimen geometry are given in Fig. 3.12. Two solid steel cylinders are mounted in the testing machine. The specimen is bonded between the cylinders with a fast-curing epoxy. This glueing procedure will increase the stiffness of the setup and counteract eccentric loading. To avoid wood failure beech was used as adherend material, and to limit the bond area PTFE-film was used.

The size of the bond is a compromise between being small enough to achieve uniform stress and large enough to reduce the influence of possible boundary effects.
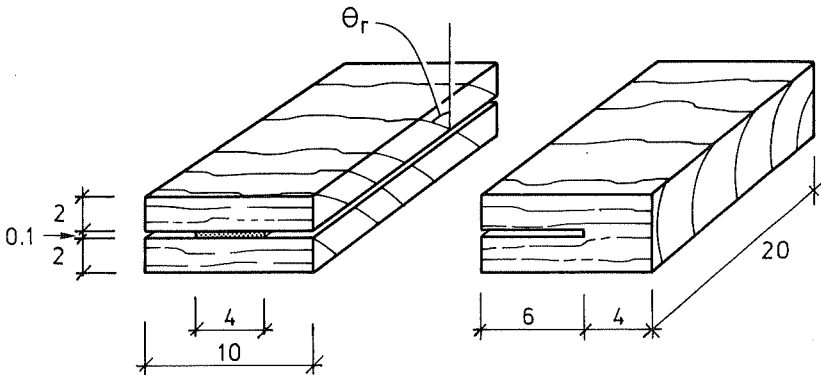
Figure 3.13: *Geometry of the small mixed-mode specimens.*

A small test series of four different bond sizes were performed which all gave similar results. In order to obtain to similarities to the shear specimen, a bond area of $4 \cdot 25mm^2$ was chosen. The load was applied with a constant loading rate of the two cylinders and the evaluation procedure was similar to that of the shear specimen including loading/unloading tests of pure wood.

3.2.3. Small mixed-mode specimen setup

The setup of the mixed-mode test, including the testing machine, is shown in Figs. 3.6 - 3.8. The size of the specimen is smaller than in the uniaxial tests to increase the overall stiffness outside of the fracture zone. Furthermore, the bond length was reduced from 5 to 4 mm at an initial stage of the test program. The specimen geometry is given in Fig. 3.13. There is a difference of the location of the fracture zone for the bonded specimen in comparison to that of pure wood. In the bonded specimen the bond line is placed in the middle of the specimen, while for the pure wood specimen the corresponding fracture area is at one of the sides. The latter choice is to prevent the wood failure area from growing larger than wanted.

The deformations are induced by pulling the linear bearings on which the specimens are attached, cf. Fig. 3.7. The deformation control signal is given by two LVDT-extensiometers measuring the relative displacements of the grips mounted on the bearings, in their respective directions. The load cell is built in on the lower grip of the specimen, cf. Fig. 3.7. It is designed as a four column frame on which strain gauges are attached in such a way that the normal and the shear strains can be separated and transformed into corresponding loading measures. The testing machine, including its signal processing and software, is at this date still in a development phase. A disturbingly high level of noise in the signals has been considerably reduced since the test series was completed. In the evaluation it has often been a process of determining means of noisy signals which may involve errors. Accordingly, some of

the quantitative values given in Sec. 4.2.3 should be handled with some care, but there is no reason to question the overall qualitative results of the test series.

The specimen has different stiffness in normal and shear direction which implies that the ratio between normal and shear deformations in the fracture zone will differ from that of the bearings. In addition, the fracture zone will change its stiffness during the tests. In the beginning the stiffness will be fairly large and positive while during the softening the incremental stiffness will be negative. This implies that for deformation control on the bearings the ratio of normal to shear deformation in the bond will vary during the test. This topic is further discussed in Sec. 4.2.3. In the evaluation of the present test series the aim has been to define the shear to normal deformation ratio in the bond line to be the initial mean shear to mean normal deformation ratio of the fracture zone.

The stiffness of the specimen outside of the bond line and the machine was determined from loading/unloading tests of wood specimens with the same geometry as for the bonded specimen. The recorded stiffnesses were approximately 1.2 and 2.0 MN/m in normal and shear direction, respectively. In the previous small specimen tests, the difference of the loading and unloading curves was accounted for in the evaluation. In the present series this difference was considered to be small and was not accounted for in the evaluation.

3.3. Verification and Fracture Propagation Tests

To verify the results from the small size specimens and to confirm theoretical considerations in the analysis, longer specimens with non-uniform stress states have been used. By choosing specimens with appropriate brittleness the influence of strength and fracture energy can be studied. For brittle joints the maximum load capacity will be independent of bond strength, and these methods can therefore advantageously be used for determination of bond line fracture energy, provided that the adherend stiffness is known.

3.3.1. Large shear specimen

The concept of the large shear specimen, illustrated in Fig. 3.14, has previously and more thoroughly been presented in [98]. The loading is applied anti-symmetrically with respect to the symmetry axis of the specimen. The bond line will, due to this, be in a state of pure shear. The bond line will as well get a curved shape when loaded antisymmetrically. This is because one adherend is exposed to tensile stress while the other is exposed to compressive stress. This bending effect is accounted for by choosing the parameter γ in Eq. (2.24) to be 0.5. Hence, the normalized strength takes the form

$$\frac{P_{max}}{\tau_f b\ell} = \frac{\tanh(2\omega)}{2\omega} \tag{3.1}$$
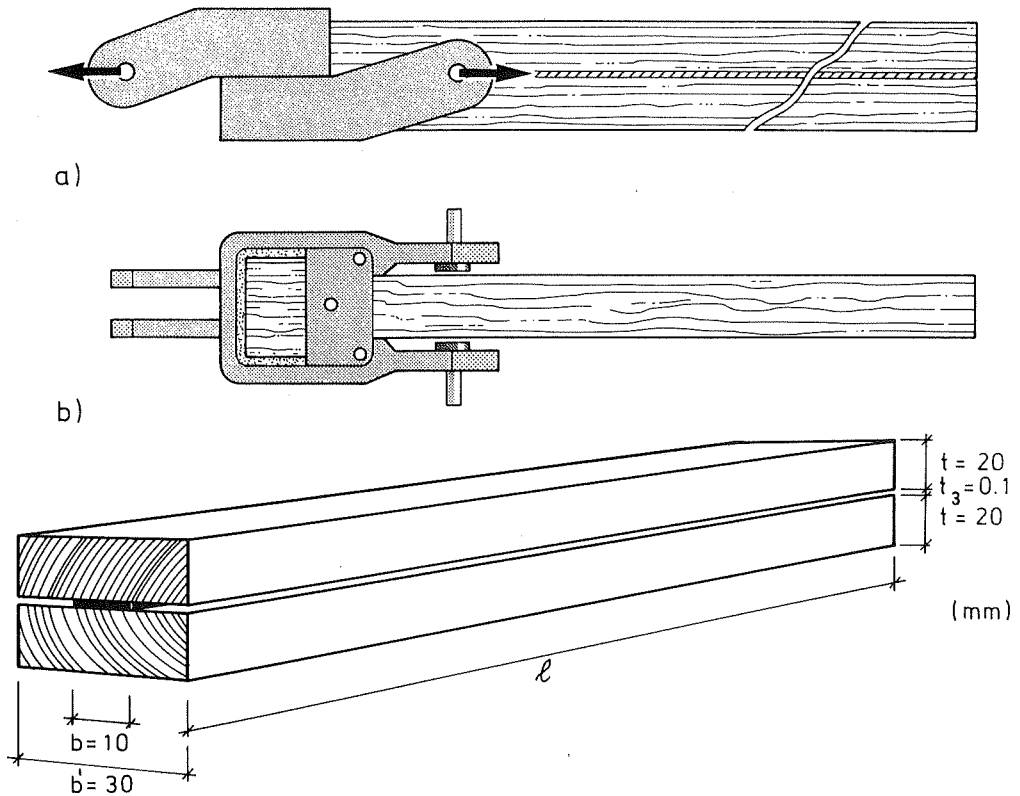
Figure 3.14: *Geometry and anti-symmetric loading of the large shear specimen.*

with the brittleness ratio, ω, defined as

$$\omega^2 = \frac{\ell^2}{t(b'/b)E} \cdot \frac{\tau_f^2}{G_f} \tag{3.2}$$

where (b'/b) is the ratio of adherend to bond line width, i.e. an increased adherend width may be compensated by increasing the adherend stiffness in the analysis.

For sufficiently large brittleness ratios the normalized joint strength will be proportional to ω^{-1}, i.e the maximum load carrying capacity can be expressed as

$$P_{max} = \frac{1}{2}\sqrt{b'btEG_f} \tag{3.3}$$

Accordingly, P_{max} is independent of ℓ and τ_f. The only material properties of relevance are the adherend stiffness modulus, E, and bond line fracture energy, G_f. During a crack propagation the applied load will theoretically reach a plateau
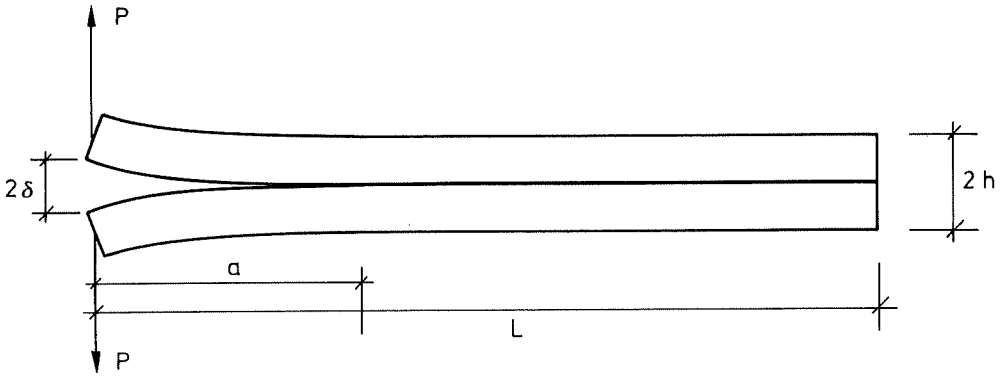
Figure 3.15: *Double cantilever beam (DCB) specimen.*

value with a constant magnitude of P_{max} and deviations from this level may thus be interpreted as variations of $\sqrt{EG_f}$ along the bond line.

The corresponding shear slip at the point of load application can be expressed as

$$\delta = \frac{8P\ell}{Etb'} \left\{ \frac{a}{\ell} + \frac{\coth 2\omega(1 - a/\ell)}{2\omega} \right\} \tag{3.4}$$

where δ is the relative displacement at the loading points and a is the crack length [98]. Since there are no transverse shear forces in the adherends, the shear stiffness of the adherend material will not affect δ nor P_{max}. This means that the above equations refer to both isotropic and orthotropic materials. From stability considerations, cf. Eq.(3.10), the large shear specimen may be considered as stable except for the end of the crack propagation and insensitive to variations of the stiffnesses of the testing machine and the grips.

3.3.2. Large tension specimen

One of the most commonly used cleavage (mode-*I*) tests is the double cantilever beam, DCB, specimen, which has also been adopted in the codes, e.g. ASTM D 3433. The specimen, shown in Fig. 3.15, consists principally of two bonded beams slit apart by two equal forces, P. The evaluation is based on the compliance method, cf. Sec. 2.3.3. The compliance is here defined as $C = \delta/P$, and it is determined by means of beam theory or FEM. From Eq. (2.11) the energy release rate is given as

$$G_c = \frac{1}{2}P_{max}^2 \left(\frac{dC}{dA} \right) \tag{3.5}$$

In *ASTM D 3433* an expression for the compliance, C, of the DCB specimen is given as

$$C = \frac{8a^3}{Ebh^3}\left(1 + \left(\frac{h}{a}\right)^2\right) \tag{3.6}$$

originating from *Mostovoy et al.* [67]. It includes bending and shear deformations of the isotropic free beam ends of length a, with $\nu = 0.3$. In testing it is commonly observed that the crack propagation will be partly unstable, implying the recorded load-deflection curve to be notched. In ASTM it is suggested that the crack arrest fracture toughness is evaluated as a mean of characterizing the bond material. This arrest fracture toughness will be influenced by the material properties but it is to a large extent a measure of the stability of the setup and, hence, its magnitude will predominantly depend on the stiffness properties of the specimen, the testing machine and the grip arrangements.

The total deflection, δ, will not only be due to bending and shear deformations in the beams. Rotations of the initially vertical beam cross section at the crack tip and the deformation of the bond line may also have significant influence. In references [25, 61] résumés are given of various expressions of C for the DCB specimen found in the literature. *Kanninen* [51] has given a solution for an isotropic beam, with a crack length a and assuming that the rest of the beam is resting on an elastic foundation at length $\ell - a$. Then

$$C = \frac{8a^3}{Ebh^3}\left\{1 + \frac{3\sqrt{5}}{4}\left(\frac{h}{a}\right) + \frac{2}{3}\left(\frac{h}{a}\right)^2 + \frac{3\sqrt{5}}{16}\left(\frac{h}{a}\right)^3\right\} \tag{3.7}$$

where the foundation modulus, k, is associated to the stiffness of the adherends as $k = 2Eb/h$. Eq. (3.7) is valid when $\ell - a$ is large in comparison to h. For orthotropic materials *Ashizawa* [5] modified Eq. (3.7) to include the ratio of longitudinal to transverse stiffness moduli,

$$C = \frac{8a^3}{E_1 bh^3}\left\{1 + 1.92\left(\frac{E_1}{E_2}\right)^{\frac{1}{4}}\left(\frac{h}{a}\right) + 1.22\left(\frac{E_1}{E_2}\right)^{\frac{1}{2}}\left(\frac{h}{a}\right)^2 + 0.39\left(\frac{E_1}{E_2}\right)^{\frac{3}{4}}\left(\frac{h}{a}\right)^3\right\} \tag{3.8}$$

where E_1 and E_2 are the longitudinal and transverse stiffness moduli respectively, and the coefficients inside the braces are empirically determined for orthotropic fibre composites. From Eq. (3.8) it follows that the energy release rate may be determined from the expression

$$G_{Ic} = 12\frac{P_{max}^2 a^2}{E_1 b^2 h^3}\left\{1 + 1.28\left(\frac{E_1}{E_2}\right)^{\frac{1}{4}}\left(\frac{h}{a}\right) + 0.41\left(\frac{E_1}{E_2}\right)^{\frac{1}{2}}\left(\frac{h}{a}\right)^2\right\} \tag{3.9}$$
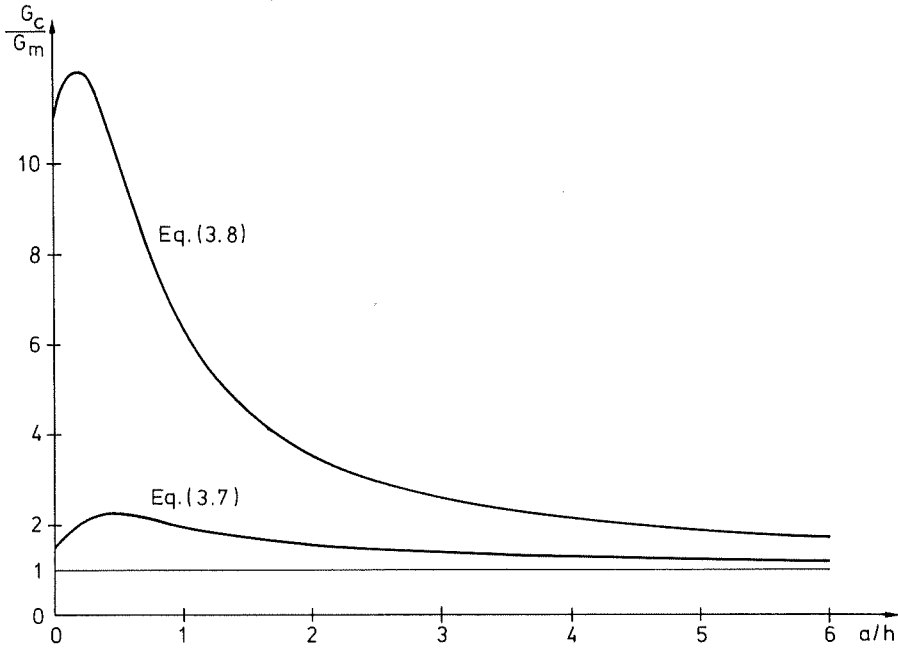
Figure 3.16: *Normalized critical energy release rate G_c versus a/h. $E_1/E_2 = 81$. G_m is the critical energy release rate based on Eq. (3.6).*

Similar solutions for specimens of orthotropic materials are given by *Bao et al.* [6] and *Komatsu et al.* [55]. Also visco-elastic behaviour of the bond line is included in [55].

In the evaluation of test results, the choice of compliance might be crucial. In Fig. 3.16, the fracture energy evaluated from Eqs. (3.7) and (3.8), normalized with respect to the values obtained by Eq. (3.6) and plotted versus the ratio a/h. For small a/h the evaluated critical energy release rate G_c is more than ten times as high for Eq. (3.8) than for Eq. (3.6). Accordingly, the compliance should be carefully determined for the type of specimen used.

The load, P_{max}, in Eq. (3.5) is a theoretical maximum load, assuming e.g. that the fracture process zone has infinitesimal size. The recorded load-displacement curve, in Fig. 3.17, suggests that P_{max} is in the range of 150 N. However, for a theoretical curve fitted to the test result, the maximum load capacity is in this case approximately 30 % larger, and as G_c depends on P_{max} squared an expected underestimation of G_c is about 40 %.

It is from the evaluation point of view desirable to obtain a smooth load-deflection curve similar to the theoretical curve in Fig. 3.17. A condition for stable crack propagation is given by *Hellan* [43],
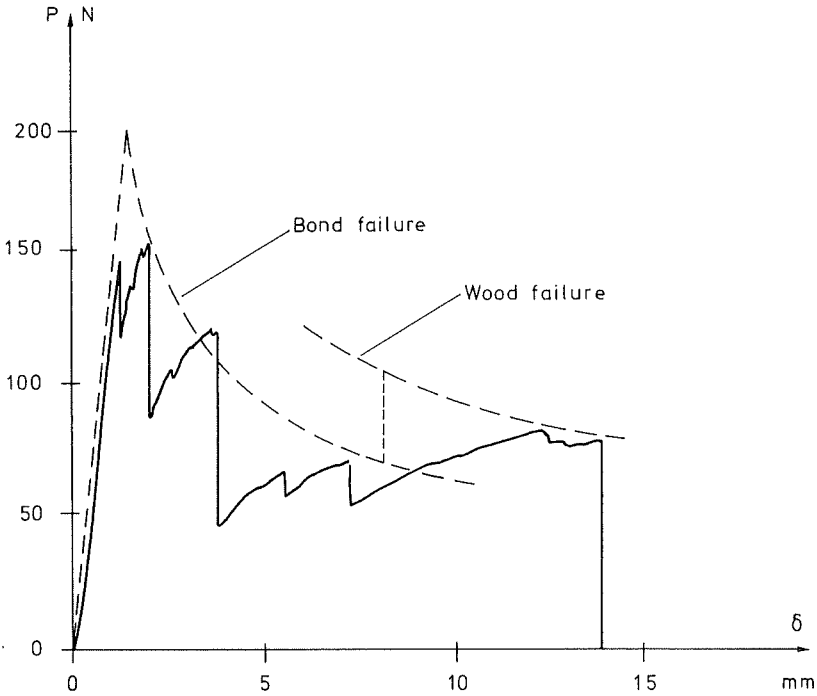
Figure 3.17: *Evaluation example for resorcinol/phenol bonded DCB specimen. In the end of the test the crack moved into the wooden adherends, yielding a larger fracture surface and thus adopting a curve at a higher level.*

$$\frac{\partial \left(G - G_c\right)}{\partial A} \leq 0 \tag{3.10}$$

Assuming G_c to be constant, its derivative will be zero and, hence, the change of G with respect to a will form a stability criterion for the specimen. With G_c constant, Eqs. (3.10) and (3.5) give us stable crack propagation if

$$\frac{dG}{dA} = \frac{1}{2}\frac{d}{dA}\left(P^2\frac{dC}{dA}\right) \leq 0 \tag{3.11}$$

For displacement controlled test conditions the energy release conditions are analysed for constant δ. With $P = \delta/C$, Eq. (3.11) may be written as

$$\frac{P^2}{2}\left(\frac{d^2C}{dA^2} - \frac{2}{C}\left(\frac{dC}{dA}\right)^2\right) \leq 0 \tag{3.12}$$

With a specimen compliance based on Eq. (3.8), the stability criterion of Eq. (3.12) for the DCB-specimen will always be satisfied. However, if the compliance of the
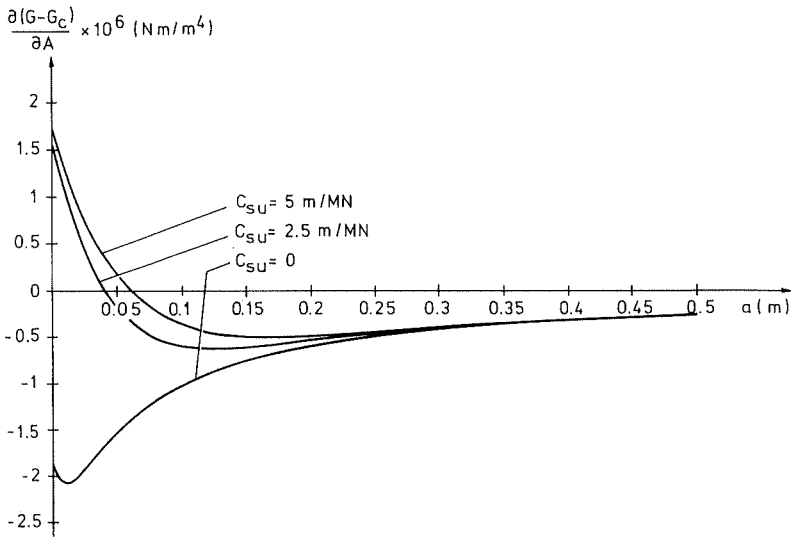
Figure 3.18: *Stability of a DCB specimen, with $C_{su} = 0$, 2.5 and 5 m/MN, respectively.*

testing machine and test setup, C_{su} is included the inequality may not be fulfilled. This is considered in Fig. 3.18 for some different values of C_{su} for the case of $E_1 = 13$ GPa and $E_2 = 0.16$ GPa. Accordingly, the stiffness of the setup may be of significance in the performance of the test and the initial crack length should be sufficiently large. Another property that will influence the stability is the change in $\sqrt{EG_c}$. A variable G_c can be included in Eq.(3.10), while a variation in adherend stiffness must be included in the deduction of the compliance. Such variations has not been considered in the present study.

From the evaluation point of view, it would be preferable if the recorded load-displacement curve would take the plateau form as for the large shear specimen in the previous section. This can be achieved by changing the geometry of the specimen as suggested by ASTM D 3433 for the contoured double cantilever beam (CDCB) specimen. The specimen is designed to have a compliance linearly dependent on a, implying the peak load, P_c, to be constant during the test. The spread in stiffness properties of wood and the difficulty of obtaining a theoretical value of C, suggest that the specimen should be experimentally calibrated before use. *River and Okkonen* [81] use a contoured specimen made of oriented strandboard sandwiched to a wood laminate having the test bond line in its centre. The strandboard part predominates the stiffness of the specimen and it is calibrated and reused for several

tests. Other materials such as aluminium may also be used in composite specimens, as suggested by *Scott and River* [85].

A different approach to obtain a plateau shape of the load-deflection curve is to change the loading. The magnitudes of the stresses at the crack tip depend on the applied load, P, times its lever a. If instead the load is applied as a moment the stresses at the crack will be independent of the crack length. This is illustrated in Fig. 3.19. From a stability viewpoint it may be advantageous to combine the moment load with the contoured geometry. If e.g. a deviation in material properties causes a steep but stable notch in the upper response curve of Fig. 3.19, the same deviation will yield a considerably less severe irregularity of the curve for the lower response curves.

From a more direct energy approach the fracture energy, G_f, may be evaluated as the energy dissipation during the total failure process of the specimen. This approach is described in [29] and was used in [12] for a short wooden DCB-specimen, i.e. a compact tension CT-specimen. In the latter reference an approximate method to deal with the theoretically very long tail of the $P - \delta$ curve for the CT-specimen is described.

Assuming negligible dead-weight of the specimen, the dissipated energy during the fracture of the specimen will be equal to the area below the recorded $P - \delta$ curve, that is

$$G_f = \frac{1}{A_{tot}} \int_0^\infty P d\delta \qquad (3.13)$$

where A_{tot} is the total bond area. In practice the complete $P - \delta$ curve will generally not be recorded, due to local instabilities, and hence, the "true" area must be approximated in one way or another.

3.3.3. Large mixed-mode bending (MMB) specimen

Mixed-mode testing is complicated as it is difficult to obtain a setup only including two unequivocally defined, perpendicular stress or deformation modes. In addition, verification tests on large specimens are preferably made in a standard uniaxial testing machine, and the mixed-modity of the stress state should hence depend on specimen geometry and the point and direction of loading. In the literature there are various mixed-mode crack propagation specimens presented to be used for e.g. metal and composites. Two such methods are given in Fig. 3.20. The four-point bending specimen was suggested by *Charalambides et al.* [17] and further analysed in [18]. It will theoretically expose a plateau-shaped load-deflection curve at propagating failure; the mixed-modity, ψ_K, will depend on the geometry but will be in the range of 45°. The mixed-mode flexure specimen (MMF) [83], is a DCB specimen loaded in bending and may be considered to be a combination of the ENF shear specimen (mode-II) [83] and the DCB cleavage specimen (mode-I). The mixed-mode state is achieved by supporting the cracked side of the ENF specimen
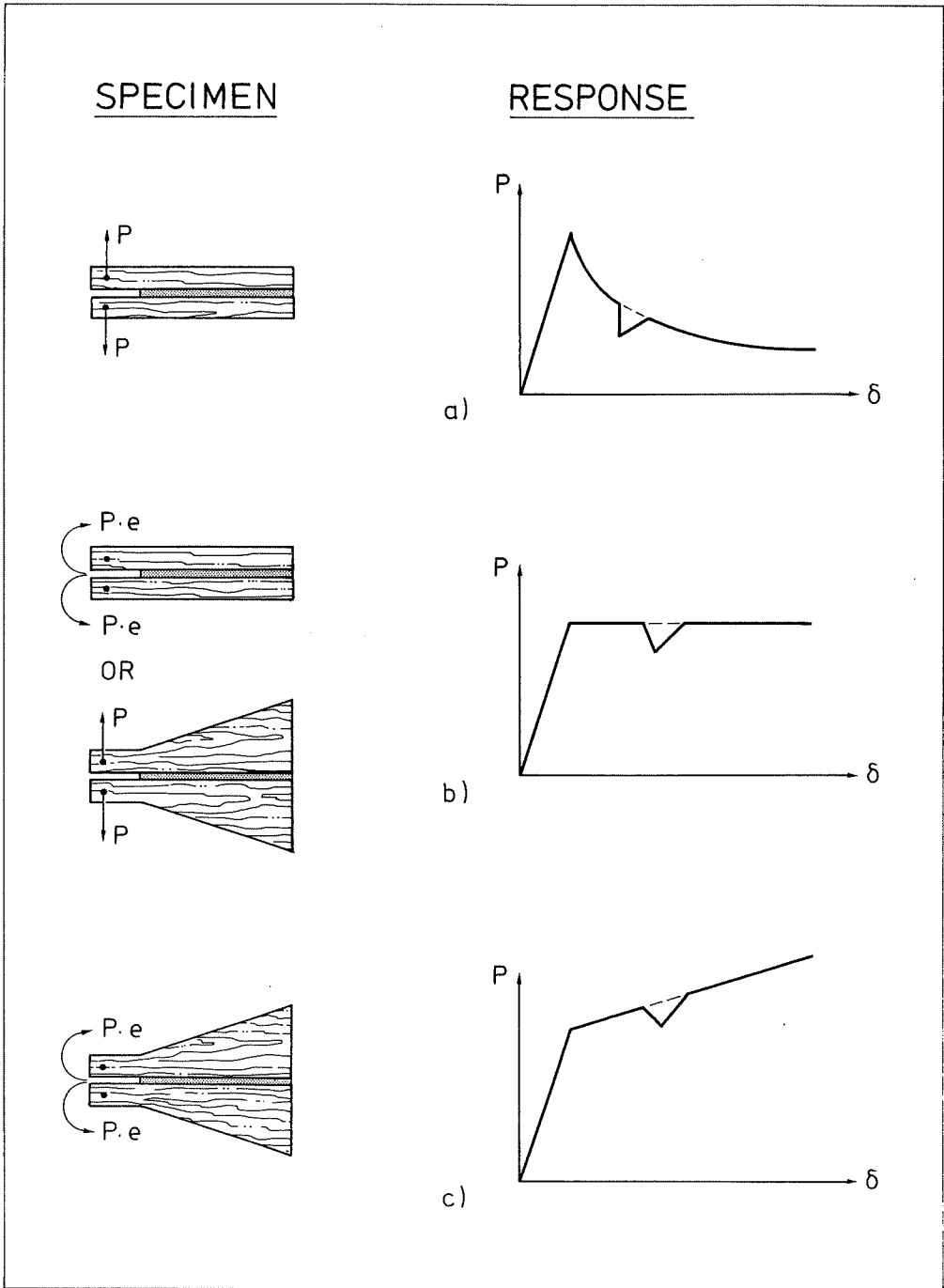
Figure 3.19: *Alternative geometry and loading of the double cantilever beam, DCB, specimen.*
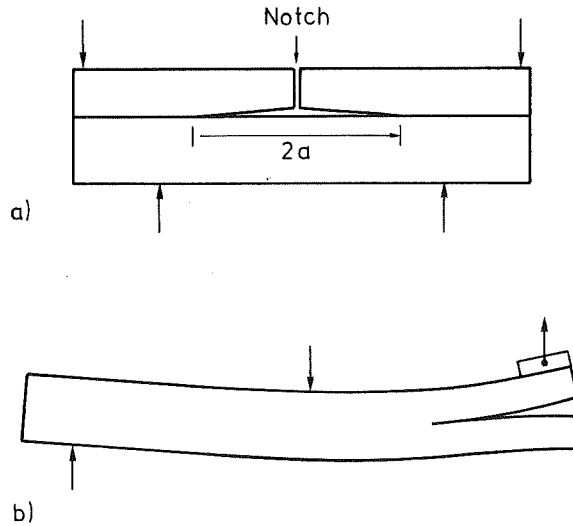
Figure 3.20: *Mixed-mode crack propagation specimens. (a) Four-point bending notched specimen. (b) Mixed-mode flexure specimen, MMF.*

on the upper adherend instead of the lower. The MMF specimen will expose a similar load-deflection response curve as that of the DCB specimen discussed in the previous section, which implies the evaluation to be done with a precautionary measure. Likewise for a combination of mode-I and mode-III loading of the DCB specimen, which has been proposed by *Chai* [15].

In the present study a mixed-mode bending specimen (MMB) is proposed, which is a combination of the large shear specimen and the moment-loaded DCB specimen [97]. Two different configurations are given in Fig. 3.21. For both specimens the force-deformation curve will expose a plateau shape, which is positive from an evaluation point of view. The mode-mixity will be proportional to the eccentricity of the applied load. In the upper specimen the adherends will be exposed to pure bending, but there will be a geometric second-order effect due to increasing separation at crack propagation. For the lower specimen the steel grips will be in contact and rotate on two steel balls. The free adherends will be statically indetermined with a shear force due to the contact reaction. The shear deformations in the beams will be negligible in comparison to bending deformations for sufficiently large crack lengths, a. In the present test programme, only the configuration of Fig. 3.21b has been used and thoroughly analysed.

The geometry of the MMB specimen is identical to that of the shear specimen, cf. Fig. 3.14, with a bond length of 350 mm and an initial crack length of 100 mm. The wood specimen is glued into the steel grips which are joined by two steel
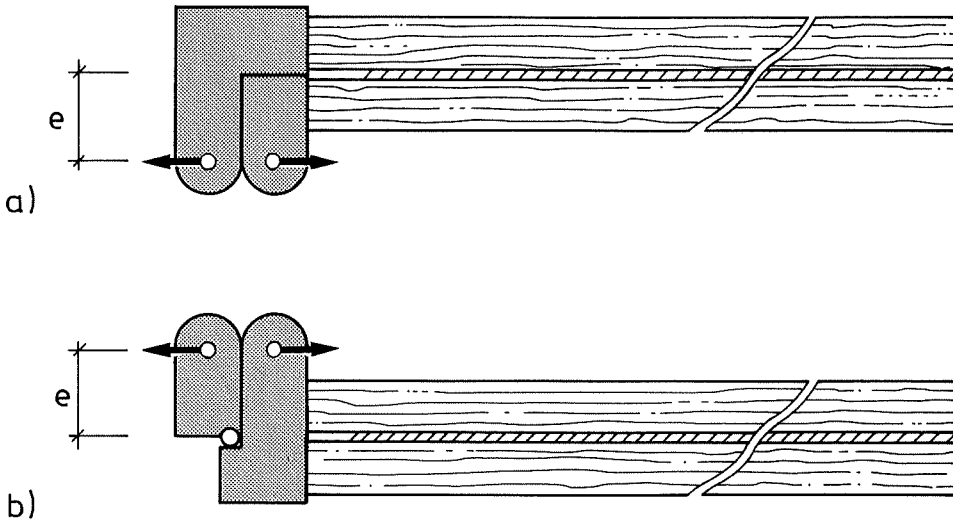
Figure 3.21: *Mixed-mode bending specimens.*

balls. The steel grips are loaded in tension, in accordance with Fig. 3.21b. The load case may be separated into a pure mode-I and a pure mode-II loading, which is illustrated in Fig. 3.22. By means of conventional beam theory and linear elastic fracture mechanics, the energy release rates of the two modes are given as

$$G_I = 3\frac{P^2}{Eb'bh}\left(\frac{e}{h}\right)^2 + \text{ shear force effects} \tag{3.14}$$

$$G_{II} = 4\frac{P^2}{Eb'bh} \tag{3.15}$$

P is the load applied with an eccentricity e, E is the elasticity modulus of the adherends in bending, b and b' are the widths of the bond and the adherends respectively, and h is the thickness of the adherends. For sufficiently large a, i.e. the shear deformations can be neglected, the ratio of G_I to G_{II} may be expressed as

$$\frac{G_I}{G_{II}} = \frac{3}{4}\left(\frac{e}{h}\right)^2 \tag{3.16}$$

Accordingly, for zero eccentricity, $e = 0$, it will be in a state of pure shear, and the test will be identical to that of the pure shear specimen, while for large values of e, the stresses will converge towards a pure mode-I state.

The test is run at a constant rate of stroke. For a sufficiently long joint, according to Eqs. (3.14) and (3.15) the force that propagates the crack will reach a plateau
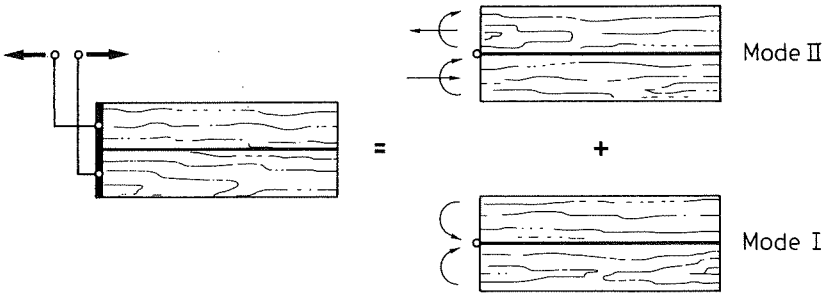
Figure 3.22: *Decomposition of the applied load in mode-I and mode-II.*

level. To evaluate G_{Ic} and G_{IIc} some mean value of the plateau force is to be inserted into Eqs. (3.14) and (3.15).

According to Eqs. (3.14) and (3.15) the maximum bending stresses in the pure modes can be expressed as

$$\sigma^I_{max} = \sqrt{\frac{12EG_{Ic}b'}{bh}} \qquad\qquad (e \to \infty) \qquad\qquad (3.17)$$

$$\sigma^{II}_{max} = \frac{3}{4}\sqrt{\frac{EG_{IIc}b'}{bh}} \qquad\qquad (e \to 0) \qquad\qquad (3.18)$$

Hence, the bending stresses will be highest in mode-I testing as long as $G_{IIc} \leq \frac{16}{3}G_{Ic}$. The magnitude of the stresses in mixed-mode testing are not known as a proper failure criterion; this is yet to be determined. Eqs. (3.17) and (3.18) imply that the adherend bending stresses can be reduced by decreasing the ratio b'/b, or by increasing the thickness of the adherends, e.g. an increase of h from 0.02 m to 0.03 m yields a decrease of σ by more than 20 %. Alternatively, the bending strength may be increased by reinforcing the adherends with e.g. strips of fibreglass.

For all fracture propagation specimens with wood adherends, the variation of adherend stiffness along the bond line must be handled in one way or another. As for the DCB specimen, it is possible to make a composite MMB specimen. For a wood-aluminium specimen Eqs.(3.14) and (3.15) will take the form

$$G_I \;\; = \;\; \frac{3}{4}\frac{P^2e^2}{b(EI)_{comp}} + \text{shear effects} \qquad\qquad (3.19)$$

$$G_{II} \;\; = \;\; \frac{P^2}{b}\left(\frac{1}{(EA)_{comp}} + \frac{(h_w + h_n)^2}{(EI)_{comp}}\right) \qquad\qquad (3.20)$$

where h_w and h_{al} are the wood and aluminium thicknesses, respectively, given in
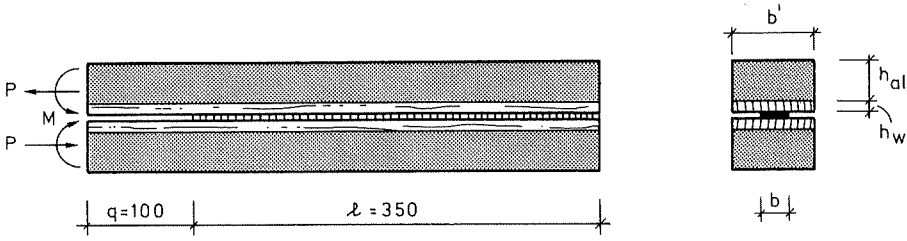
Figure 3.23: *Geometry of composite MMB specimen.*

Fig. 3.23 and the composite stiffnesses are given by

$$(EI)_{comp} = E_{al}\frac{b'}{3}\left\{h_n^3 + (h_{al} - h_n)^3 + \frac{E_w}{E_{al}}\left[(h_w + h_n)^3 - h_n^3\right]\right\} \quad (3.21)$$

$$(EA)_{comp} = b'(E_{al}h_{al} + E_wh_w) \quad (3.22)$$

in which h_n is the distance from the wood-to-aluminium interface to the neutral axis of the beam, expressed as

$$h_n = \frac{1}{2}\frac{E_{al}h_{al}^2 - E_wh_w^2}{E_{al}h_{al} + E_wh_w} \quad (3.23)$$

To obtain a bending stiffness like that for the pure wood specimen, i.e. $h = 20$ mm, $h_w = 3$ mm and $h_{al} = 11$ mm are appropriate thicknesses. Assuming $E_{al}/E_w = 6$, a 10 % change in E_w yields only a 1.2 % change in $(EI)_{comp}$.

The shear deformation term in Eq. (3.19) may be evaluated by means of energy considerations. For an arbitrary cross section the shear deformation of a cantilever beam can be expressed as

$$\delta_{shear} = \beta \cdot \frac{VL}{GA} \quad (3.24)$$

where V is the shear force, G is the shear modulus, L is the beam length (in the present case, the crack length, a) and A the cross sectional area of the beam. β is a parameter determined by the shape of the cross section. For a rectangular section, $\beta = \frac{6}{5}$ and for other shapes β can be found in handbooks. Correspondingly, β may consider the composite effects of the present specimen and we get

$$\delta_{shear}^{comp} = \beta_{comp} \cdot \frac{VL}{(GA)_{comp}} \quad (3.25)$$

where by means of the energy method, see e.g. [73], β_{comp} can be derived to take the form

$$\beta_{comp} = \frac{1}{3}C_s\frac{(GA)_{comp}}{(EI)_{comp}} \quad (3.26)$$

for which $\mathcal{C}_s$ takes the rather inconvenient form

$$
\mathcal{C}_s = \frac{3}{4} \frac{b'}{(EI)_{comp}} \left\{ \frac{8}{15} \frac{E_{al}^2}{G_{al}} \left(h_u^5 + h_n^5 \right) + \frac{4}{3} \frac{E_{al} E_w}{G_{al}} h_n^3 \left(h_l^2 - h_n^2 \right) + \frac{E_w^2}{G_{al}} h_n \left(h_l^2 - h_n^2 \right)^2 + \right.
$$

$$
\left. \frac{E_w^2}{G_w} \left(\frac{8}{15} h_l^5 - h_l^4 h_n + \frac{2}{3} h_l^2 h_n^3 - \frac{1}{5} h_n^5 \right) \right\} \tag{3.27}
$$

where $h_u = h_{al} - h_n$ and $h_l = h_n + h_w$. Accordingly, the mode-I energy release rate may be written as

$$
G_I = \frac{1}{4} \frac{P^2 e^2}{b(EI)_{comp}} \left\{ 1 + \frac{3\mathcal{C}_s(\mathcal{C}_s - a^2)}{(a^2 + \mathcal{C}_s)^2} \right\} \tag{3.28}
$$

The corresponding expression for pure wood adherends, i.e. Eq. (3.14) including shear terms, is

$$
G_I = 3 \frac{P^2}{E_w b' b h} \left(\frac{e}{h} \right)^2 \left\{ 1 + \frac{9 \left(\dfrac{E_w}{G_w} \right) h^2 \left(3 \left(\dfrac{E_w}{G_w} \right) h^2 - 10a^2 \right)}{\left(10a^2 + 3 \left(\dfrac{E_w}{G_w} \right) h^2 \right)^2} \right\} \tag{3.29}
$$

4. EXPERIMENTAL RESULTS

4.1. General Remarks

As a major result of the test programme, it will be shown in this chapter that adhesive joints expose gradual softening and that, with the suggested methods, it is possible to record the complete stress-deformation curves in pure shear and tension as well as in mixed-mode. The main objective of the experimental programme has been to evaluate the proposed test methods and to give some typical values of bond line characteristics with regards to non-linear fracture mechanics. Accordingly, little effort has been devoted to studying the influence of e.g. environmental influence on the bond line properties. Most of the uniaxial test results have previously been presented in e.g. [29, 98], but they are considered to have enough reference value to be recapitulated here.

4.2. Small Specimen Results

4.2.1. Small shear specimen results

The small shear test programme included 17 series of at least six specimens each and, in addition, three series of solid wood to determine specimen stiffness outside of the bond line. The parameters varied were type of adhesive, bond thickness, curing time and deformation rate. In addition, three series were performed to study the influence of formaldehyde content on the properties of resorcinol/phenol bonds.

In the first test programme, previously presented in [96], three different types of adhesive were used to comprehend a spread of adhesives on the market. They were a ductile one-component polyurethane (Casco 1809), an intermediate one-component PVAc (Casco 3304) and a brittle two-component resorcinol/phenol (Casco 1703+ 2624). The latter is the only adhesive that can be considered to expose structural abilities regarding long term loads, environmental effects, etc. The one-component adhesives are available in most carpenter stores and, hence, commonly used in diverse applications of non-structural bonding. All together these three adhesives represent, however, rather different chemical constitutions and they may represent a span in bond line characteristics to be expected in an arbitrary testing situation.

Two curing times and three different deformation rates were applied for each type of adhesive. Typical mean stress-deformation curves are given in Fig. 4.1 and for each adhesive mean stress-deformation curves are given in Figs. 4.2-4.4. In Tab. 4.1
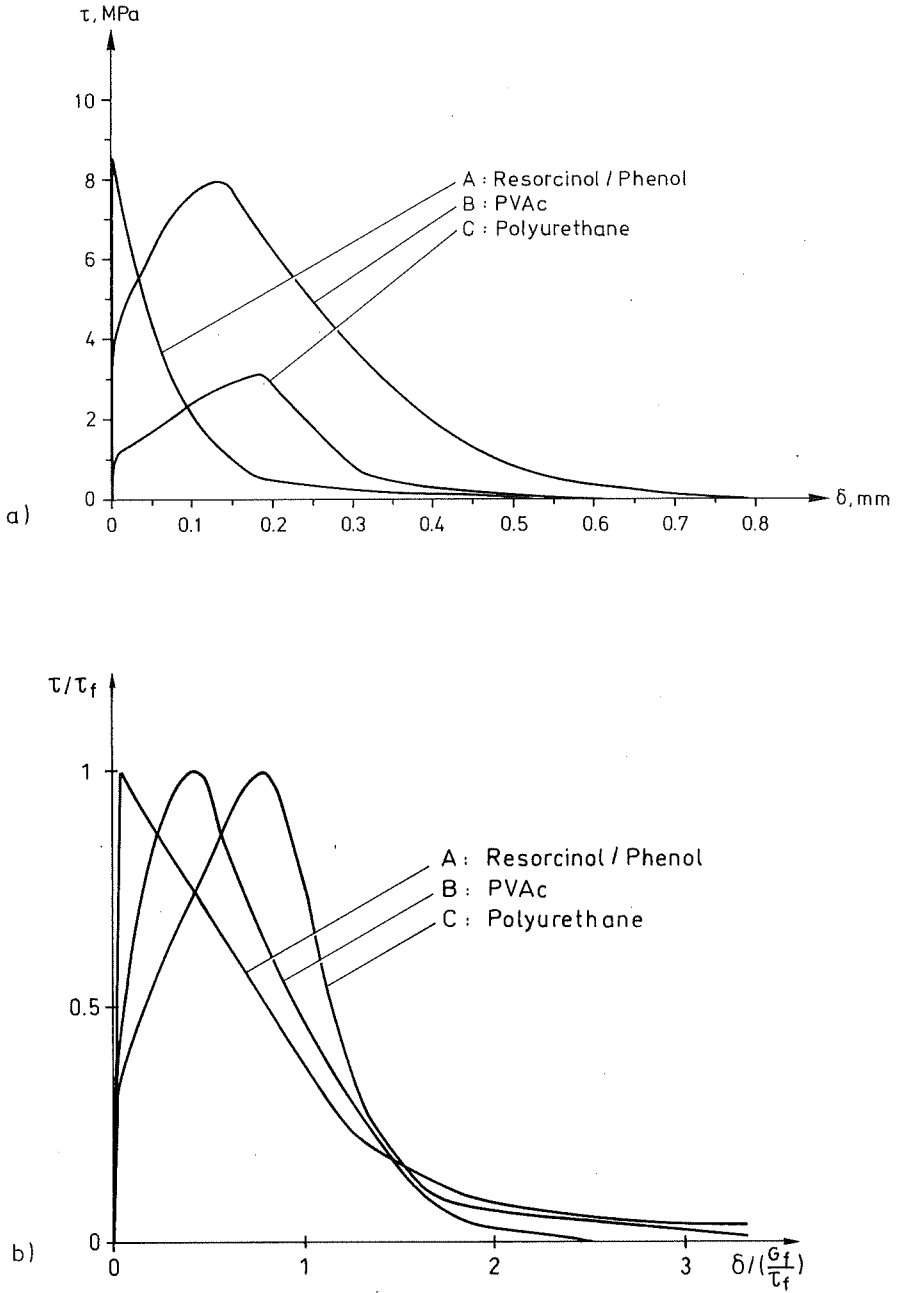
Figure 4.1: *Stress versus deformation for three different bond lines tested at constant conditions, deformation rate = 0.0625 mm/min, curing time = 4 days. a) $\tau - \delta_s$ curves. b) Normalized curves.*

Table 4.1: τ_f and G_f for 0.1 mm thick bond lines with different adhesives at different curing times in days (C) and different deformation rates in mm/min (R).

Adhesive	R	C	Number of tests stab/tot	τ_f [MPa]	G_f [kNm/m²]	τ_f^2/G_f [GPa/m]
PVAc	1.0	4	6/6	8.81±0.92	1.86±0.52	45.5
	0.25	4	6/6	8.78±0.60	1.70±0.29	46.2
	0.0625	4	6/6	7.36±0.79	2.11±0.2	26.0
	0.25	16	6/6	7.12±0.72	1.75±0.21	29.2
Poly-urethane	1.0	4	6/6	4.06±1.46	0.78±0.37	21.4
	0.0625	4	6/6	2.84±1.32	0.60±0.29	13.6
	0.0625	16	6/6	3.56±0.92	0.85±0.25	14.9
Resorcinol/phenol	0.25	4	2/6	8.78±0.60	1.00±0.07	80.1
	0.0625	4	4/6	8.38±0.67	0.70±0.11	98.7
	0.0625	16	3/6	8.28±1.47	0.48±0.04	162.5
Wood (Picea Abies)	0.0625	-	28/28	8.90±1.25	0.95±0.19	83.4

the corresponding material properties are quantitatively listed, including tests of European Whitewood (picea abies) made with the same test method but in relation to another project [79]. *Boström* [12] reported from tests with another test setup corresponding figures for Scots pine to be 10.9 ± 0.9 MPa and 0.83 ± 0.05 kNm/m² for shear strength and fracture energy, respectively. There is a similarity between the results from resorcinol/phenol bonds and those of pure wood, with regards to stress-slip curve shape as well as to the magnitude of the material parameters. These results suggest that testing resorcinol/phenol bonds is, in praxis, to a large extent a test of the adjacent wood material. By studying the failed surface it is noticed that a significant amount of wood fibres is involved in the fracture process, hence supporting this assumption.

In Tab. 4.1 τ_f, G_f and bond line ratio τ_f^2/G_f are given. The ratio τ_f^2/G_f is the bond line part of the brittleness ratio defined in Eq. (2.22) and hence a high ratio will indicate a brittle behaviour while a low ratio corresponds to more ductile
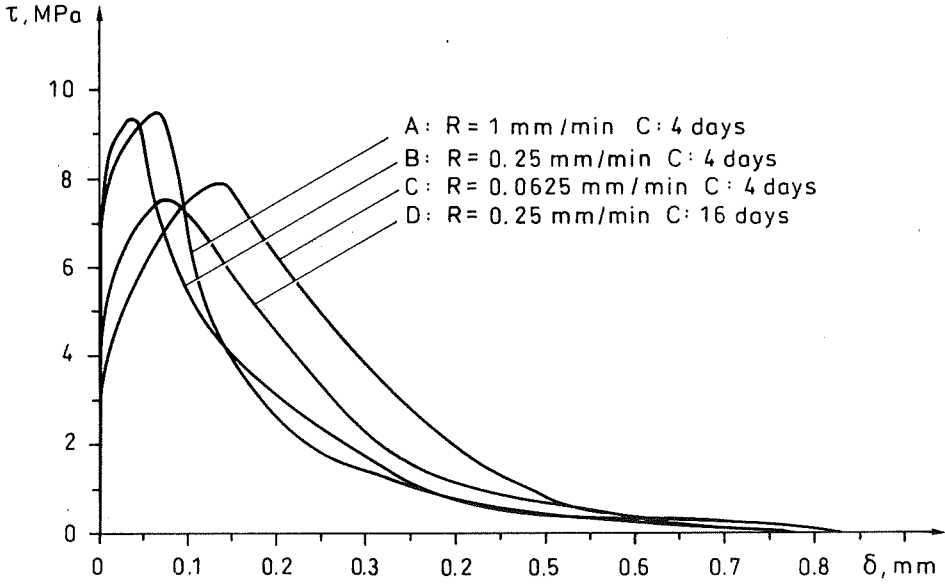
Figure 4.2: $\tau - \delta_s$ curves for PVAc, tested at different rates of deformation (R) and curing times (C).
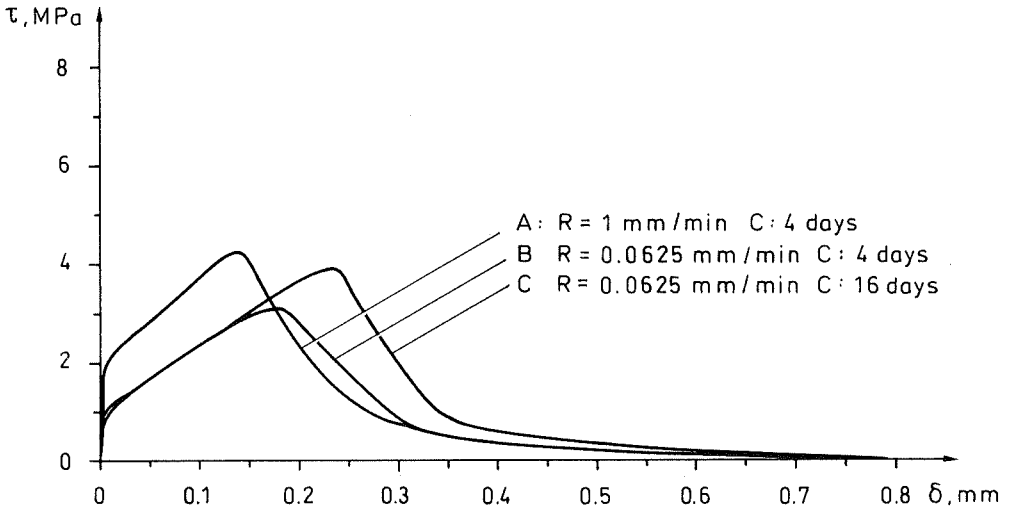
Figure 4.3: $\tau - \delta_s$ curves for polyurethane, tested at different rates of deformation (R) and curing times (C).
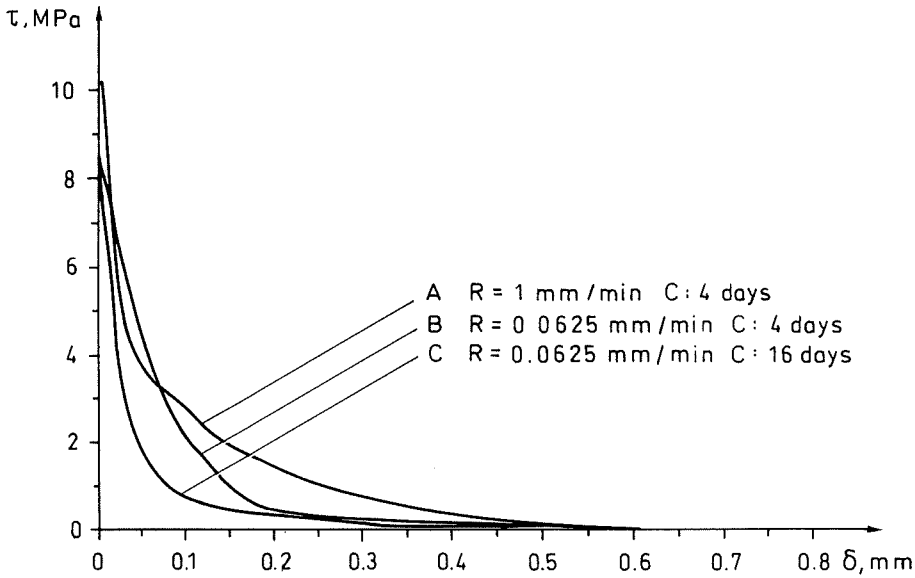
Figure 4.4: $\tau - \delta_s$ curves for resorcinol/phenol, tested at different rates of deformation (R) and curing times (C).

characteristics of the bond line. The different types of adhesives possess different ranges on a brittleness scale where the polyurethane bonds exhibit the toughest behaviour with a magnitude of the brittleness bond line ratio of approximately 15 GPa/m, while the brittle resorcinol/phenol bonds expose values about ten times higher.

There is an obvious difference in characteristic stress-slip performance of the three adhesives. In general the initial elastic deformations are almost negligible in comparison to the non-linear deformations. For resorcinol/phenol the major deformation occurs in the softening region while for polyurethane a considerable slip is observed in the hardening pre-peak stress region.

Due to their distinctive chemical constitutions, the adhesives react differently to the different testing conditions. The effect is schematically presented in Tab. 4.2. The three types of adhesive possess different curing mechanisms. PVAc cures by emitting solvents to the wood material, polyurethane cures by reaction to water applied in the glue line or absorbed from the adjacent material, while resorcinol/phenol primarily cures by chemical reaction of the two components. This may explain the different responses to curing time.

Increased deformation rate yields higher strength for PVAc and polyurethane. Such rate dependence is a common observation for polymeer materials. The brittleness is also increased for these bonds. However, for resorcinol/phenol the brittleness tends to decrease with increased deformation rate, which is rather surprising.

Table 4.2: *Effect of testing conditions on the bond line properties.*

Condition	Adhesive	τ_f	G_f	τ_f^2/G_f
Increased curing time	PVAc	⇑	∼	⇑
	PU	⇑	⇑	∼
	R/P	∼	⇓	⇑
Increased deformation rate	PVAc	⇑	∼	⇑
	PU	⇑	⇑	⇑
	R/P	∼	⇑	⇓

The coefficients of variation for PVAc are about 10 % in strength and approximately twice as large for fracture energy. For polyurethane and resorcinol/phenol, the approximate values are 40 % and 10 %, respectively, for both strength and fracture energy. The rather high deviation of polyurethane bond lines indicates that the present polyurethane adhesive is rather sensitive to the glueing conditions. One conceivable explanation is the possible lack of curing pressure in the bond line during hardening. Load carrying capacity, P_{max}, of lap joints may at most be proportional to τ_f and $\sqrt{G_f}$, cf. limit equations in Fig. 2.14. Hence, the effect of deviation is considerably smaller for fracture energy than for strength. A 40 % deviation as for polyurethane would consequently at most affect joint strength with a deviation of about $\sqrt{1.40} - 1.0 = 18$ %.

In the second test programme, including four series, the influence of bond thickness on the bond line parameters was tested for polyurethane and resorcinol/phenol. Two thicknesses were used; 0.1 mm and 0.25 mm. Stress-slip curves are presented in Figs. 4.5 and 4.6 and the evaluated parameters are given in Tab. 4.3. Increased thickness has a severe influence on the one-component polyurethane bond, while no significant influence was observed for resorcinol/phenol. Polyurethane cures by absorbing and reacting to water, and unless sufficient clamping pressure is applied, the bond will obtain a foamy character. In the case of 0.25 mm bonds, the Teflon film will act as a spacer and the thick polyurethane bond will not obtain sufficient pressure during curing.

In the two test programmes the same adhesives were used and also the test conditions were identical. From this point of view there is a surprisingly large difference between the results of the two identical series. For resorcinol/phenol the
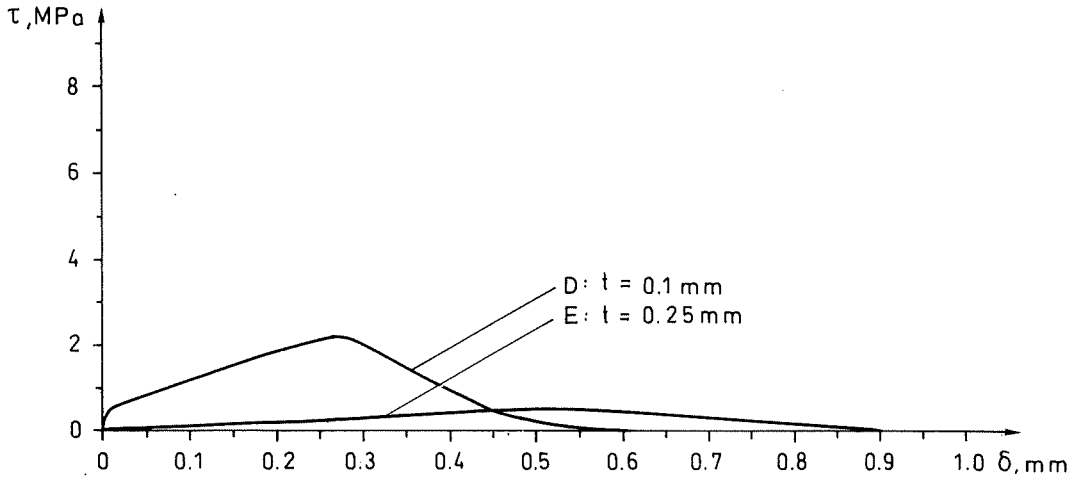
Figure 4.5: $\tau - \delta_s$ curves for polyurethane, tested with different bond thickness.
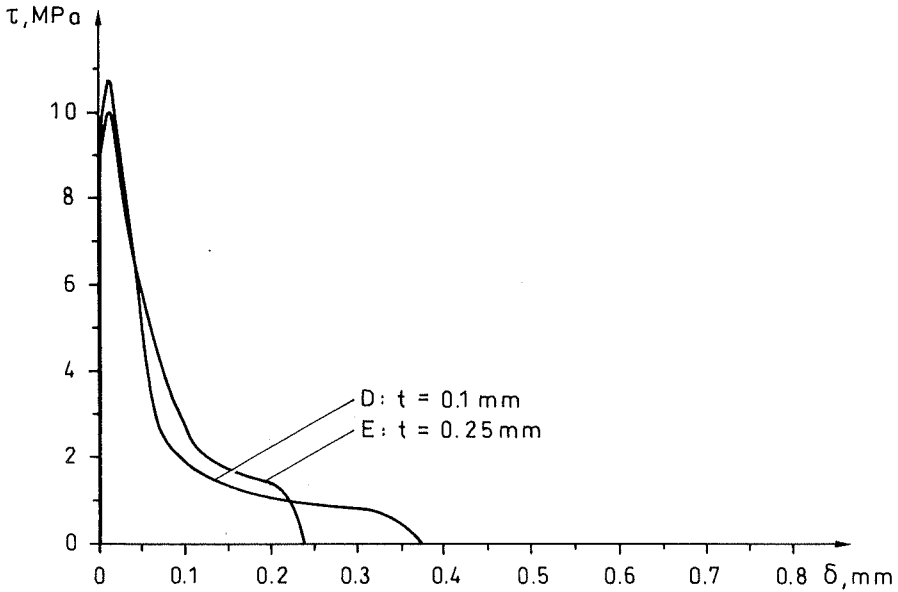
Figure 4.6: $\tau - \delta_s$ curves for resorcinol/phenol, tested with different bond thickness.

Table 4.3: *Influence of bond thickness on bond line parameters in shear. Deformation rate = 0.0625 mm/min.*

Adhesive	Bond thickness [mm]	Curing time [days]	τ_f [MPa]	G_f [kNm/m²]	τ_f^2/G_f [GPa/m]
Poly-urethane	0.10	40	2.15 ± 0.20	0.60 ± 0.04	7.8
	0.25	40	0.45 ± 0.06	0.18 ± 0.04	1.1
Resorcinol/-phenol	0.10	20	10.9 ± 0.60	0.85 ± 0.09	137
	0.25	20	10.0 ± 0.80	0.79 ± 0.14	131

strength was 30 % higher and the fracture energy approximately 20 % larger in the second series. This may be explained by the facts that different pots of glue were used and that in the latter series the two components were mixed by parts of weight instead of volume. However, from the discussion above, an important contribution may be different wood properties in the two series.

A third programme including three test series with six specimen each was made on resorcinol/phenol to evaluate the influence of formaldehyde content on the bond line properties [29]. The adhesive was Casco 1711+2620, which was tested at three different contents of formaldehyde in the hardener; 22.5 %, 40.0 % and 57.5 %. The mixing proportion was 1:5 by weight for harderner to glue. The recorded curve shapes were similar to those above for resorcinol/phenol, and the results are quantitatively given in Tab. 4.4.

There is a tendency for the bond line to become more brittle at increased formaldehyde content, mainly due to decreased fracture energy, G_f.

4.2.2. Small tension specimen results

The pure tension test programme was less ambiguous than that in pure shear. The main objective was to suggest an adequate method for determination of the complete stress-deformation curve in tension perpendicular to the bond line. No effort has been made to investigate the influence of testing conditions and environmental influence on the bond line properties.

The test programme consisted of two parts. The first part was to evaluate a proper geometry of the bond surface. Four different resorcinol/phenol bond geome-

Table 4.4: *Influence of formaldehyde content in the hardener on bond line parameters of resorcinol/phenol. Deformation rate = 0.0625 mm/min.*

Formaldehyde content [%]	τ_f [MPa]	G_f [kNm/m^2]	τ_f^2/G_f [GPa/m]
22.5	10.3 ± 0.6	0.71 ± 0.11	151.9 ± 22.5
40.0	10.6 ± 1.2	0.69 ± 0.16	167.8 ± 29.8
57.5	10.2 ± 0.4	0.56 ± 0.06	187.8 ± 25.1

tries were tested, shown in Fig. 4.7. To facilitate a straightforward evaluation of the test results, the stress distribution should be uniform. As an initial assumption, all four geometries were considered to exhibit a uniform stress state. Deviations in the test results would, accordingly, oppose this assumption or suggest that e.g. boundary effects or insufficient bond line stiffness implies non-uniform properties over the bond surface.

In the shear test programme it was observed that the results from resorcinol closely correspond to those of pure wood. In the tension programme it was decided to use beech (Fagus sylvatica) as adherend material to more likely obtain bond line properties predominantly influenced by the adhesive. A total of 15 specimens were tested in the initial part. Each specimen was cured for one week at 20°C and 65 % RH. The tests were run at a deformation rate of 0.0625 mm/min; for three of the specimens the exposed failure was partly unstable and, consequently, no fracture

A = 10 × 10 mm^2 A = 5 × 5 mm^2 A = 4 × 25 mm^2 A = 2 × 12 5 mm^2
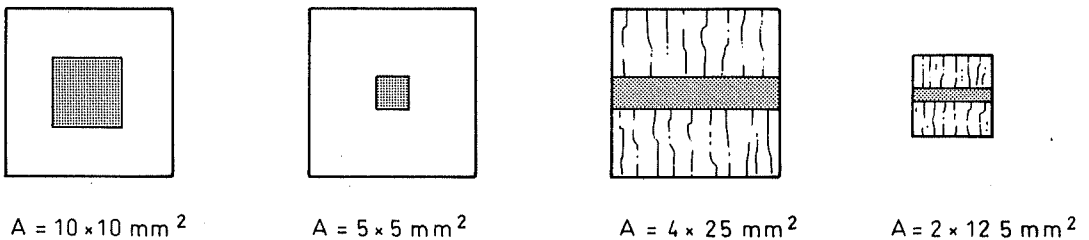
Figure 4.7: *Different specimen geometries of the small specimen tension test.*

Table 4.5: *Results from introductory tensile tests. Beech adherends bonded with resorcinol/phenol.*

Bond line geometry [mm^2]	Number of tests [stable/total]	σ_f [MPa]	G_f [kNm/m^2]	σ_f^2/G_f [GPa/m]
10·10	4/5	6.1 ± 0.6	0.23 ± 0.01	162
5·5	4/4	5.6 ± 0.5	0.20 ± 0.06	157
4·25	2/4	6.1 ± 0.9	0.21 ± 0.00	177
2·12.5	2/2	6.1 ± 0.4	0.20 ± 0.03	186

energy was recorded for those specimens. Mean values with standard deviation of the bond line parameters are given in Tab. 4.5.

Good correspondence was obtained. Disparities among the different geometries are small, and overall less than the corresponding standard deviations. Accordingly, the test method may be considered as well adapted, including uniform stress distribution of bond line stresses, and it is not possible to appoint one geometry as the most appropriate for the tensile test programme. Due to similarities to the shear specimen, the $4 \cdot 25$ mm^2 was chosen in the second test programme.

Two series, one with one-component polyurethane (Casco 1809) and one with two-component resorcinol/phenol (Casco 1703+2624), with 10 specimens each were tested. The bonds were 0.1 mm thick, cured for approximately two weeks at 20°C and 65% RH. The tests were run with a constant rate of deformation of 0.0625 mm/min. Estimated mean stress-widening curves of the two series are given in Fig. 4.8 and in normalized form in Fig. 4.9. The curves expose similar characteristic shapes as in shear but the magnitudes are smaller, especially for the polyurethane bonds. Mean values with standard deviations of the recorded bond properties are given in Tab. 4.6. The fracture was located into the bond line, being a mixture of adhesion failure with presence of wood fibres from both adherends and cohesion failure within the glue layer.

Corresponding values for wood are reported in the literature, e.g. [12, 40, 79]. For Scots pine, tensile strengths are registered in the range of 3-6 MPa and fracture energy values in the range of 300-500 Nm/m^2 with lower values for round annular rings and higher moisture content [12]. The figures given in [12] are overall higher than for the two other references. Regarding brittleness, the resorcinol/phenol to beech specimens expose a considerably more brittle behaviour than those of Scots
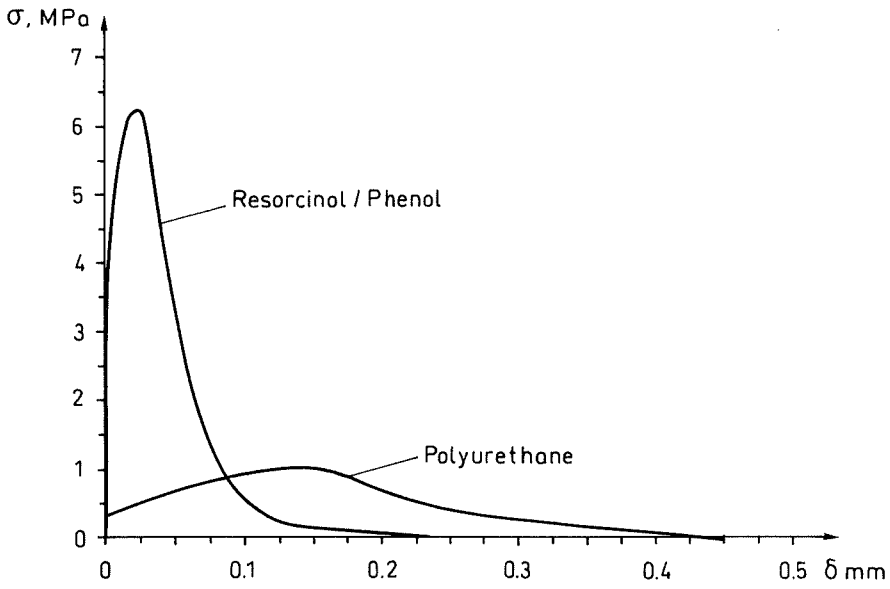
Figure 4.8: *Mean $\sigma - \delta_n$ curves of resorcinol/phenol and polyurethane bonds in tension.*
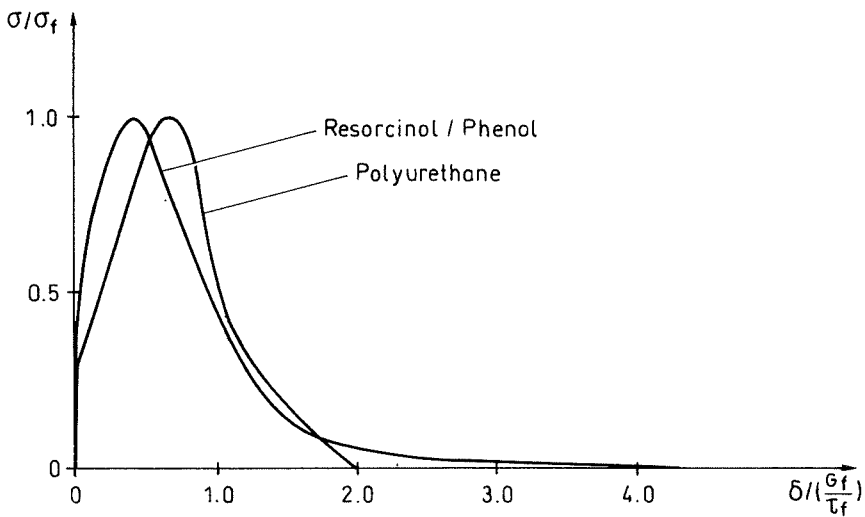
Figure 4.9: *Normalized mean $\sigma - \delta_n$ curves of resorcinol/phenol and polyurethane bonds in tension.*

Table 4.6: *Tension test results.*

Adhesive	Number of tests [stable/total]	σ_f [MPa]	G_f [kNm/m^2]	σ_f^2/G_f [GPa/m]
Resorcinol/phenol	8/10	6.4 ± 0.8	0.36 ± 0.06	114
Polyurethane	10/10	1.0 ± 0.5	0.23 ± 0.09	4

pine.

It is most probable that the properties of polyurethane are underestimated. The small bond size in combination with the Teflon film means that the boundary effects are too large and the clamping pressure is insufficient. This is also indicated by the deviation in the recorded values. The specimen with the highest figures exposed a strength value of 2.0 MPa and a fracture energy value of 0.45 kNm/m^2, which is twice that of the mean values. This was not further investigated in the present study.

There is a significant difference in recorded fracture energies of the resorcinol/phenol bonds in the two sets of test. There were, however, three main differences in the test situations. Different pots of glue of different ages were used, slightly different mixing procedures were employed, and furthermore the curing time was doubled.

4.2.3. Small mixed-mode results

The small specimen mixed-mode test series involved tests on resorcinol/phenol (Casco 1711+2620) bonds, PVAc (Casco 3304) bonds and some comparative tests on pure wood. The wood material used had a mean density of 570 kg/m^3, an average moisture content of 11 % and with distances between annual rings in the range of 1.1 to 1.3 mm. The specimens were stored in a constant climate of 20 °C and a relative humidity of 65 %. The PVAc specimens were cured for 15-17 days before testing; for the R/P specimens the curing times were in a wider span of approximately 1-3 weeks. The wood specimens and the adherends of the bonded specimens were made from sapwood of Scots pine (Pinus Sylvestris) with the grain direction in the shear direction and with a slope of the angular rings, θ_r, in the range of $30° - 45°$ to the normal direction, cf. Fig. 3.13. The bond lines were limited by means of 0.1 mm Teflon film.

The bonded specimens were tested at 7 different mixed-mode angles, while the wood specimens were tested at only 4 different directions in the $\delta_s - \delta_n$ field. The
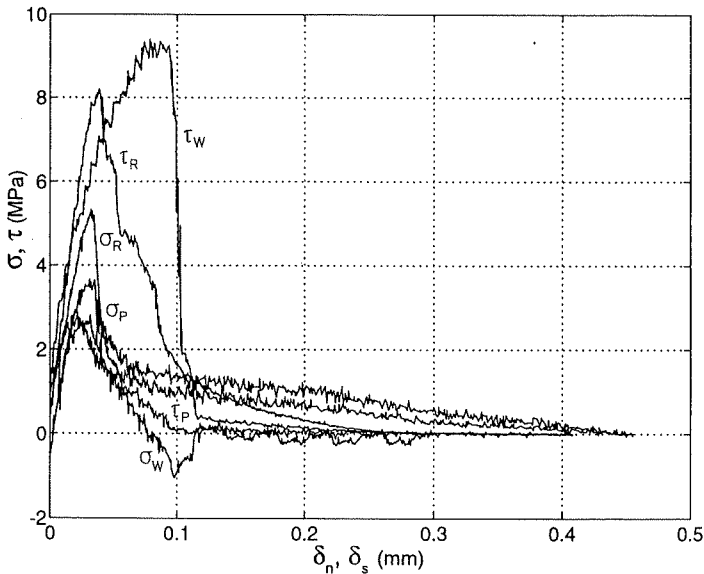
Figure 4.10: *Typical recorded stress-deformation curves for R/P (R), PVAc (P) and wood (W) at $\psi_g = 45°$.*

tests were run at a deformation rate of 0.03 mm/min in the dominant direction and adjusted in the inferior direction to correspond to the present mixed-mode angle. The testing machine, presented in Sec. 3.1.3, was in a development phase during the tests. A major problem during the tests was signal noise, which caused some problems in the evaluation, but more important, the fluctuating signal increased the frequency of unstable tests. Since the test series was completed the machine has been improved, and complementary tests showed considerably smoother curves and improved stability performance of the tests. In the evaluation the results may nevertheless be considered as significant, except for some of the PVAc results at large mixed-mode angles, i.e. at shear-dominated failure, which are rather rough estimates. However, the general tendency should not be questioned.

In Fig. 4.10 typical stress deformation curves are given for the mixe-mode angle $\psi_g = 45°$. ψ_g being the mixed-mode angle of the LVDT-transducers which controls the test, i.e. the mixed-mode angle of the steel grips close to the specimens. Characteristic fracture surfaces are given in Fig. 4.11. For R/P failure is mainly an adhesive debonding, involving the outer fibre layer of the adherends, while PVAc reveals a mixture of adhesive and cohesive failure. For the wood specimens the fracture surface often was rather rough, but still located along the symmetric axis of the specimen.

The recorded mean strengths and fracture energies for the mixed-mode angles
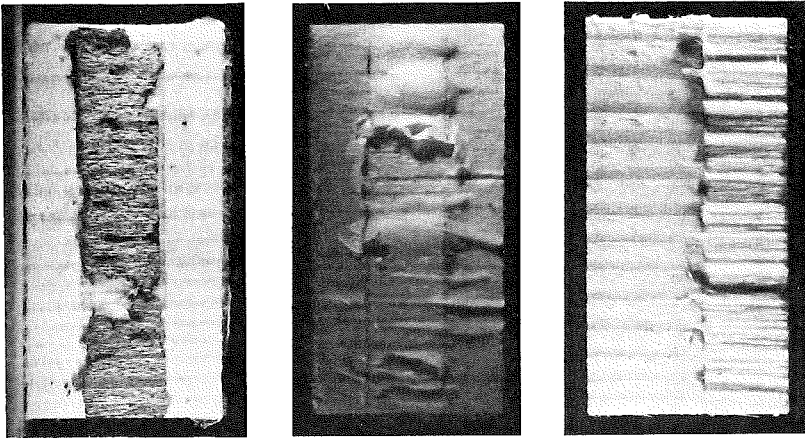
Figure 4.11: *Fracture surfaces of R/P, PVAc and wood specimens.*

ψ_g and ψ_b are given in Table 4.7. ψ_b is the estimated mixed-mode angle of the bond line corresponding to ψ in Sec. 2.4.3. This estimate is based on the experiments and on FE-analysis, further discussed in connection to Fig. 4.24. To obtain a more accurate value of ψ_b, optical equipment could be used, which was not applicable during the present test series. Standard deviations are given for R/P and wood, while for PVAc the rather rough estimates imply that standard deviations would have rather subjective interpretation.

The strength values given in Tab. 4.7 are the peak values during the tests. For the bonded specimens the peak values and, hence, also the softening occurred simultaneously in the two directions. For wood, however, the softening occurred at different times. This difference is illustrated in Figs. 4.12 and 4.13, in which typical recorded mean stresses versus time curves are plotted for R/P and wood.

From the recorded curves, force versus displacements of the grips, evaluated mean stress-deformation curves of the R/P and PVAc bond lines are established, given in Figs. 4.14-4.17. In the evaluation of stresses, the recorded load is divided by the bond area, $4 \cdot 20$ mm^2, and for the evaluation of the bond displacements the stiffness outside of the bond lines is estimated to be 2.0 MN/m in shear and 1.2 MN/m in tension. These stiffness numbers were obtained by loading/unloading tests of solid wood specimens in the similar manner as performed for the uniaxial tests, cf. Fig. 3.11. The difference of the loading and the unloading curve was considered small in comparison to the signal deviations and, hence, no fracture energy reduction was made due to plastic dissipation of the wood material.

From the recorded curves and the evaluated bond line properties, there is a clear difference between the PVAc and the resorcinol/phenol bonds. The R/P bonds exposed the most brittle performance, with the largest number of unstable tests. For predominating normal directions the curves of the three materials are quite similar, but as the influence of the shear component increases, the PVAc curves

Table 4.7: *Mixed-mode material test results. Strength and fracture energies are given for different mixed-mode angles, ψ_b, being the initial bond line mixed-mode angle which will converge towards the global angle, ψ_g, during the test, as described in Fig. 4.24.*

Bond	Number of tests (stab/tot)	ψ_g	ψ_b	$\tau_{f,a}$ [MPa]	$\sigma_{f,a}$ [MPa]	$G_{fs,a}$ [Nm/m^2]	$G_{fn,a}$ [Nm/m^2]	$G_{f,a}$ [Nm/m^2]
R/P	8/11	0	0	0	4.9±0.9	0	310±100	310±100
	5/5	6	28	1.4±0.5	4.9±1.1	12±4	380±60	400±60
	5/7	23	70	3.7±0.7	5.4±0.6	110±16	190±30	310±40
	6/17	45	79	6.3±1.7	4.4±1.2	550±70	280±170	830±210
	5/14	63	85	10.8±1.3	2.8±0.6	660±80	50±20	710±60
	4/7	84	89	12.8±1.1	1.1±0.9	1250±280	-20±10	1230±260
	2/5	90	90	12.9±0.7	0.6±0.5	1590±530	0	1590±530
PVAc	5/5	0	0	0	4.6	0	820	820
	2/3	6	28	0.9	3.9	10	570	580
	5/5	23	70	1.9	3.5	100	440	540
	3/4	45	79	2.5	3.8	320	490	810
	5/5	63	85	2.8	3.0	600	310	910
	5/5	84	89	4.2	2.4	~1800	70	~1870
	5/5	90	90	5.1	-	~3000	10	~3000
Wood	6/6	0	0	0.9±0.3	4.8±0.5	0	475±65	475±65
	8/9	45	79	8.1±0.7	3.3±0.5	481±81	146±36	627±99
	2/2	51	82	9.4±0.6	2.7±0.7	552±36	75±97	627±61
	4/4	90	90	10.9±0.5	0.2±0.1	1120±86	0	1120±86
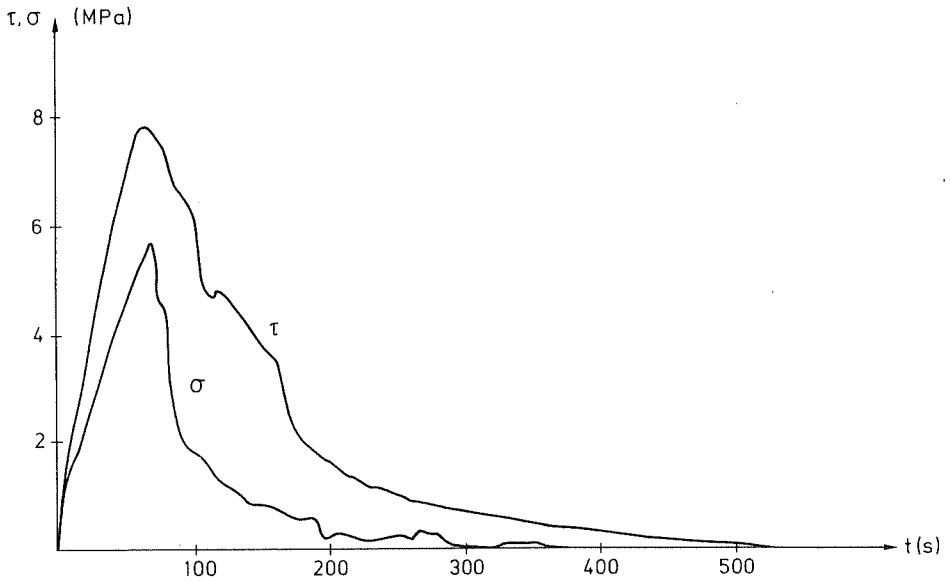
Figure 4.12: *Typical stress-time curves for R/P at $\psi_g = 45°$.*
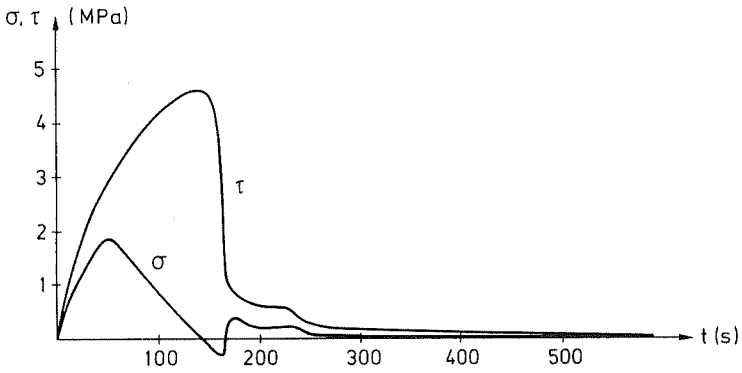
Figure 4.13: *Typical stress-time curves for wood at $\psi_g = 45°$.*
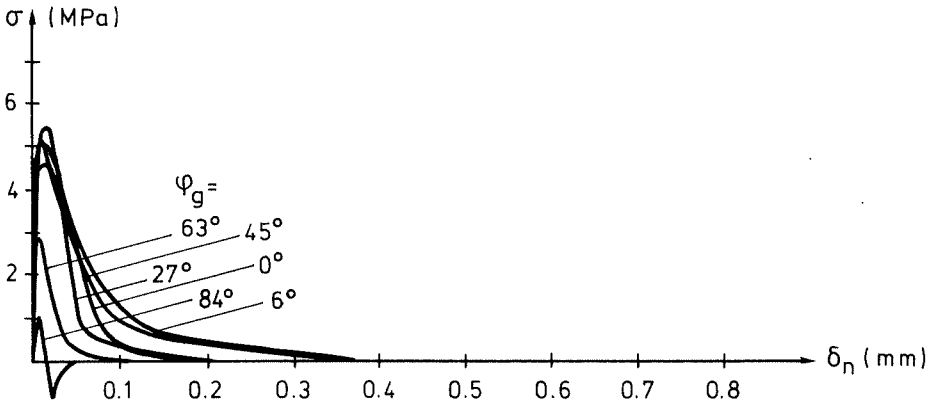
Figure 4.14: *Mean normal stress-deformation curves for resorcinol/phenol bonds at different mixed-mode angles, ψ_g.*
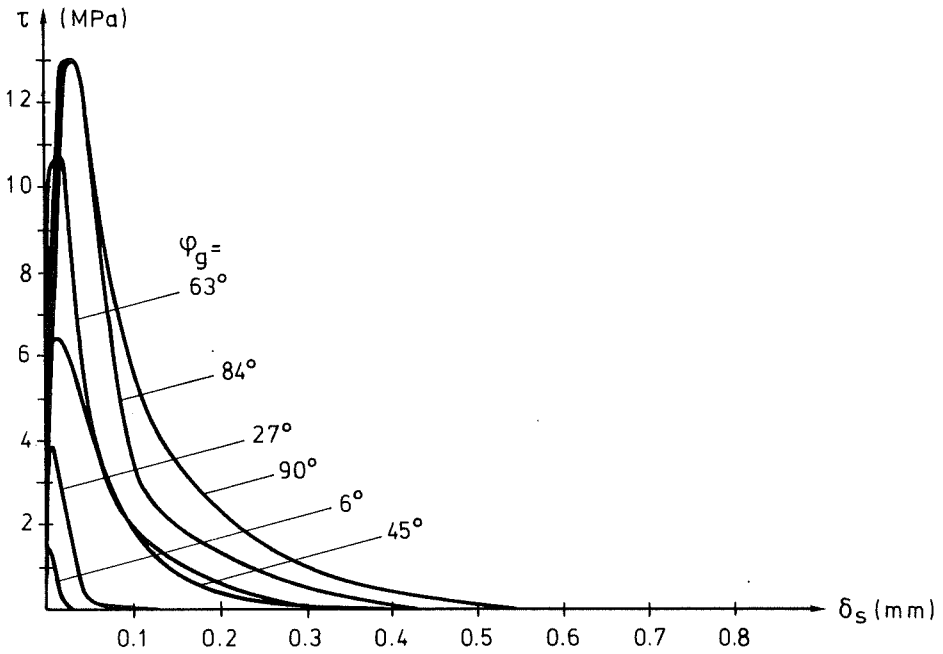
Figure 4.15: *Mean shear stress-deformation curves for resorcinol/phenol bonds at different mixed-mode angles, ψ_g.*
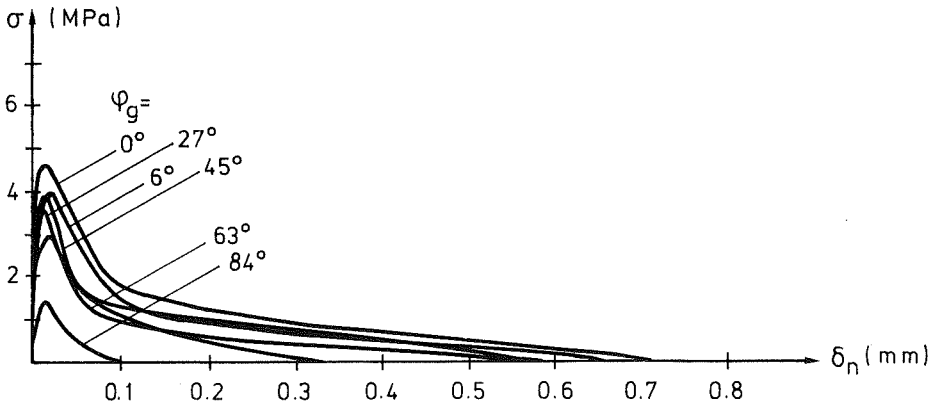
Figure 4.16: *Mean normal stress-deformation curves for PVAc bonds at different mixed-mode angles, ψ_g.*
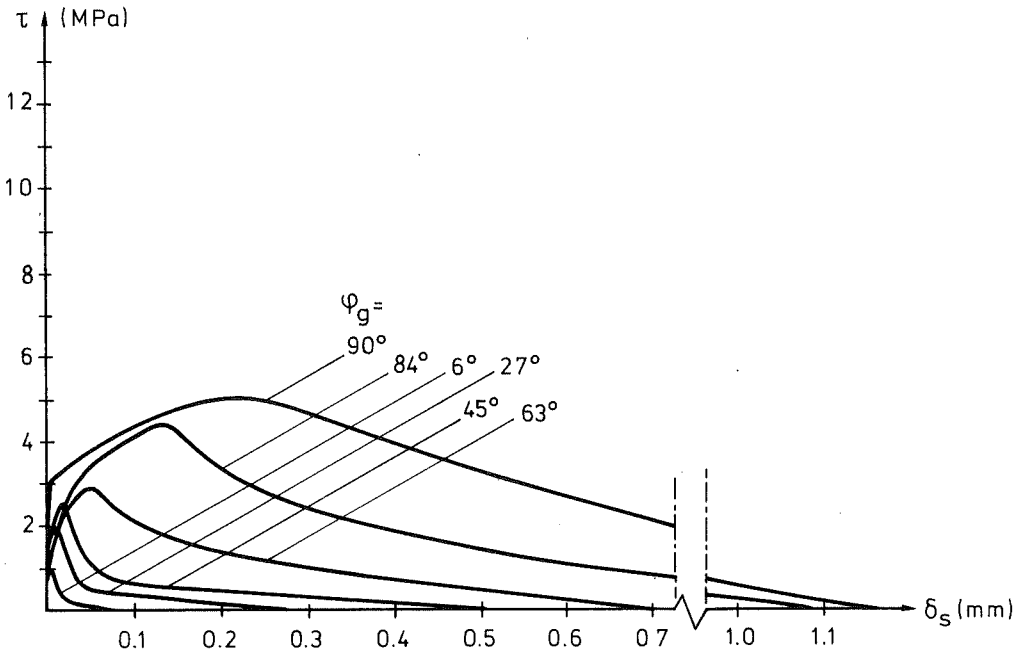
Figure 4.17: *Mean shear stress-deformation curves for PVAc bonds at different mixed-mode angles, ψ_g.*
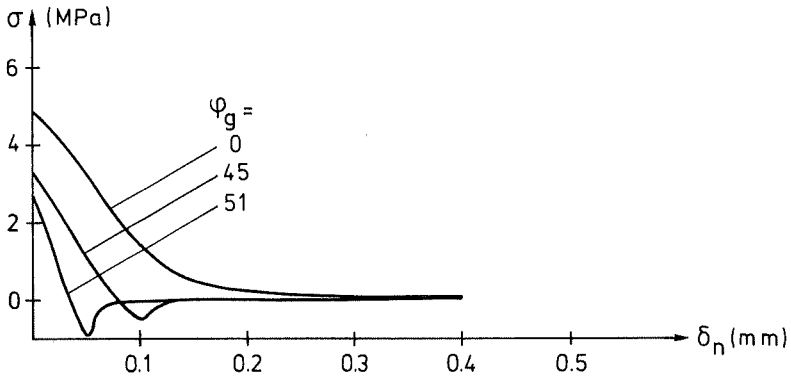
Figure 4.18: *Mean softening normal stress-deformation curves for wood bonds at different mixed-mode angles, ψ_g.*
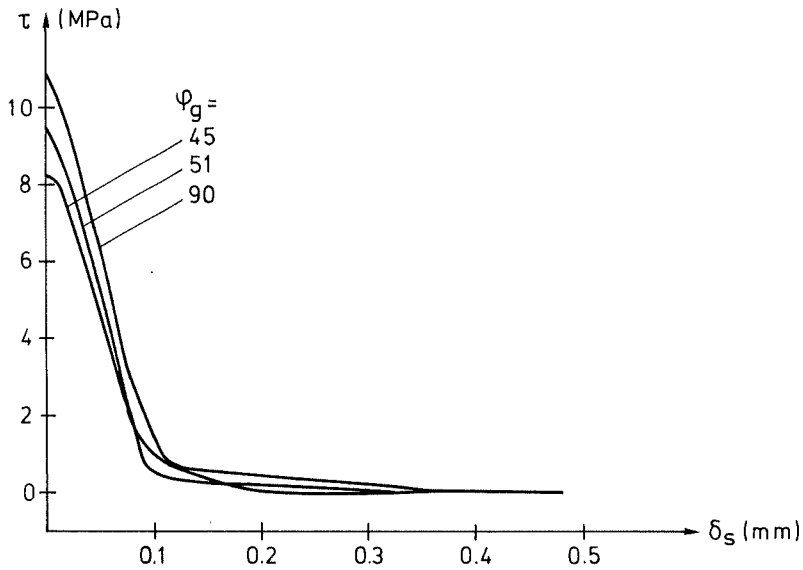
Figure 4.19: *Mean softening shear stress-deformation curves for wood bonds at different mixed-mode angles, ψ_g.*

become more extended as the fracture energy increases comparatively much at a rather low local shear strength.

The wood curves, given in Figs. 4.18 and 4.19 are evaluated according to the fictitious crack model [44]. Hence, the deformation indicated in these figures is the tensile opening and shear slide, respectively, of the localized fracture process region, assumed to develop at peak stress due to strain instability. The performance in tension and shear is evaluated separately. In the evaluation, the unloading of the material outside of the localized fracture zone is assumed to take place according to the initial elastic stiffness of the specimen. Hence, dissipation in the wood material due to plastic hardening is reduced for, and the fracture energy is the energy consumed in the softening region.

As stated in the uniaxial tests, the R/P bonds expose similar behaviour as pure wood, as the fracture process of the strong and brittle R/P is influenced by the adjacent wood material. The mixed-mode tests support this assumption. In Figs. 4.20-4.22 the recorded local strengths are plotted in a $\sigma - \tau$ diagram and compared to the common failure criterion

$$\left(\frac{\sigma_{f,a}}{\sigma_f}\right)^m + \left(\frac{\tau_{f,a}}{\tau_f}\right)^n = 1.0 \qquad (4.1)$$

where $\sigma_{f,a}$ and $\tau_{f,a}$ are normal and shear strength for a present mixed-modity, and m and n are the chosen integers that best correspond to the respective curves. For R/P and wood m and n are chosen to be 2, while for PVAc the best fit was found for $m = 2$ and $n = 1$.

In Fig. 4.23 the total fracture energy of R/P and PVAc is plotted against the fracture energy based mixed-mode angle ψ_G, defined in Eq. (2.53), and compared to calculated curves based on the mixed-mode model. For R/P, G_f seems to be quite independent of mixed-mode angle, except for at large ψ_G, where a large increase is observed. For PVAc the curve is more rounded with a tendency of a minimum point in the mixed-mode region. While R/P exhibits the best fit to the mixed-mode model with $m = n = 2$, PVAc reveals a better fit for $m = n = 1$. Furthermore, R/P corresponds well to the curve in Fig. 2.7b, PVAc corresponds more to a mixture of curve a and b. PVAc is a tough material, but in a bond line it is restrained by the adherends, which affect the size and shape of the fracture zone.

To verify the mixed-mode model, presented in Sec. 2.4.3 by means of the mixed-mode material test results is complicated. The deformation control in the tests is related to displacements outside of the specimen. Since no measuring technique to record the actual bond displacements was available during the tests, the transformations from global to bond displacements involves approximations. Furthermore, in the beginning of the test the bond line will expose a comparatively large stiffness, but as the test proceeds and the bond line enters the softening region, the incremental bond line stiffness will become negative. This implies that for a prescribed constant ψ_g, the bond line angle ψ_b will change during the test. For the present specimen, ψ_b will in the beginning be considerably larger than ψ_g. In Tab. 4.7 the
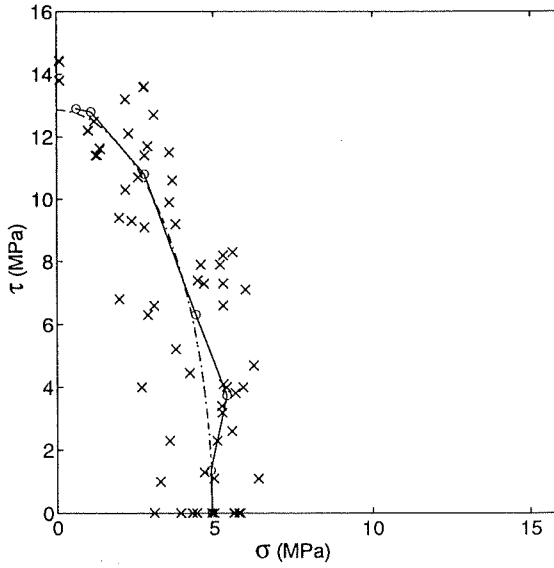
Figure 4.20: *Recorded mixed-mode strength of resorcinol/phenol bonds, compared to Eq. (4.1) with m=n=2. ◦ denotes the mean for each tested angle ψ_g.*
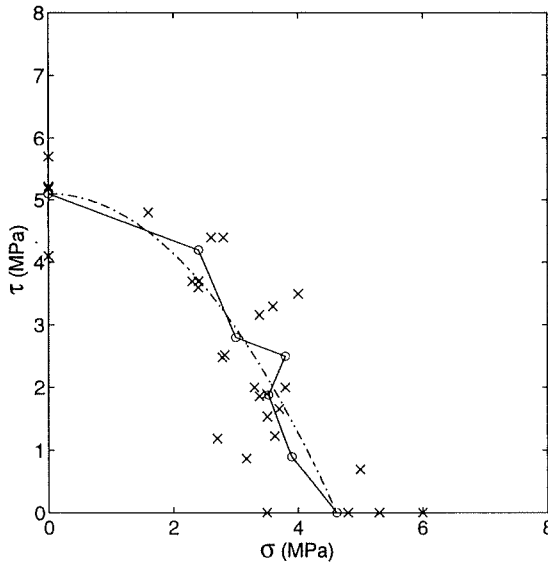
Figure 4.21: *Recorded mixed-mode strength of PVAc bonds, compared to Eq. (4.1) with m=2, n=1. ◦ denotes the mean for each tested angle ψ_g.*
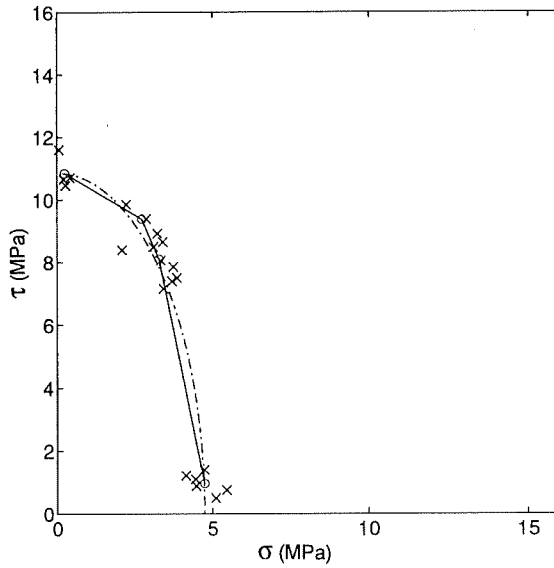
Figure 4.22: *Recorded mixed-mode strength of wood, compared to Eq. (4.1) with m=n=2. ○ denotes the mean for each tested angle ψ_g.*
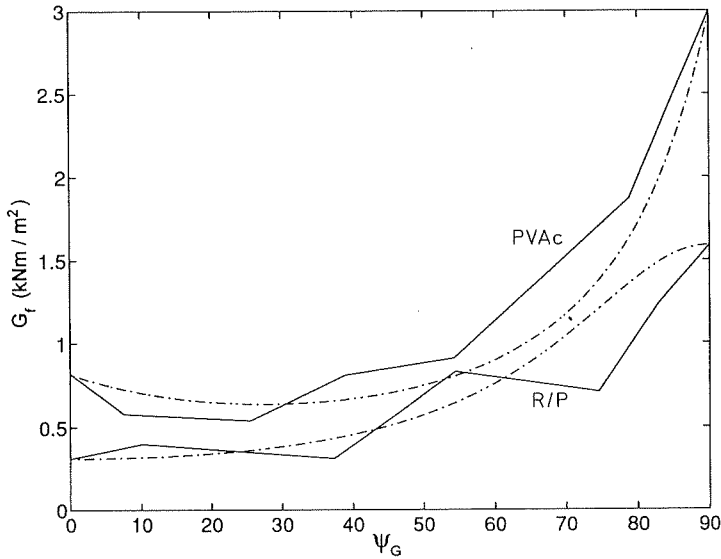
Figure 4.23: *Experimental total fracture energy versus ψ_G for resorcinol/phenol and PVAc compared to calculated curves with the mixed-mode model with m=n=2 for R/P and m=n=1 for PVAc.*
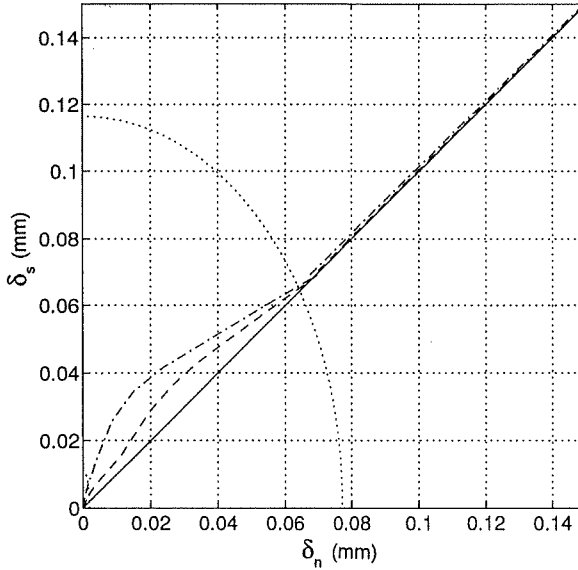
Figure 4.24: *Bond line displacement paths for the small mixed-mode specimen.* ψ_g(-), ψ_b-bond corner(- -), ψ_b-means(-.). *The dotted lines denote the breaking points of the chosen tri-linear model.*

estimated initial value of ψ_b is given. However, at the end of the test the bond line stiffness approaches zero and ψ_b will converge towards ψ_g. In Fig. 4.24, the outcome from a FE-analysis with the mixed-mode model is given for $\psi_g = 45°$. In the analysis the stiffness parameters are chosen so that the calculated global stiffness of the specimen corresponds to those recorded experimentally. The path of the bond line displacements will be correlated to the chosen stiffness parameters.

Even though the specimen is very short there will not be a completely uniform stress and deformation state along the bond line. This non-uniformity does not significantly affect the global load-displacement curve during the test. Analysis of the specimen with the chosen material model gives a global response corresponding to the input model. However, the magnitude of the bond line angle, ψ_b, will be different if the displacements are chosen to be means along the bond line or as being those in the bond line corner. ψ_b for these two choices is given in Fig. 4.24.

Altogether, a direct evaluation of the mixed-mode model from the recorded results is connected with rough estimations. Such evaluation will in the future be improved with measuring technique facilitating recordings of displacements in or very close to the bond line. Optical instruments with such abilities are under development for use in e.g. the biaxial testing machine. The indirect evaluation in Figs. 4.20-4.23 reveals a reasonable correspondence between test results and the model.

4.3. Verification and Crack Propagation Results

In the large specimen test programme, the main objective has been to verify the material test recordings, the theory and the models of analysis. A crack propagation specimen is here a rather large specimen with a non-uniform stress distribution for which the load carrying capacity is governed only by fracture mechanics crack propagation properties such as G_c, and not by local strength. The scope of the programme is limited, but sufficiently large to draw several conclusions about the questions at issue.

4.3.1. Large shear specimen results

The specimen used in the large shear specimen test is given in Fig. 3.14. The test series involved two different adhesives, one-component polyurethane (Casco 1809) and two-component resorcinol/phenol (Casco 1703+2624), tested at three different bond lengths, 0.025 m, 0.1 m and 0.4 m. For each combination two specimens were tested. The specimens were cured for approximately 10 days, the bond line thickness was 0.1 mm and the tests were run at a constant actuator rate of 0.0625 mm/min.

Specimen strength can be calculated by Eq. (2.24) choosing γ to be 1.0 or preferably by taking bending effect into account as 0.5, which was suggested in Eq. (3.1). These equations are based on the simplified constitutive relations given in Fig. 4.25a, where the peak shear stress is τ_f and the area below the curve equals the fracture energy, G_f. The "fictitious" shear modulus obtained from this assumption will, due to the apparent nonlinear properties of bond lines, be more appropriate for many applications in strength analysis than some "true" elastic modulus. The analysis will correspond to a regular maximum stress analysis for which the shear modulus is modified with regards to fracture energy. For specimens with sufficiently large brittleness ratios the load carrying capacity will be independent of the shape of the stress-deformation curve and, hence, with this simplified model a material point is expected to fail when the stress reaches its maximum value, τ_f.

The load-slip response of the specimen can analytically be calculated by combining Eqs. (3.3) and (3.4) for increasing crack length a. A more precise description can be found in [98]. The material properties employed in the analysis were for wood: $E = 13$ GPa, for resorcinol/phenol bonds: $\tau_f = 8.5$ MPa, $G_f = 0.71$ kNm/m^2 and for the polyurethane bonds: $\tau_f = 3.2$ MPa, $G_f = 0.77$ kNm/m^2.

To verify the analytical model, a finite element analysis was performed for the resorcinol/phenol specimen. The software used was a modified version of GENFEM-S [63] and the material model was in this case more sophisticated, given in Fig. 4.25b. The properties are of the same magnitude as those of Fig. 4.25a, but the shape of the material curve corresponds better to the recorded relations. However, for sufficiently large joints the curve shape will not influence the load carrying capacity of the specimen and, hence, for the 400 mm specimen the two methods of analysis should be expected to coincide. For the largest specimen tested, calculated response is given
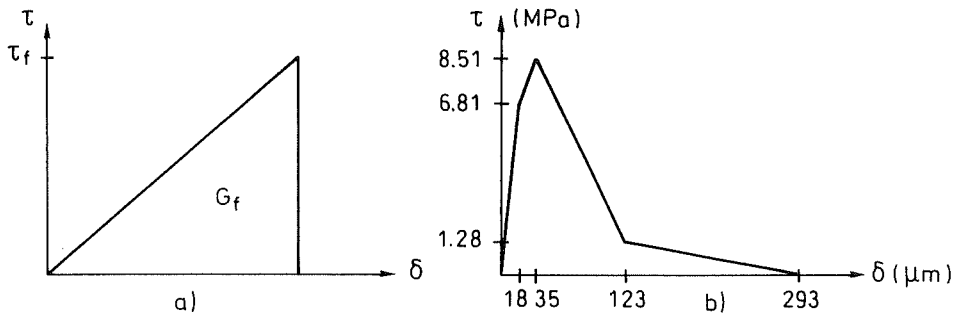
Figure 4.25: *Constitutive relations of bond lines used a) in analytic analysis b) resorcinol/phenol in FE-analysis.*

in Fig. 4.26. Using standard so-called Volkersen theory, i.e. $\gamma = 1$ in Eq. (3.1), the expected response will differ considerably in comparison to beam theory choosing $\gamma = 0.5$, i.e. including bending of the adherends. The beam theory analysis and the finite element analysis do, however, reveal similar responses. Accordingly, beam theory is expected to be adequate for analysis of the large shear specimen.

The three different lengths bonded with resorcinol/phenol were calculated with finite elements and it is shown that only the longest, $\ell = 400$ mm, will fully reach the plateau level of constant load at fracture propagation. The result is shown in Fig. 4.27. For polyurethane the corresponding curves were calculated by means of beam theory, cf. Fig. 4.28. The polyurethane specimens are considerably more flexible than the corresponding resorcinol/phenol specimens and, in addition, the difference in initial stiffness is more pronounced. Due to the simplified material model in Fig. 4.25a the fictitious initial shear modulus is so low that it will considerably influence the global stiffness of the shorter specimens. However, the maximum load capacity is influenced only to a minor extent.

Recorded and calculated load carrying capacities of the specimens are given in Tab. 4.8. For the longest resorcinol/phenol specimen, the strength value corresponds to the mean of the plateau load. The calculated values for resorcinol/phenol are in good agreement with the recorded figures. In a later test series [29] the 400 mm specimen were used in three tests of another resorcinol/phenol adhesive (Casco 1711+2620) for which similar results were obtained, i.e. $P_{max} = 3800$ N implying that $G_f = 815$ Nm/m^2. For polyurethane the correspondence is, however, rather poor, with considerably higher properties for the large specimen. This can most likely be explained by the difference in curing conditions for the small and the large specimen, respectively.

Figs. 4.29 - 4.31 show the calculated and recorded load-slip responses of resorcinol/phenol specimens at the three lengths tested. For the shortest specimen, $\ell = 25$ mm, the calculated response is in good agreement to the recorded response. The
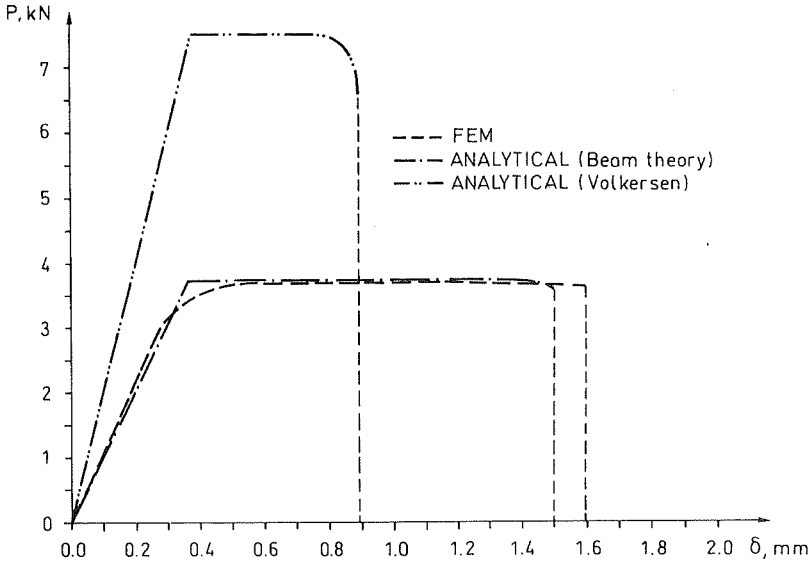
Figure 4.26: *Comparison of different methods of analysis applied on the large shear specimen with $\ell = 400$ mm and bonded with resorcinol/phenol.*

Table 4.8: *Calculated and experimental failure load of the large shear specimen. The material properties used for wood are: $E = 13$ GPa, for resorcinol/phenol : $\tau_f = 8.5$ MPa, $G_f = 0.71$ kNm/m^2 and for the polyurethane bonds: $\tau_f = 3.2$ MPa, $G_f = 0.77$ kNm/m^2.*

ℓ [mm]	Resorcinol/phenol			Polyurethane	
	P_{anal} [kN]	P_{FEM} [kN]	P_{test} [kN]	P_{anal} [kN]	P_{test} [kN]
25	1.93	1.97	1.60	0.81	0.34
			1.70		0.40
100	3.66	3.54	2.55	2.68	4.25
			3.05		4.65
400	3.74	3.68	3.80	3.88	8.35
			4.15		8.70
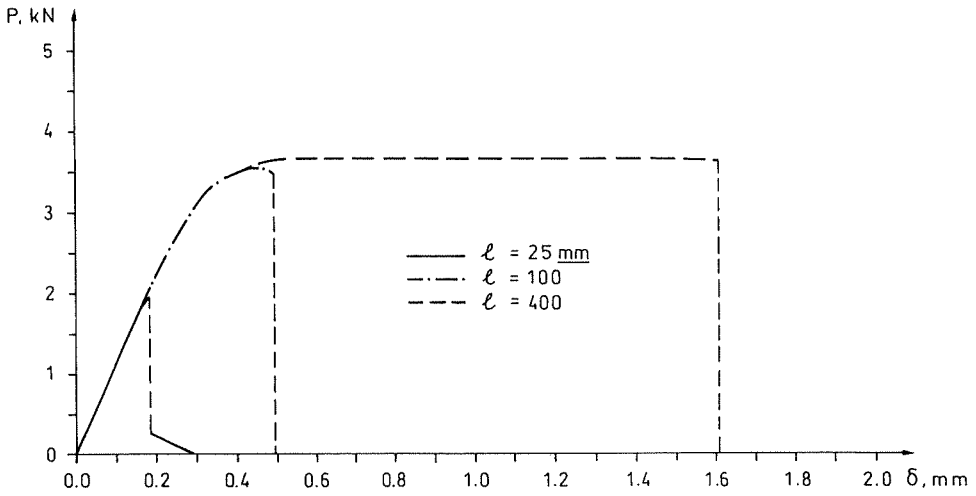
Figure 4.27: *Load-displacement response of the large shear specimen at three different lengths bonded with resorcinol/phenol. Calculated with finite elements.*
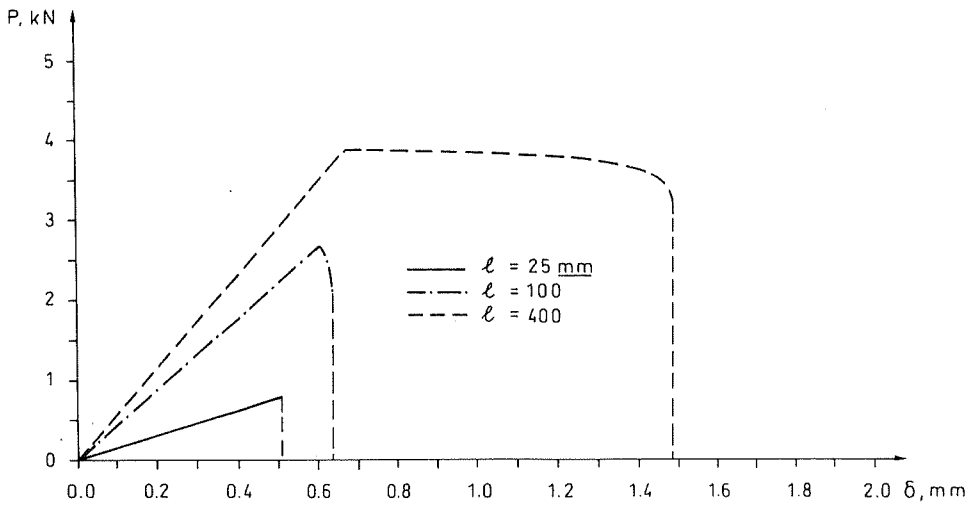
Figure 4.28: *Load-displacement response of the large shear specimen at three different lengths bonded with polyurethane. Calculated analytically with beam theory.*
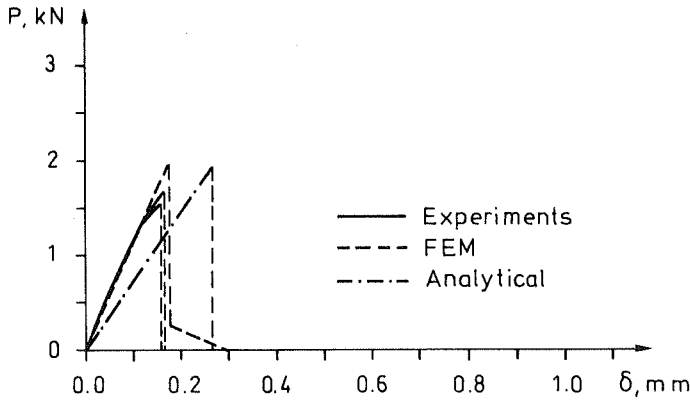
Figure 4.29: *Experimental and calculated force-slip response of the large shear specimen bonded with resorcinol/phenol.* $\ell = 25$ mm.

force-slip relation is approximately linear up to peak load, followed by an abrupt failure. Calculated peak load is somewhat overestimated, possibly due to boundary effects, and due to the simplified material curve the analytical solution tends to underestimate specimen stiffness.

For the specimen of intermediate length, $\ell = 100$ mm, in Fig. 4.30, the conformity is less good. The lower strength specimen exhibits a response similar to that calculated except for a missing top, while the second specimen reveals a more ductile behaviour than expected. The result is most probably due to instabilities during the test.

The conformity of the longest specimen, $\ell = 400$ mm, is good, cf. Fig 4.31. The expected plateau at peak load is recorded in the tests with an average magnitude only slightly exceeding those obtained in the calculations. In addition, the deviation in calculated and recorded deformation at failure is small. At the plateau, bond failure will propagate without any additional force being required. From Eq. (3.3) it is concluded that the only material properties influencing the magnitude of the force plateau are adherend stiffness and bond line fracture energy. Accordingly, if E is known fracture energy may be evaluated as

$$G_f = \frac{4}{E} \frac{P_{ave}^2}{b'bt} \tag{4.2}$$

where P_{ave} is the average peak force level at the plateau, b' and b are the width of the adherends and the bond line, respectively, and t is the adherend thickness. G_f is a function of P_{ave} squared and, hence, the evaluation of G_f is sensitive to error estimates of the applied force. However, the total load-deflection curve should be recorded and, hence, P_{ave} can be evaluated as an average value of a long bond line and it may be expected to form an adequate mean. The deviation from the mean

Figure 4.30: *Experimental and calculated force-slip response of the large shear specimen bonded with resorcinol/phenol. $\ell = 100$ mm.*

Figure 4.31: *Experimental and calculated force-slip response of the large shear specimen bonded with resorcinol/phenol. $\ell = 400$ mm.*

plateau level may be interpreted as deviations of $\sqrt{EG_f}$. Accordingly, the large shear specimen may supersede a large number of material tests in determination of fracture energy.

The deviation in the plateau force does not, however, reflect the local variation of $\sqrt{EG_f}$. It may be expressed as a smooth mean value, representing the fracture energy and adherend stiffness over the entire active fracture region which is propagating along the bond line during increased deformation. The length of the fracture region, ℓ_{fr}, is proportional to the material brittleness ratio of the specimen. *Gustafsson* [38] gives an expression for the size of the fracture zone in Volkersen analysis. For the present large shear specimen this will be adjusted to

$$\ell_{fr} \approx 1.5\sqrt{t\frac{b'}{b}\frac{E}{4}\frac{G_f}{\tau_f^2}} \qquad (4.3)$$

The ratio b'/b is required to account for the limited bond line, and the reduction of E by a factor of 4 is to compensate for adherend bending. The factor 1.5 is a qualified guess; an accurate value should be in the range of 1.0 to 2.0. In accordance to the material tests, ℓ_{fr} should be in the range of 60 mm for resorcinol/phenol and about three times as large for the polyurethane specimen. Finite element analysis including a "true" material curve will give a more exact value of ℓ_{fr}.

The corresponding calculated and recorded curves for polyurethane for the bond lengths $\ell = 100$ mm and $\ell = 400$ mm are given in Figs. 4.32 and 4.33. No tests were made on 25 mm polyurethane, due to handling problems. There is a bad correspondence between the large specimen results and the small specimen test results. The magnitude of the polyurethane properties is considerably larger for the large specimen, mainly due to dissimilar curing conditions for the two specimens. The sensitivity to curing conditions for polyurethane was discussed in Sec. 4.2.1. From Tab. 4.8, the specimen load carrying capacities are underestimated for the two largest specimens, while for the 25 mm specimen it is overestimated. Assuming the strength of the 400 mm specimen to be governed only by fracture energy, it is implied that G_f should be 3.7 kNm/m^2, to be compared with the initial value of approximately one fifth, given in Tab. 4.1. This new value substituted in Eq. (3.1) means that the local bond strength should adopt a value of 4.9 MPa, about 50 % higher. These values yield a bond line brittleness ratio of approximately 6.5 GPa/m, which is about half the size of the material tests.

These new material properties were employed in the finite element analysis. In addition two different material curves were used, given in Fig. 4.34. The two models are given identical fracture energies but different strengths and curve shapes. The analysis confirms the observation from the one-dimensional theory that for long joints G_f will predominate over τ_f as the governing bond line property. The difference in local bond strength has some influence on the 100 mm specimen and it is notable that a rather small difference in material curve shape yields two principally
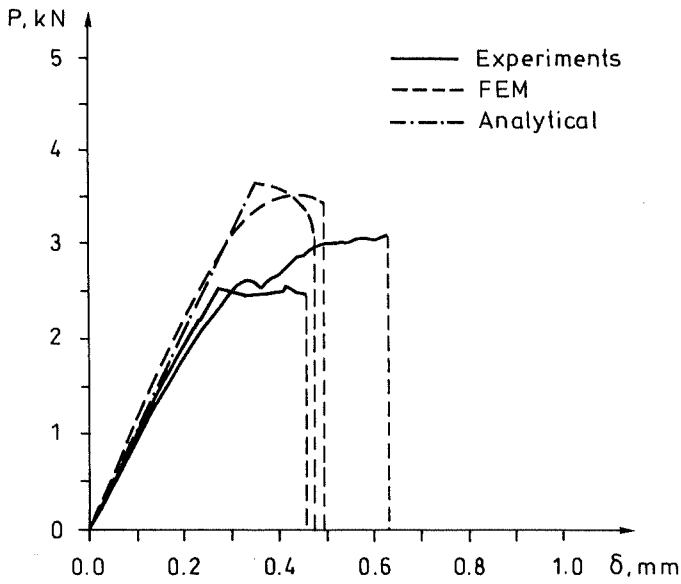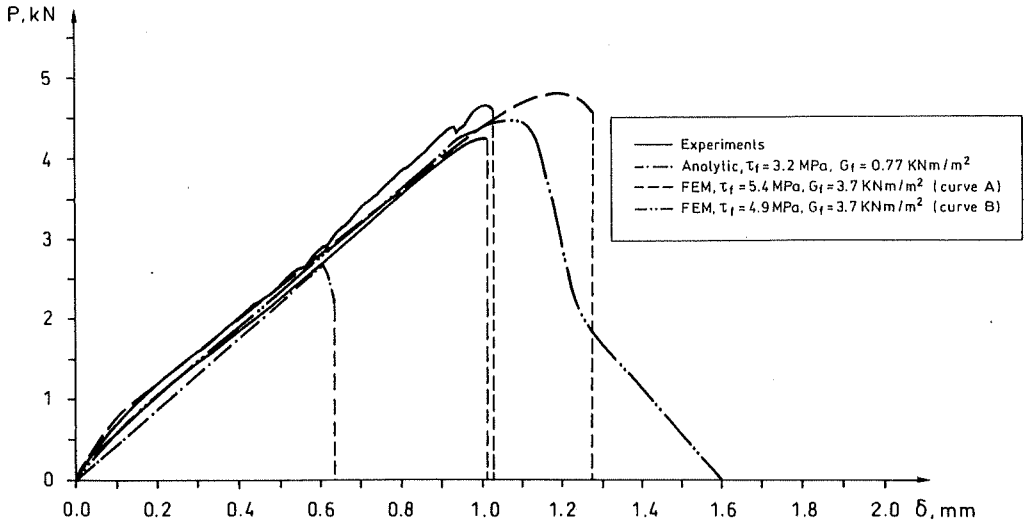
Figure 4.32: *Experimental and calculated force-slip response of the large shear specimen bonded with polyurethane.* $\ell = 100$ *mm.*
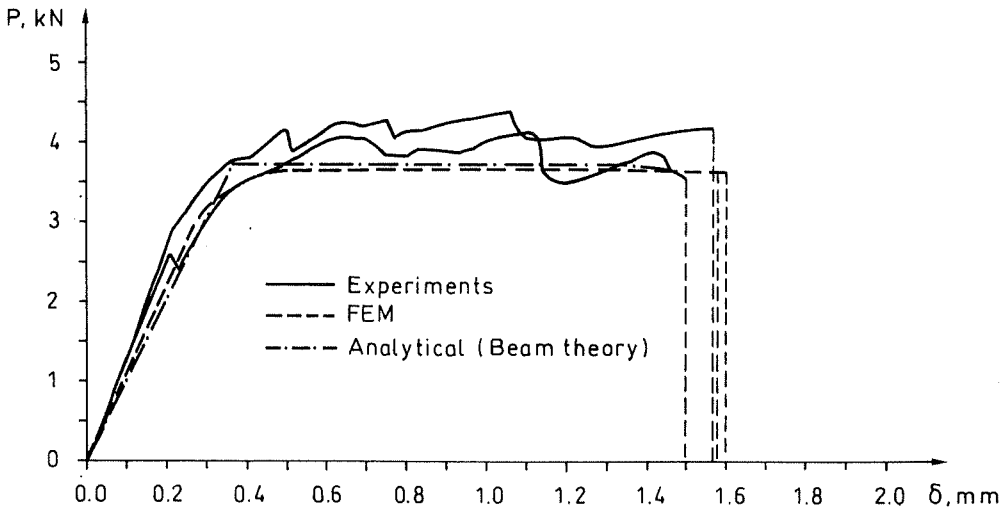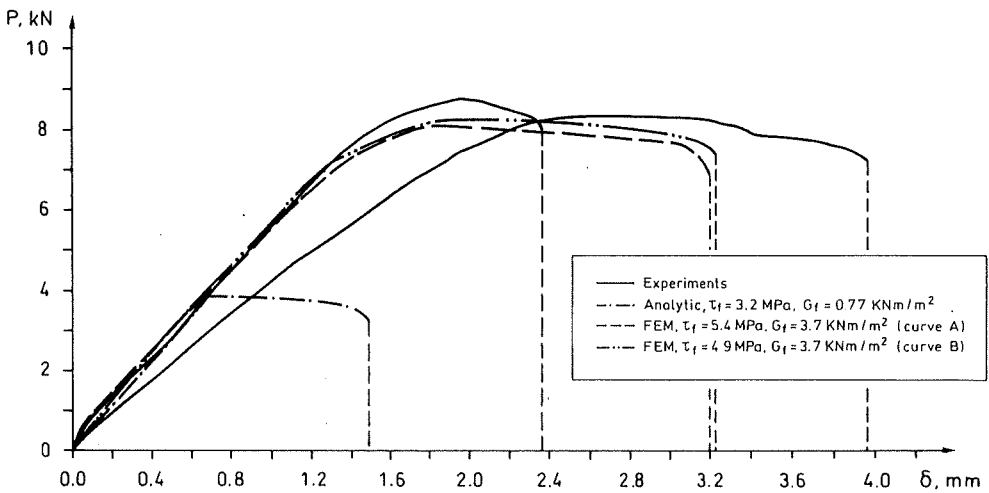

Figure 4.33: *Experimental and calculated force-slip response of the large shear specimen bonded with polyurethane.* $\ell = 400$ *mm.*
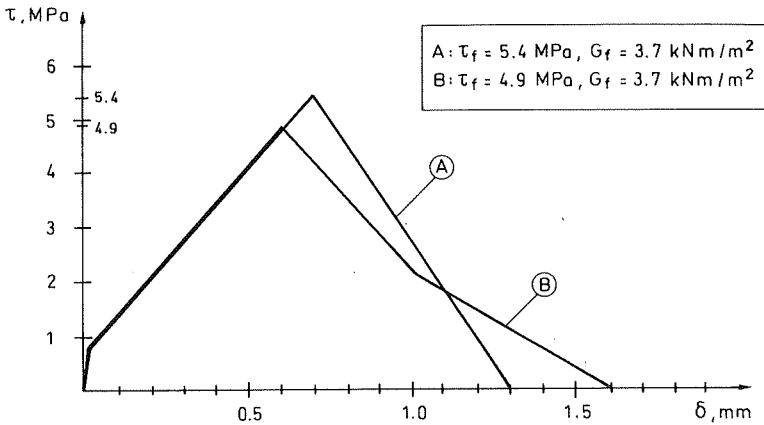
Figure 4.34: *Modified $\tau - \delta_s$ curves of polyurethane in accordance with large shear specimen results.*

different fracture characteristics of the 100 mm specimen, from brittle to stable performance.

4.3.2. Large tension specimen (DCB) results

In Sec. 3.3.2 some doubts were raised concerning the adaptability of the DCB specimen to tests of brittle bond lines. A test series was performed to experimentally evaluate the test method. Six different types of two-component adhesives were used and a study was performed where the mechanical bonding was improved by means of stoppers of adhesive material. The latter tests are presented in [29] together with all recorded curves. Of the recorded force-deflection curves, only a few reveal a shape similar to those expected from theory, which to a large extent can be explained by the occurrence of wood failure. However, by means of different methods of evaluation it is possible to quantitatively distinguish the adhesives.

The bond thickness of the specimens were 0.1 mm limited by a teflon film, and the specimens were cured for between 7 and 10 days. The E-modulus of the adherend material was from separate tests found to be 12 GPa as a mean.

In Tab. 4.9 evaluated fracture energy, G_f, and two values of the energy release rate G_c, are given. These two parameters should be of equal magnitude for the present specimen, but the difference is demonstrably large for most of the adhesives. G_f is evaluated as the area below the recorded load-displacement curve divided by the bond area, in accordance with Eq. (3.13), G_c^P, is obtained by means of linear elastic fracture mechanics in Eq. (3.9) and G_c^{fit} is an attempt to fit the recorded curves to theoretical curves also derived from Eq. (3.9).

Neither G_f nor the two values of G_c are correctly determined. G_c^P is determined directly from the square of the peak load, P_c^2, and as the theoretically expected sharp
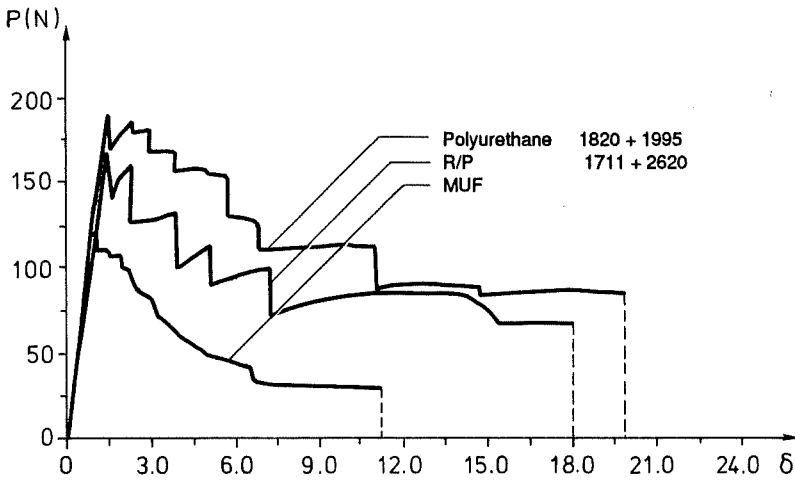
Figure 4.35: *Experimental force-displacement response of the large tension specimen, the adhesive codes are those given by Casco.*
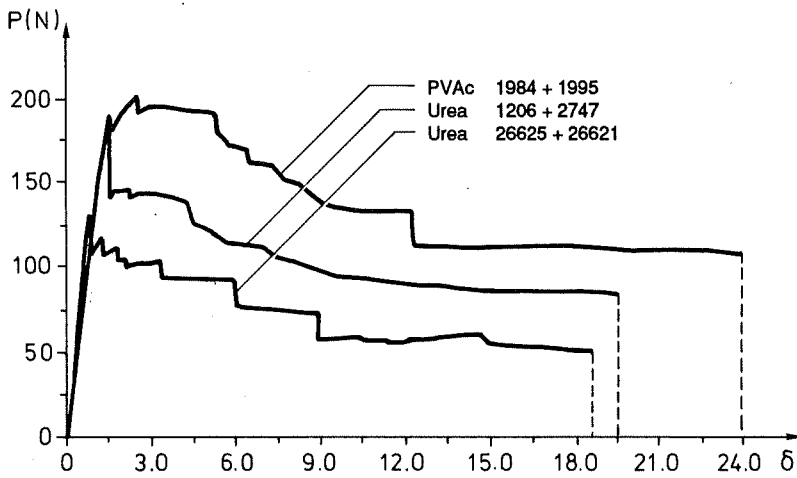
Figure 4.36: *Experimental force-displacement response of the large tension specimen, the adhesive codes are those given by Casco.*

Table 4.9: *Evaluated fracture energy, G_f, and energy release rate G_c, from DCB-tests.*
$E_w = 11800$ *MPa.*

Adhesive	Code	P_c [N]	G_f [Nm/m^2]	G_c^P [Nm/m^2]	G_c^{fit} [Nm/m^2]
PU	1820	189	530	290	700
R/P	1711	167	410	226	550
MUF	-	124	140	125	180
PVAc	1984	189	670	290	1000
Urea	1206	180	410	263	500
Urea	26625	132	310	141	320

top is not recorded, G_c will be underestimated. G_f is probably better approximated, but as the $P - \delta$ curve should theoretically reverse at the end of the test, it fails abruptly before it reaches the zero level. Accordingly, the area below the curve and, hence, also G_f should be expected to be overestimated. Furthermore, several of the specimens exposed a rather deep wood failure, yielding larger fracture areas, which would imply that the fracture energy is further overestimated. The evaluation of G_c^{fit} is also coarse, and due to partial wood failure different parts of the curves fit to different theoretical curves. The MUF specimens expose the best correspondence to theory, which is also reflected by a low G_f/G_c ratio. The failure was a typical bond failure and, hence, both G_f and G_c^P may be somewhat underestimated.

4.3.3. Mixed-mode bending specimen results

An experimental evaluation of the mixed-mode bending, MMB, specimen was performed. A total of 12 specimens of solid wood bonded with resorcinol/phenol (Casco 1711+2620) was tested with various amounts of mode-mixity. In addition, five composite aluminium/wood specimens were tested with an eccentricity, e, of 20 mm, of which three specimens were bonded with 2-component polyurethane (Casco 8356+1821). The expected plateau shaped load-deflection curve was not fully obtained except in a few cases. In the evaluation of total fracture energy, it was considered most appropriate to evaluate the fracture energy from the maximum load at failure. In Tab. 4.10 the total fracture energy, G_f^{tot}, of the resorcinol/phenol and the PU specimens, is given. The tests do not indicate any significant influence of mixed-modity on the fracture energy. The mode-I fracture energy is larger than expected from the material tests, while the shear mode values are less.

To verify the assumption of beam theory, an FE-analysis was performed. The

Table 4.10: *Mixed-mode-bending test results and evaluated properties. In the evaluation the stiffness moduli were chosen to be $E_{al} = 70$ GPa and $E_w = 13$ GPa. Please note that the results are strongly affected by wood failure implying increased fracture surface.*

Specimen	e [mm]	P_{max} [kN]	ψ_G [°]	G_f^{tot} [kNm/m^2]
Solid wood	0	5.2	90	1.4
and	0	3.7	90	0.7
R/P	0.01	3.3	67	0.66
	0.02	3.9	49	1.4
	0.02	3.6	49	1.2
	0.02	3.1	49	0.86
	0.075	1.2	17	0.85
	0.15	0.77	9	1.3
	0.15	0.55	9	0.67
	0.15	0.61	9	0.82
	0.15	0.32	9	0.22
	0.15	0.61	9	0.82
Composite	0.02	3.3	42	0.67
R/P	0.02	5.6	42	1.94
Composite	0.02	5.6	42	1.9
PU	0.02	6.1	42	2.3
	0.02	5.8	42	2.1
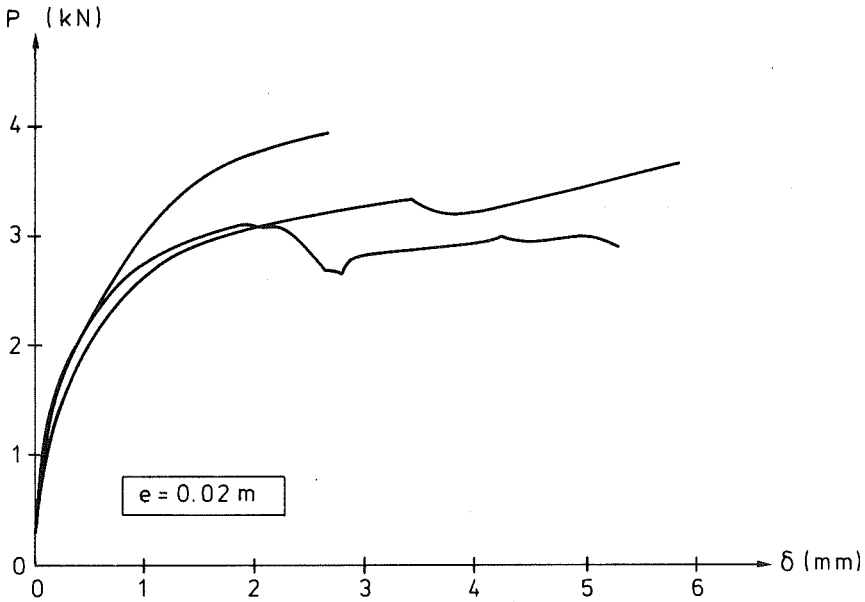
Figure 4.37: *Load deflection curves of MMB specimens of solid wood bonded with resorcinol/phenol with $e = 0.02$ m.*

program used was CALFEM with a self-correcting incremental solution scheme as will be described in Sec. 5.2.4. In the analysis the equation system involved 3412 degrees of freedom and the number of steps was approximately 300-400 for each eccentricity. The first 50 mm of the bond line was modelled with bond elements of 0.5 mm length, while the last 300 mm was modelled with 2 mm elements. In Fig. 4.38 the force-deformation curves of three different eccentricities are given, the deformation being that of the point of load application. The shape is close to plateau-like with a slight slope in the post-peak region. The maximum load values may be compared to those obtained from linear elastic fracture mechanics. Eqs. 3.14 and 3.15 may be rewritten including critical values, to an expression for critical load

$$P_c = \sqrt{\frac{(G_{Ic}^{\prime a} + G_{IIc}^a)Eb'bh}{3\left(\dfrac{e}{h}\right)^2 + 4}} \tag{4.4}$$

where $G_{Ic}^{\prime a}$ and G_{IIc}^a are the present energy release rates for the given mixed-modity, which have to be determined from some fracture criterion. Using the criterion commonly used in LEFM in Eq. (2.19) with $m = n = 2$, the total energy release
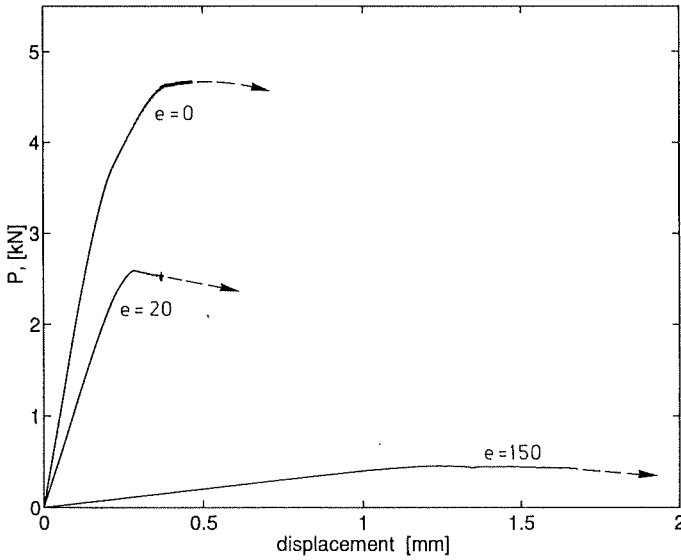
Figure 4.38: *Calculated force-deformation curves of the MMB-specimen with differ-ent eccentricities of load application. Material parameters are: $\tau_f = 10$ MPa, $\sigma_f = 6.5$ MPa, $G_{f,s} = 980$ Nm/m^2 and $G_{f,n} = 360$ Nm/m^2.*

rate may be given as

$$G^a_{Ic} + G^a_{IIc} = G_{Ic} \left\{ \frac{0.75 \left(\dfrac{e}{h}\right)^2 + 1}{0.75 \left(\dfrac{e}{h}\right)^2 + \dfrac{G_{Ic}}{G_{IIc}}} \right\} \tag{4.5}$$

The results are given in Tab. 4.11 for which the LEFM results are based on Eq. (4.5). If the *Wu*-criterion was used, i.e. $m = 1, n = 2$, P_c for $e = 0.02$ m would adopt the value 2.25 kN. There is a deviation between the LEFM- and the FE-analysis. For the largest eccentricity the deviation of approximately 50 N is mainly due to limitations of beam theory in describing the deformations of the specimen. For $e = 0.02$ m, the difference will to a large extent depend on the chosen failure criterion and mixed-mode model.

In the comparison to the test results one more factor has to be considered, namely the wood failure, which tends to increase at increasing peel stresses. Wood failure implies increased failure surface and consequently increased failure load. Hence, it is difficult to determine to what extent the difference in calculated and recorded results is due to improper theoretical models, or is a consequence of underestimated

Table 4.11: *Calculated and recorded maximum load capacity (dimension in kN) of the MMB-specimen.*

	e=0 [m]	e=0.02 [m]	e=0.15 [m]
P_{LEFM}	4.4	2.5	0.41
P_{FEM}	4.7	2.6	0.46
P_{TEST}	4.4	3.5	0.57

fracture surface. A qualified assumption is that for $e = 0.15$ m, the main reason is wood failure, which then could also be of great influence for the eccentricity of 0.02 m.

One outcome from the FE-analysis with the proposed bond model is that the mixed-modity will vary along the fracture zone. In Fig. 4.39 the normal and shear stress distributions are given for the specimen with 150 mm of eccentricity, at the elastic state, the state of maximum global load and during fracture propagation. The ratio of τ/σ will vary considerably within the fracture zone. Furthermore, the size and shape of the propagating fracture zone seem to be approximately constant, but the ratio of peak stresses is different in comparison to the elastic state.

A notable observation from the tests is, that for a predominant shear stress state, the adhesive properties determines the fracture process of the MMB-specimen. For increasing normal stresses, the risk for wood failure will increase implying the wood properties to be those of significance.

The MMB-specimen may be considered to be well adopted for mixed-mode fracture propagation testing of comparatively weak adhesives, i.e. specimens that are expected to reveal bond failure for arbitrary mode-mixity. This is the case when testing weaker adhesives than in the present test series, and also when testing stronger adherend materials, such as metals or fibre-composites.
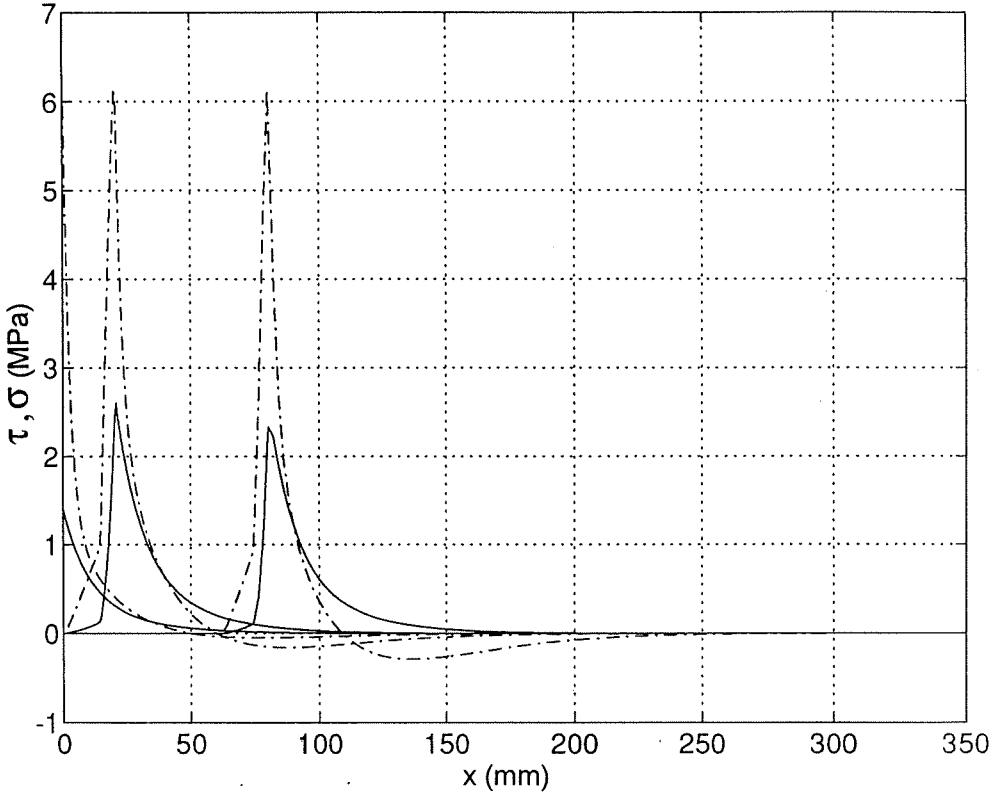
Figure 4.39: *Stress distribution in MMB specimen with e=150 mm, in the elastic region (P=197 N), at peak global force (P=456 N) and during fracture propagation (P=447 N). Shear stress(–), normal stress(-.). x denotes the distance from the bond end.*

5. FINITE ELEMENT CALCULATIONS

5.1. General Remarks

In Section 2.4.3 a mixed-mode constitutive model of adhesive bond lines was proposed. To handle such models in analysis of arbitrary joints, numerical methods are required. The finite element method is chosen because it is the predominating numerical method in structural analysis today.

5.1.1. The finite element method

The finite element method, FEM, is a numerical approach by which differential equations can be solved. Differential equations in turn describe physical phenomena over certain regions, e.g. the deflection of a wood beam or the heat flow in a wall. In FEM such regions are divided into smaller parts called *finite elements*. Numerical approximation and integration is performed over each element and element equations are obtained. The contribution of each element is subsequently added to a global system of equations. By solving this system of equations the distribution of the quantity studied is determined.

5.1.2. Present FE codes

In the present analysis the research code CAMFEM [22] has been used. At an early state of the present study CAMFEM was used as an independent fortran-based finite element code. CAMFEM may be considered to be a library of well-documented FE commands. For each command a set of arguments is required, and the user performs calculations by interactively giving commands in the program or alternatively, for larger problems, writing a command list which will be run by the program. CAMFEM is well adapted as a research code as it is flexible and comparatively easy to adjust to fit any specific application. Hence, the program has been supplemented with code related to the present study. All major steps in the solution procedure must be given by the user and, hence, it requires the user to be familiar with the structure of FE programs. In the development of CAMFEM the effort has been focused on the numerical methods and analysis. Accordingly, there are limited pre- or post processor facilities connected to the program at this state. In the present analysis, however, a mesh generator [60] was adopted to suit the input files of the program. The research code CAMFEM is closely related to the educational code

CALFEM [23]. Parallel to this study the features of CALFEM were implemented as a toolbox in the code MATLAB [65], which is a computing environment suitable for matrix computation, including graphics facilities. The implementation of the program to MATLAB has conciderably improved the calculation capacity as well as the visualization facilities for the post processing. It was considered adequate to also translate the code related to this study into the MATLAB environment. Hence, the computations performed at a late state of the present study have been carried out in the MATLAB environment.

5.2. Finite Element Implementation

5.2.1. Basic equations

Descriptions of how to establish finite element equations from basic equations of equilibrium are commonly found in the literature. Nevertheless, it is found adequate to make a brief description of some basic steps in the derivation. Except for the bond description, the present description corresponds closely to that of *Dahlblom* [24] who previously used CAMFEM in the analysis of concrete with regard to environmental influence.

The equations of equilibrium are

$$\frac{\partial \sigma_{ji}}{\partial x_j} + b_i = 0 \qquad (5.1)$$

where σ is the stress tensor, b is the body force vector and x_j denotes a Cartesian coordinate system. For the tractions, t, acting on the surface, S, surrounding the body holds

$$t_i = \sigma_{ji} n_j \qquad (5.2)$$

where n is the outward unit vector normal to the surface, S.

In order to obtain a finite element formulation, a weak formulation will be established. Multiplying Eq. (5.1) by a set of weighting functions, v_{im}, and integrating over the volume V, we obtain

$$\int_V v_{im} \frac{\partial \sigma_{ji}}{\partial x_j} dV + \int_V v_{im} b_i dV = 0 \qquad (5.3)$$

which by means of Gauss's theorem and Eq. (5.2) may be rewritten to

$$\int_V \frac{\partial v_{im}}{\partial x_j} \sigma_{ji} dV = \int_V v_{im} b_i dV + \int_S v_{im} t_i dS \qquad (5.4)$$

The equilibrium equation, Eq. (5.1), is also valid in rate form and as v_{im} is set to be independent of time, Eq. (5.4) may be directly transformed into

$$\int_V \frac{\partial v_{im}}{\partial x_j} \dot{\sigma}_{ji} dV = \int_V v_{im} \dot{b}_i dV + \int_S v_{im} n_j \dot{t}_i dS \qquad (5.5)$$

The stress rate is related to the strain rate through the constitutive equations of the present materials which, for the bond line, were discussed in section 2.4.3. The stress-strain relation may be expressed as

$$\dot{\sigma}_{ij} = D_{ijpq}\dot{\epsilon}_{pq} \tag{5.6}$$

where D is the tangential material stiffness tensor and $\dot{\epsilon}$ is the strain rate tensor which is given by the linear kinematic relation

$$\dot{\epsilon}_{pq} = \frac{1}{2}\left(\frac{\partial \dot{u}_p}{\partial x_q} + \frac{\partial \dot{u}_q}{\partial x_p}\right) \tag{5.7}$$

where $\mathbf{u}$ is the displacement vector. Combining Eqs. (5.5), (5.6) and (5.7) and noting that the stress and strain rate tensors $\dot{\sigma}$ and $\dot{\epsilon}$ are symmetric we obtain the *weak formulation*, expressed as

$$\int_V \frac{\partial v_{im}}{\partial x_j}D_{ijpq}\frac{\partial \dot{u}_p}{\partial x_q}dV = \int_V v_{im}\dot{b}_idV + \int_S v_{im}\dot{t}_idS \tag{5.8}$$

The weak formulation forms the base of the FE formulation. The advantage of the weak form is that the unknown function, u, is differentiated only once in comparison to the strong form, Eqs. (5.1), (5.6) and (5.7), where the second derivative of u enters. Accordingly, by using the weak formulation fewer requirements are put on the approximation of u.

5.2.2. Finite element equations

In order to obtain finite element equations, the displacements u_p are expressed in an approximate form as a function of displacements of the nodes connecting the finite elements. These nodal displacements are denoted $\bar{u}_n$ and they relate to u_p as

$$u_p = N_{pn}\bar{u}_n \tag{5.9}$$

and correspondingly in rate form, where N_{pn} are interpolation functions and index n denotes the equation number or the degree of freedom, *dof*, and p is a component in the Cartesian coordinate system. By means of the so-called Galerkin method these interpolation functions are chosen to be identical to the weighting functions, i.e. $v_{im} = N_{im}$. Hence Eq. (5.8) may be expressed as

$$K_{mn}\dot{\bar{u}}_n = \dot{P}_m \tag{5.10}$$

where K_{mn} and $\dot{P}_m$ are defined as tangent stiffness and rate of load, given by

$$K_{mn} = \int_V \frac{\partial N_{im}}{\partial x_j}D_{ijpq}\frac{\partial N_{pn}}{\partial x_q}dV \tag{5.11}$$

$$\dot{P}_m = \int_V N_{im}\dot{b}_idV + \int_S N_{im}\dot{t}_idS \tag{5.12}$$

In rational finite element programming a matrix formulation is required. By introducing the matrices N_n, $\tilde{\nabla}$, B_n, $\dot{t}$, $\dot{b}$, and $\dot{\sigma}$, $\dot{\epsilon}$ and D. Eqs.(5.6) and (5.11)-(5.12) may be written in matrix form as

$$\dot{\sigma} = D\dot{\epsilon} \tag{5.13}$$

$$K_{mn} = \int_V B_m^T D B_n \, dV \tag{5.14}$$

$$\dot{P}_m = \int_S N_m^T \dot{t} \, dS + \int_V N_m^T \dot{b} \, dV \tag{5.15}$$

where for a general three-dimensional case

$$N_n = \begin{bmatrix} N_{1n} \\ N_{2n} \\ N_{3n} \end{bmatrix} ; \qquad \dot{t} = \begin{bmatrix} \dot{t}_1 \\ \dot{t}_2 \\ \dot{t}_3 \end{bmatrix} ; \qquad \dot{b} = \begin{bmatrix} \dot{b}_1 \\ \dot{b}_2 \\ \dot{b}_3 \end{bmatrix} \tag{5.16}$$

$$\tilde{\nabla} = \begin{bmatrix} \dfrac{\partial}{\partial x_1} & 0 & 0 \\[2mm] 0 & \dfrac{\partial}{\partial x_2} & 0 \\[2mm] 0 & 0 & \dfrac{\partial}{\partial x_3} \\[2mm] \dfrac{\partial}{\partial x_2} & \dfrac{\partial}{\partial x_1} & 0 \\[2mm] 0 & \dfrac{\partial}{\partial x_3} & \dfrac{\partial}{\partial x_2} \\[2mm] \dfrac{\partial}{\partial x_3} & 0 & \dfrac{\partial}{\partial x_1} \end{bmatrix} ; \qquad B_n = \tilde{\nabla} N_n = \begin{bmatrix} \dfrac{\partial N_{1n}}{\partial x_1} \\[2mm] \dfrac{\partial N_{2n}}{\partial x_2} \\[2mm] \dfrac{\partial N_{3n}}{\partial x_3} \\[2mm] \dfrac{\partial N_{1n}}{\partial x_2} + \dfrac{\partial N_{2n}}{\partial x_1} \\[2mm] \dfrac{\partial N_{2n}}{\partial x_3} + \dfrac{\partial N_{3n}}{\partial x_2} \\[2mm] \dfrac{\partial N_{1n}}{\partial x_3} + \dfrac{\partial N_{3n}}{\partial x_1} \end{bmatrix} \tag{5.17}$$

$$\dot{\sigma} = \begin{bmatrix} \dot{\sigma}_{11} \\ \dot{\sigma}_{22} \\ \dot{\sigma}_{33} \\ \dot{\sigma}_{12} \\ \dot{\sigma}_{23} \\ \dot{\sigma}_{31} \end{bmatrix} \qquad \dot{\epsilon} = \begin{bmatrix} \dot{\epsilon}_{11} \\ \dot{\epsilon}_{22} \\ \dot{\epsilon}_{33} \\ 2\dot{\epsilon}_{12} \\ 2\dot{\epsilon}_{23} \\ 2\dot{\epsilon}_{31} \end{bmatrix} \qquad D = \begin{bmatrix} D_{1111} & D_{1122} & D_{1133} & D_{1112} & D_{1123} & D_{1131} \\ D_{2211} & D_{2222} & D_{2233} & D_{2212} & D_{2223} & D_{2231} \\ D_{3311} & D_{3322} & D_{3333} & D_{3312} & D_{3323} & D_{3331} \\ D_{1211} & D_{1222} & D_{1233} & D_{1212} & D_{1223} & D_{1231} \\ D_{2311} & D_{2322} & D_{2333} & D_{2312} & D_{2323} & D_{2331} \\ D_{3111} & D_{3122} & D_{3133} & D_{3112} & D_{3123} & D_{3131} \end{bmatrix} \tag{5.18}$$

By means of Eq. (5.10) and introduction of the matrices above, a finite element formulation is obtained. In the solution, adequate boundary conditions have to be

considered. The solution of Eq. (5.10) is the rate of displacements of the nodal points, $\dot{\tilde{u}}$. The strain rates corresponding to these displacement rates are given by the relation

$$\dot{\epsilon} = \mathsf{B_n}\dot{\tilde{u}}_n \tag{5.19}$$

and correspondingly, with known strain rates the stress rates can be determined from Eq. (5.13).

A major concept of the finite element method is that the interpolation functions, N_{in}, are chosen to be non-zero in a limited subdomain only. Hence, the integration can be split up into integration over each subdomain, i.e. *finite element*. A system of equations can be established for each element and subsequently be assembled into a global equation system.

The finite element formulation above is made for a general 3-D case. The present analysis is performed in 2-D, plane stress, which infers that the matrices of Eqs. (5.16) and (5.17) will be reduced to include only two directions, i.e.

$$\mathsf{N_n} = \left[\begin{array}{c} N_{1n} \\ N_{2n} \end{array} \right]; \qquad \dot{\mathsf{t}} = \left[\begin{array}{c} \dot{t}_1 \\ \dot{t}_2 \end{array} \right]; \qquad \dot{\mathsf{b}} = \left[\begin{array}{c} \dot{b}_1 \\ \dot{b}_2 \end{array} \right] \tag{5.20}$$

$$\tilde{\nabla} = \left[\begin{array}{cc} \dfrac{\partial}{\partial x_1} & 0 \\[3mm] 0 & \dfrac{\partial}{\partial x_2} \\[3mm] \dfrac{\partial}{\partial x_2} & \dfrac{\partial}{\partial x_1} \end{array} \right]; \qquad \mathsf{B_n} = \tilde{\nabla}\mathsf{N_n} = \left[\begin{array}{c} \dfrac{\partial N_{1n}}{\partial x_1} \\[3mm] \dfrac{\partial N_{2n}}{\partial x_2} \\[3mm] \dfrac{\partial N_{1n}}{\partial x_2} + \dfrac{\partial N_{2n}}{\partial x_1} \end{array} \right] \tag{5.21}$$

and, furthermore, the stress-strain relation of Eq. (5.6) for plane stress and orthotropic linear elastic material will take the form

$$\left[\begin{array}{c} \dot{\sigma}_{11} \\ \dot{\sigma}_{22} \\ \dot{\sigma}_{12} \end{array} \right] = \dfrac{E_1 E_2}{1 - \nu_{12}\nu_{21}} \left[\begin{array}{ccc} \dfrac{1}{E_2} & \dfrac{\nu_{12}}{E_2} & 0 \\[3mm] \dfrac{\nu_{21}}{E_1} & \dfrac{1}{E_1} & 0 \\[3mm] 0 & 0 & \dfrac{1 - \nu_{12}\nu_{21}}{E_1 E_2}G_{12} \end{array} \right] \left[\begin{array}{c} \dot{\epsilon}_{11} \\ \dot{\epsilon}_{22} \\ 2\dot{\epsilon}_{12} \end{array} \right] \tag{5.22}$$

Four node isoparametric elements with four integration points are used. The choice of nodal displacements and interpolation functions for this element type may be found in e.g. *Zienkiewicz* [104].

5.2.3. Implementation of the mixed-mode bond model

The constitutive relation of the bond line was discussed in Sec. 2.4.3. The bond line is modelled as a surface for which the properties are independent of the initial thickness. Instead restraints are put on the connection between the adjacent nodes of the two adherends in accordance with the chosen material's characteristics. The assumption of no initial thickness means that the stress state relates to the actual state of deformation, as strains have no physical interpretation. The stress-deformation relation was given by Eq. (2.28) as

$$
\begin{bmatrix} \dot{\sigma} \\ \dot{\tau} \end{bmatrix} = \begin{bmatrix} D_{nn} & D_{ns} \\ D_{sn} & D_{ss} \end{bmatrix} \begin{bmatrix} \dot{\delta}_n \\ \dot{\delta}_s \end{bmatrix}
\tag{5.23}
$$

where the indices n and s stand for normal and shear direction respectively and where the expression for the stiffness components, D_{ij}, were given by Eq.(2.46) i.e.

$$
D_{nn} = \frac{\partial \sigma(\delta_n, \delta_s)}{\partial \delta_n} \quad , \quad D_{ns} = \frac{\partial \sigma(\delta_n, \delta_s)}{\partial \delta_s}
$$

$$
D_{sn} = \frac{\partial \tau(\delta_n, \delta_s)}{\partial \delta_n} \quad , \quad D_{ss} = \frac{\partial \tau(\delta_n, \delta_s)}{\partial \delta_s}
\tag{5.24}
$$

The procedure for determining the stiffness components, D_{ij}, was described in Sec. 2.4.3.

The deformations δ_n and δ_s are determined from the present state of nodal displacements through the expression

$$
\begin{bmatrix} \dot{\delta}_n \\ \dot{\delta}_s \end{bmatrix} = \begin{bmatrix} 0 & -1 & 0 & 1 \\ -1 & 0 & 1 & 0 \end{bmatrix} \begin{bmatrix} \dot{u}_1 \\ \dot{u}_2 \\ \dot{u}_3 \\ \dot{u}_4 \end{bmatrix}
\tag{5.25}
$$

with definitions in Fig. 2.15. The present bond element is generated as a four node element even though there is no coupling between the two sets of springs in the respective ends. This facilitates using most standard mesh generators, and more important, the active length, ℓ_e, of each spring, i.e. the bond length represented by each spring, is implied as well as the slope of the bond line in relation to the coordinate system. Hence, nodal forces can be divided by the corresponding bond area, $0.5\ell_e b$, cf. Fig. 5.1, and straightforwardly expressed as corresponding stresses, and the transformation of stresses into an arbitrary coordinate system is standard.
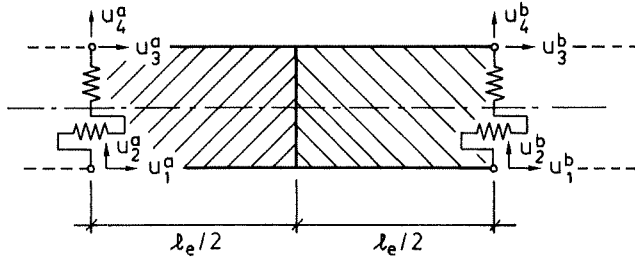
Figure 5.1: *Bond element.*

For the complete element

$$
\begin{bmatrix} \dot{\delta}_n^a \\ \dot{\delta}_s^a \\ \dot{\delta}_n^b \\ \dot{\delta}_s^b \end{bmatrix} = \begin{bmatrix} 0 & -1 & 0 & 1 & 0 & 0 & 0 & 0 \\ -1 & 0 & 1 & 0 & 0 & 0 & 0 & 0 \\ 0 & 0 & 0 & 0 & 0 & -1 & 0 & 1 \\ 0 & 0 & 0 & 0 & -1 & 0 & 1 & 0 \end{bmatrix} \begin{bmatrix} \dot{u}_1^a \\ \dot{u}_2^a \\ \dot{u}_3^a \\ \dot{u}_4^a \\ \dot{u}_1^b \\ \dot{u}_2^b \\ \dot{u}_3^b \\ \dot{u}_4^b \end{bmatrix} \tag{5.26}
$$

where displacement components are given in Fig. 5.1. The rotation of the element is determined from the initial coordinates of the nodal points.

In the present strength analysis, the longitudinal stresses and strains are neglected. As a check, the longitudinal strain, ϵ_ℓ, can be obtained by the expression

$$
\dot{\epsilon}_\ell = \frac{(\dot{u}_3^b + \dot{u}_1^b) - (\dot{u}_3^a + \dot{u}_1^a)}{2\ell_e} \tag{5.27}
$$

5.2.4. Solution procedure

The description of the bond line constitutive model in Sec. 2.4.3 implies that the stiffness matrix will be nonsymmetric in the softening region. Many FE programs cannot handle large nonsymmetric equation systems. In its fortran version CAM-FEM handles non-symmetry only by solving the full stiffness matrix. However, already at a rather limited number of degrees of freedom the major part of the computer time will be consumed to add and multiply figures of zero. In the MATLAB environment the matrices can be stored and solved in sparse form. Only the nonzero values will hence be stored, including two additional numbers to define its position in the full matrix. However, for a typical calculation, the finger joints in Sec. 5.3.1,

only approximately 1 % of the components of the stiffness matrix will be nonzero. Accordingly, the space required to store the stiffness matrix is reduced by about 97 %. The time to solve the equation system was in this case reduced from several minutes to a few seconds on the same computer.

In the solution of the non-linear problem an incremental procedure is applied, where a linear relation within each increment is assumed. The nonlinearity of the constitutive relation assumed, may result in that the equations of equilibrium are not satisfied exactly. A measure of the deviation is provided by the out-of-balance forces $P_m^\star$, which are defined as the difference between the applied loads, i.e. the right hand side of Eq. (5.4), and the internal forces, i.e. the left hand side of Eq. (5.4). Thus,

$$P_m^\star = \int_V v_{im} b_i dV + \int_S v_{im} n_j \sigma_{ij} dS - \int_V \frac{\partial v_{im}}{\partial x_j} \sigma_{ji} dV \tag{5.28}$$

Applying the definitions above and adopting rate form, the rate of change of the out-of-balance forces, $\dot{P}_m^\star$, can be expressed as the rate of the sum of the applied forces minus the integrated internal stress rates determined from the constitutive model, i.e. in matrix form

$$\dot{\mathsf{P}}_\mathsf{m}^\star = \dot{\mathsf{P}}_\mathsf{m} - \int_V \mathsf{B}_\mathsf{m}^\mathsf{T} \dot{\sigma} dV \tag{5.29}$$

use of Eqs. (5.13), (5.14) and (5.19) yields

$$\mathsf{K}_\mathsf{mn} \ddot{\mathsf{u}}_\mathsf{n} = \dot{\mathsf{P}}_\mathsf{m} - \dot{\mathsf{P}}_\mathsf{m}^\star \tag{5.30}$$

where K_mn is the tangential stiffness. The evaluation of Eq.(5.30) is performed by a so called Euler forward expression assuming a linear relation from time t to $t + \delta t$, i.e.

$$\mathsf{K}_\mathsf{mn}(t)\delta \bar{\mathsf{u}}_\mathsf{n} = \delta \mathsf{P}_\mathsf{m} - \delta t \dot{\mathsf{P}}_\mathsf{m}^\star \tag{5.31}$$

where $\mathsf{K}_\mathsf{mn}(t)$ is the tangential stiffness at time t, $\delta \bar{\mathsf{u}}_\mathsf{n}$ the change of nodal displacement from time t to $t + \delta t$, and $\delta \mathsf{P}_\mathsf{m}$ the incremental load. In order to guide the solution towards the true solution, it is desired to reduce the magnitude of $\mathsf{P}_\mathsf{m}^\star(t)$ to zero during the time increment. Therefore the rate of change of the out-of-balance forces are assumed to be

$$\dot{\mathsf{P}}_\mathsf{m}^\star = -\frac{1}{\delta t} \mathsf{P}_\mathsf{m}^\star(t) \tag{5.32}$$

Substituting Eq. (5.32) into Eq. (5.31) yields

$$\mathsf{K}_\mathsf{mn}(t)\delta \bar{\mathsf{u}}_\mathsf{n} = \delta \mathsf{P}_\mathsf{m} + \mathsf{P}_\mathsf{m}^\star(t) \tag{5.33}$$

This procedure is called a self-correcting solution form [89], since the solution is guided towards a true solution and it is illustrated as a flow chart in Fig. 5.2.

```
                    ┌─────────────────┐
                    │      START      │
                    └─────────────────┘
                             │
                    ┌─────────────────┐
                    │   DATA INPUT    │
                    └─────────────────┘
                             │
                ┌────────────────────────────┐
    ┌──────────▶│   ESTABLISH THE TANGENT    │
    │           │      STIFFNESS MATRIX      │
    │           └────────────────────────────┘
    │                        │
    │           ┌────────────────────────────┐
    │           │   REARRANGE FOR BOUNDARY   │
    │           │        CONDITIONS          │
    │           └────────────────────────────┘
    │                        │
    │           ┌────────────────────────────┐
    │           │  INCREMENT THE PRESCRIBED  │
    │           │       DISPLACEMENTS        │
    │           └────────────────────────────┘
    │                        │
    │           ┌────────────────────────────┐
    │           │   SOLVE THE EQUATION SYSTEM│
    │           └────────────────────────────┘
    │                        │
    │           ┌────────────────────────────┐
    │           │ CALCULATE TOTAL ELEMENT    │
    │           │ STRESSES AND STRAIN OR     │
    │           │ DEFORMATIONS               │
    │           └────────────────────────────┘
    │                        │
    │           ┌────────────────────────────┐
    │           │ CALCULATE THE OUT-OF-      │
    │           │ BALANCE FORCE ...          │
    │           └────────────────────────────┘
```

INCREMENTAL LOOP

ESTABLISH THE TANGENT STIFFNESS MATRIX

REARRANGE FOR BOUNDARY CONDITIONS

INCREMENT THE PRESCRIBED DISPLACEMENTS

SOLVE THE EQUATION SYSTEM

CALCULATE TOTAL ELEMENT STRESSES AND STRAIN OR DEFORMATIONS

CALCULATE THE OUT-OF-BALANCE FORCE AS THE APPLIED FORCE MINUS THE INTEGRATED INTERNAL STRESSES

ADD THE OUT-OF-BALANCE FORCE TO THE INCREMENTAL LOAD VECTOR

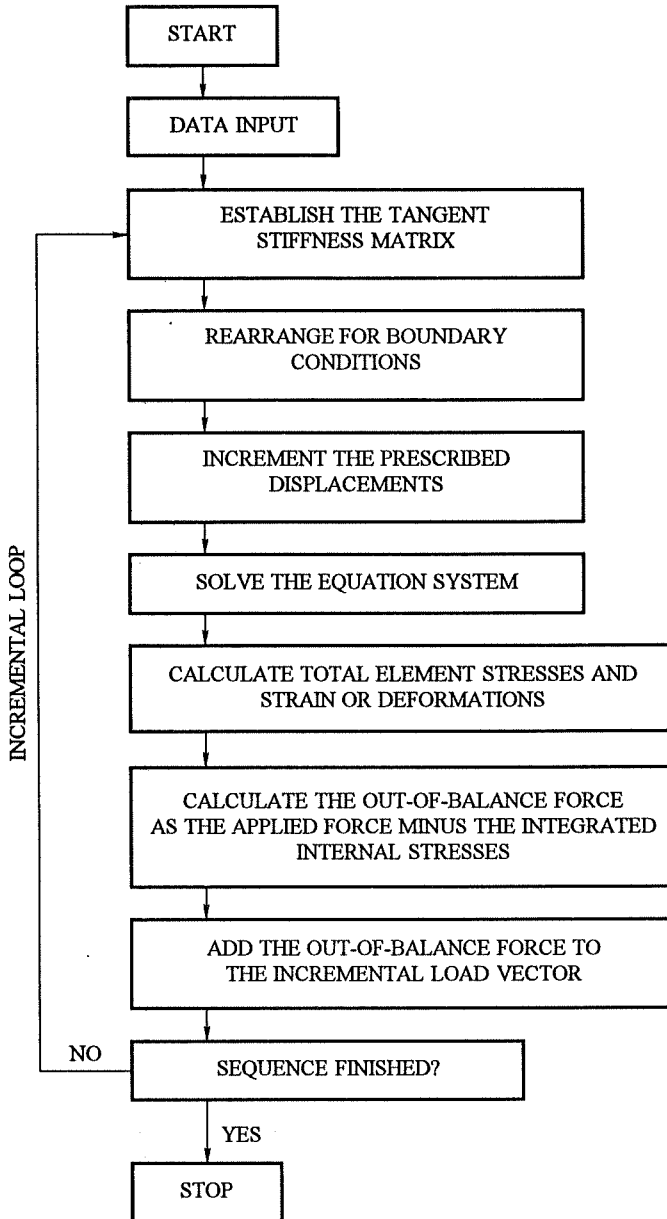NO ← SEQUENCE FINISHED?

YES

STOP

Figure 5.2: *Flow chart of the present nonlinear FE analysis.*

5.3. Numerical examples

5.3.1. Finger joints

Finger joining as a means of splicing wood lengthwise was introduced in the late 1940s and it has enjoyed continuously increased acceptance. For instance, the method may today be considered as a prerequisite for the modern glulam industry.

A finger joint may be regarded as a series of scarf joints separated by blunt tips at the end of the scarfs. A scarf joint implies, from a mechanical point of view, a rather uniform stress state, and with a sufficiently small slope it will produce joints of strength comparable to solid timber members. The specification of a minimum required slope varies in the literature, but should be in the range of 1/10. Accordingly, the use of scarf joints implies that the material waste is at least 10 times the height of the cross section for each joint. The main reasons for the slope requirement is that the bond area increases for decreased slope and, furthermore, the gluability of wood perpendicular to grain is poor in comparison to along the grain and that adhesive joints, in general, involve a superior load transferring ability through shear stresses in comparison to normal stresses.

The introduction of finger joints entails less waste of wood material. However, due to production limitations there will be a cross-sectional reduction of the member due to blunts at the finger tips and roots. This cross-sectional reduction tends to increase for increasing slope. Accordingly, by improving the adhesive bonding by decreasing the finger slope, the risk of tensile failure in the region of reduced cross section may be increased. For evaluation of failure due to cross sectional reduction a strength analysis of tensile failure in finger joints with regard to stress concentrations at the finger tip gaps is given by *Qu and Fan* [74].

As the use of finger joints has increased, it has been followed by several investigations with the aim of finding improved or optimal design. Tensile tests of finger joints have been presented in e.g. [49, 50, 59, 76, 86, 102], to study geometric factors such as slope, finger length and tip thickness, but also the stiffness and density of the adjoining wood material. A comprehensive test programme for finger joints in bending is presented by *Colling* [20, 28]. As a general outcome of these tests, it may be concluded that the load carrying capacity of a finger joint is improved by decreasing slope angle, decreasing tip gap size, increased stiffness of the wood and to some extent by increased finger length.

The influence of adhesive properties has been tested only to a minor extent. *Goth and Radović* [35] report that the short term finger joint strength can be improved by a factor of 50-70 % by substituting a standard brittle resorcinol/phenol adhesive with a tough one-component polyurethane. In the present study, the influence of the bond line parameters local strength and fracture energy are studied by means of finite element analysis.

The finger joints involved in the study are identical, with regards to designation
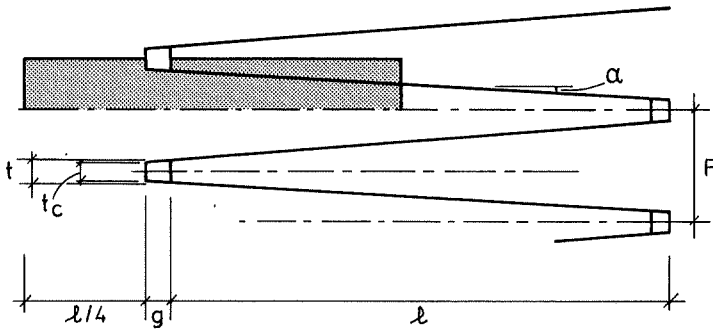
Figure 5.3: *Finger geometry. The shaded area is the analysed symmetric part.*

Table 5.1: *Geometry of the analysed finger joint profiles.*

Profile	Dimensions [mm]				α	Cross sectional reduction $1 - \frac{t}{p}$
	ℓ	p	t_c	g		
I-15	15	3.8	0.42	1.1	10.4	0.84
I-20m	20	5.0	0.5	1.2	10.3	0.85
I-20	20	6.2	1.0	0.6	9.8	0.82
I-30	30	6.2	0.6	1.5	12.4	0.86

and geometry, to those analysed by *Aicher and Klöck* [2]. They analysed the load capacity of four different standardized finger joint geometries by means of linear and non-linear stress analysis as well as with energy release rate approach by means of the compliance method , cf. Eq. (2.11). The finger geometries are given in Tab. 5.1 with definitions in Fig. 5.3. The slope α is the angle between the finger and the lengthwise direction of the member

$$\alpha = \arctan\left(\frac{0.5p - t_c}{\ell + g}\right) \tag{5.34}$$

Due to the symmetry of the finger joints it was decided, for the general case, only to analyse the shaded area of Fig. 5.3. The boundary conditions of this quarter of a finger are given in Fig. 5.4. Loading is applied by incremental displacements
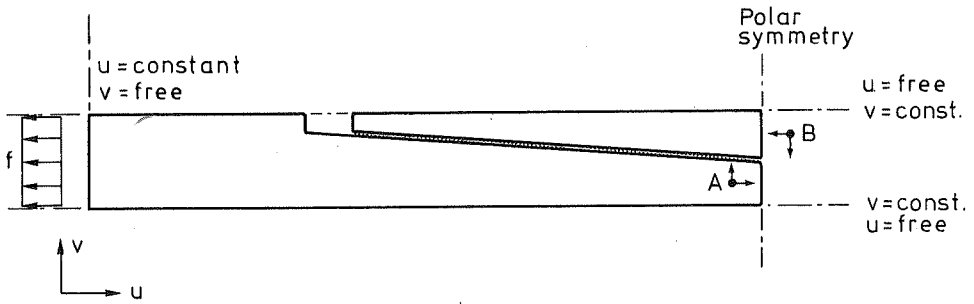
Figure 5.4: *Boundary conditions in finger joint analysis.*

of the horizontal degrees of freedom, *dofs*, on the left boundary. The upper and lower sides are assumed to be parallel, also during deformation. This is achieved by prescribing the vertical dofs on the lower boundary to be zero and the vertical dofs on the upper side to be equal. The distance between the upper and lower boundary is free to change during the course of loading.

On the right symmetry line there will be polar symmetry, implying that the deformations of points A and B will be equal but opposite. The polar symmetry condition presumes that the stiffnesses of the lower and upper wood materials are equal.

The implementation of these boundary conditions is made by expressing all vertical dofs on the upper as one dof, and correspondingly for the lower boundary. This can be achieved through a transformation matrix, C, given by

$$\dot{u}^c = C\dot{u} \qquad (5.35)$$

where $\dot{u}^c$ is the reduced deformation vector including the restraints from the boundary conditions. C enters the equation system, Eq. (5.10), as

$$C^T K C \dot{u} = C^T \dot{P} \qquad \Leftrightarrow \qquad K^c \dot{u} = \dot{P}^c \qquad (5.36)$$

In the solution scheme, the solving of Eq. (5.36) is followed by determination of the deformations $\dot{u}^c$ by Eq. (5.35). Following the self-correcting solution procedure of Section 5.2.4, the nodal reactions, Q, will be determined as

$$\dot{Q} = K\dot{u}^c - \dot{P} \qquad (5.37)$$

The total reaction for a linear elastic step, will be equal to the nodal components of the integrated element stresses, R_i, of the deformed body. For a non-linear step the difference between the Q and R_i will form the out-of-balance force vector, $P_m^\star$ in Eq. (5.33).
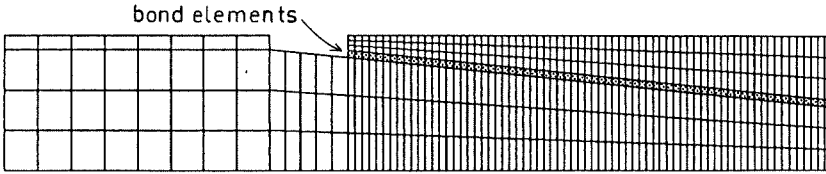
Figure 5.5: *Element mesh of I-15 joint.*

For all four geometries the same number of elements is used. The element mesh of I-15 is given in Fig. 5.5. Accordingly, for the large joints, larger elements were used, e.g. the bond element lengths are 0.0993, 0.134, 0.139 and 0.203 mm, respectively, for the geometries in Tab. 5.1.

The aim of this numerical finger joint study has been to compare the load-bearing capacity of the different joints in Tab. 5.1, and to make a parametric study of how the involved material properties affect the global finger joint strength. The bond line is 0.1 mm thick and the properties used in the analysis are given in Fig. 5.6, and the powers $m = n = 2$. The wood material is assumed to be linear elastic with properties [40]: $E_x = 13110$ MPa, $E_y = 161$ MPa, $G_{xy} = 471$ MPa and $\nu_{xy} = 0.53$. The plane stress D-matrix, in accordance with Eq. (5.22), will hence adopt the values (dimensions in MPa)

$$D_w = \begin{bmatrix} 13155 & 86 & 0 \\ 86 & 162 & 0 \\ 0 & 0 & 471 \end{bmatrix} \tag{5.38}$$

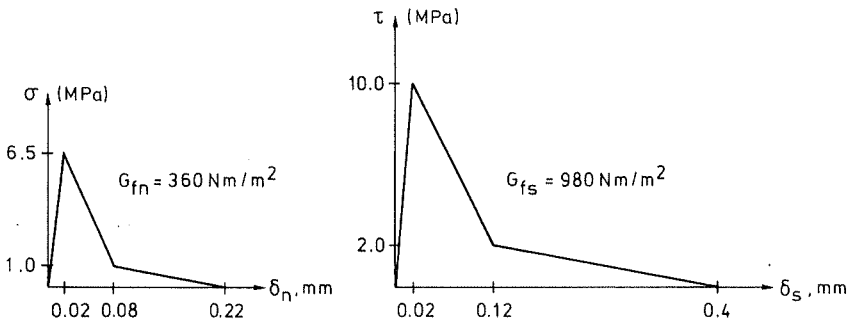The parametric study was made by increasing the different properties one at

Figure 5.6: *Uniaxial bond line properties.*

Table 5.2: *Difference in input for the parametric study.* E_w *denotes wood stiffness with indices* ℓ *and* u *for lower and upper finger.*

Strengh parameter	Characteristics
f_1	Reference
f_2	σ_f and τ_f: $+10$ %
f_3	G_{fn} and G_{fs}: $+10$ %
f_4	E_w $+10$ %, (Eq. (5.38)$\cdot$1.1)
f_5	$f_2 + f_3 + f_4$
f_6	Simplified stress-deformation curve, cf. Fig. 2.12
f_7	$E_{wu} = 1.1 E_{w\ell}$, $\frac{1}{2}(E_{w\ell} + E_{wu}) = E_w$

a time and calculating the effect on the load capacity of the finger joint. The capacity is given as the corresponding tensile strength of the member, f, being the calculated maximum load divided by the cross sectional area, i.e. $f = P/A$. The input differences for the different strength values are given in Tab. 5.2.

The calculated tensile strengths are given in Tab. 5.3, and the mean tension stress-deformation curves of the four geometries with the reference properties, f_1, are given in Fig. 5.7. With regard to the calculations, the finger joints may be divided into three strength categories, I-30 being the strongest, followed by I-15 and I-20m and with I-20 exposing the lowest tensile strength. This characterization corresponds qualitatively to what has been observed in experiments reported in the literature. However, quantitatively the correspondence is less good. This may be due to several reasons. The experimental strength values are recorded not for bond failure only, but also for a large number of tension failures due to cross-sectional reduction. In the present joints the mean stress in the panels at the finger tips, $f_1/(1-t/p)$ is 83.2, 82.9, 70.9 and 95.2, respectively and, hence, wood failure should be expected at lower levels. Furthermore, the calculated finger joints are idealized, whereas real joints often are far from perfect; e.g. *Johansson* [50] reports that the actual cross-sectional reduction of the finger joints for several manufacturers are about twice the nominal value. Hence, the calculated values should be compared to maximum tested values rather than to the means.

The boundary condition of constant vertical deformation of the horizontal sides, cf. Fig 5.4, implies that all fingers are equally stressed. In practice, for a single finger jointed panel, knots and other imperfections will involve bending and stress eccentricities in the panel. This factor may be of large significance to finger joint

Table 5.3: *Calculated tensile strength for different finger joints. The values in parentheses denote the percentage change in comparison to f_1 for each joint. The span of the recorded results represents a span of means from different recordings found in the literature [49, 50, 59, 76, 86, 102].*

Finger joint type	f_1	f_2	f_3	f_4	f_5	f_6	f_7	Recorded results
I-15	69.9	75.2 (7.6)	70.2 (0.4)	70.2 (0.4)	76.9 (10.0)	67.8 (-3.0)	67.8 (-3.0)	40-45
I-20m	70.5	75.2 (6.7)	71.0 (0.7)	71.0 (0.7)	77.6 (10.0)	68.1 (-3.4)	69.8 (-1.0)	45-50
I-20	58.1	61.7 (6.2)	58.5 (0.7)	58.5 (0.7)	63.9 (10.0)	55.9 (-3.8)	57.8 (-0.5)	30-40
I-30	81.9	85.5 (4.4)	82.9 (1.2)	83.0 (1.3)	90.1 (10.0)	80.3 (-2.0)	79.6 (-2.8)	45-50

strength and it may be assumed that a finger joint in e.g. a glulam beam will be more uniformly loaded and, hence, stronger than a single finger joint loaded in tension.

From the parametric study it is clear that strength is the predominating bond line parameter affecting finger joint strength. A 10 % bond strength increase yields an increase of 4.5-7.6 % in joint strength with the highest value for the I-15 joint. Increased fracture energy and wood stiffness give the same effect on the stress distribution in the bond line and should, hence, affect joint strength equally. The effect is, however, considerably less than for bond strength, with the lowest impact on the I-15 joint. However, for a finger joint the maximum strength is limited by the strength of the wood material, while the fracture energy theoretically may be many times that of wood. From one-dimensional theory, the normalized bond strength was given in Eq. (2.22) as a function of the brittleness number. For a symmetric joint it takes the form

$$\frac{P_{max}}{\tau_f b\ell} = \mathcal{F}\left\{ \frac{\ell^2 \tau_f^2}{E_w t G_f} \right\} \qquad (5.39)$$

Eq. (5.39) implies that a 10 % increase of the parameters τ_f, E_w and G_f will all
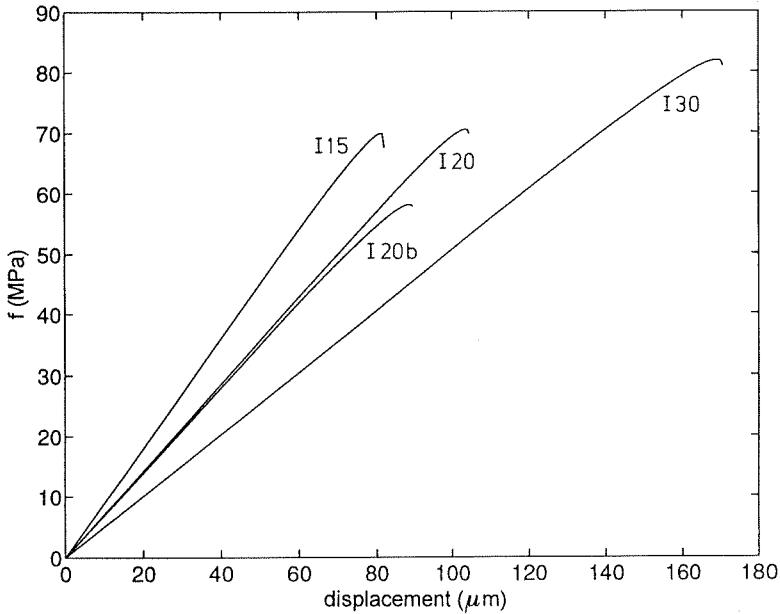
Figure 5.7: *Calculated mean tension stress versus global deformation of different finger joints.*

together give a 10 % increase of P_{max}. This is verified by calculation f_5, but the effect is not obtained by linear superposing the contributions from the separate increases of the three joint parameters. The nonlinear response already for the actual small variation of the input parameters may be due to the path dependence of the mixed mode fracture energy. At a change of a single parameter, the stiffness ratio between the bond and the wood material will change and, hence, also the ratio of τ/σ in the bond. Accordingly, a change of for instance the uniaxial bond strength will imply an increase in mixed-mode fracture energy. This effect partly explains the small influence of fracture energy to P_{max}, as an increase of G_f and E_w yields a decreased ratio of δ_s/δ_n and, hence, a mixed-mode fracture path involving lower energy consumption.

The stress distribution at the limit of the linear elastic state and at peak load is given in Fig. 5.8 for The I-30 joint. The ratio δ_s/δ_n for the outer bond dofs in the elastic state is 7.9, 6.9, 4.9 and 7.1, respectively, for the joints following the order of Tab. 5.1. In the softening region these values will increase to be approximately doubled at maximum load and for I-30 will be as high as 17 at P_{max}.

In the analysis f_6 the simplified material model of Fig. 2.12 was used, with the same magnitude of material properties as for f_1. The simplified model yields a decrease of finger joint strength in the range of 2.0-3.8 %, with the highest effect
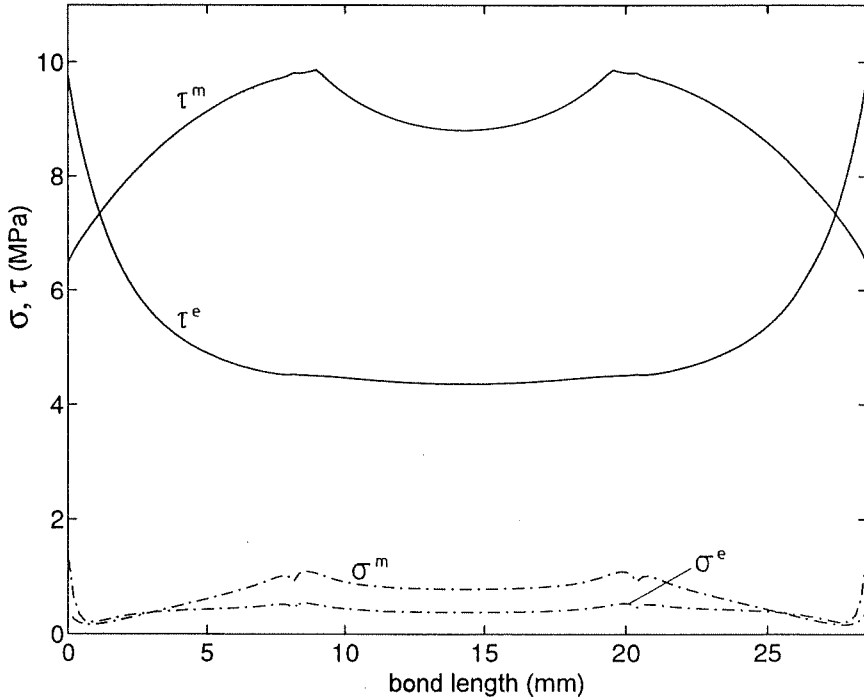
Figure 5.8: *Stress distribution along the bond line of I-30 finger joint at at the limit of the linear elastic state (e) and at maximum load (m).*

on the I-20 joint. In real finger joints the stiffness of the opposite fingers may be expected to vary. In the analysis f_7 the stiffness of the facing fingers differs 10 %, but with a mean stiffness equal to that of f_1. This difference implies a decrease of joint strength in the range of 0.5-3.0 %, which may not seem to be crucial. However, in reality such stiffness deviation may be considerable, having a large impact on the finger joint strength. In this analysis the polar symmetry is not applicable and, hence, full length fingers have been analysed.

This study has been focused on the strength properties of finger joints. However, depending on the structure where the joint is supposed to act, the stiffness properties may also be of relevance in design. A finger joint situated in an outer lamella of a glue laminated beam will mainly be stressed in tension. If the finger joint reveals low stiffness in comparison to the surrounding material, stress redistribution will occur, forcing the adjacent material to transfer a larger amount of stress. On the contrary, if the joint is stiffer, it will act as a magnet to stresses, implying failure
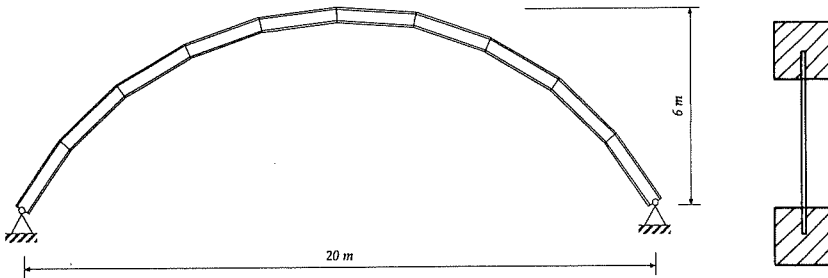
Figure 5.9: *Arch of light-weight beams.*

at relatively low global load. In comparison, a knot in the outer lamella, exposes
rather low strength but also a lower tensile stiffness and, hence, the actual stresses
acting on the knot will be moderate.

5.3.2. In-glued steel plates

Lightweight beams have obtained an increasing popularity in wood structures. One
possible application is large lightweight beam arches, illustrated in Fig. 5.9. A
project has been run at the division of Structural Mechanics at Lund University to
evaluate such structures, primarily with regard to instabilities and the joining of in-
dividual beam segments, presented in [30]. Several joint designs were evaluated. One
concept was to use steel plates glued into the wooden flanges with two-component
polyurethane (Casco 8356+1821). Tests were performed on single in-glued steel
plates of different geometries and number of steel plates loaded in tension as well as
on moment loaded full-size joints.

   Two different geometries were analysed with the present bond line model and,
for each geometry, two bond lengths were analysed, cf. Fig. 5.10. In the analysis,
symmetry was used and the 50 mm joint was modelled with 25 bond elements and a
total of 302 elements, while the corresponding numbers for the 250 mm joint were 53
and 554. A bi-linear material model was used with the parameters given in Fig. 5.11
and the coupling terms m and n are both set to 2.0. The material stiffnesses matrix,
cf. Eq. (5.22), of wood and steel were chosen to be (dimensions in MPa)

$$[D_w] = \begin{bmatrix} 13000 & 86 & 0 \\ 86 & 162 & 0 \\ 0 & 0 & 471 \end{bmatrix} ; \quad [D_s] = \begin{bmatrix} 283000 & 121000 & 0 \\ 121000 & 283000 & 0 \\ 0 & 0 & 81000 \end{bmatrix} \quad (5.40)$$

with the largest wood stiffness in the grain direction. The width of the specimens is
60 mm and the bond thickness is 0.1 mm. The loading is applied as an incremental
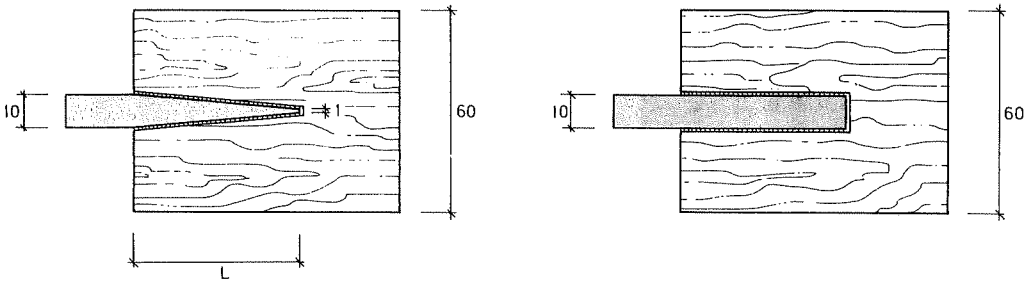
Figure 5.10: *Geometry of steel-to-wood specimens. a) Tapered joint. b) straight joint.*

displacement of the left boundary of the steel plates and the right boundary of the wood parts is prescribed to zero horizontal displacement. The right side of the steel plates is not bonded to the wood material, cf. Fig. 5.12.

The calculated load-deformation curves for the four different specimen geometries are given in Figs. 5.13 and 5.14, and the load capacity values and corresponding experimental recording values are given in Tab. 5.4. Three tests were made on each specimen and the correspondence between the calculated and recorded values for the tapered specimens is good, while for the short straight specimen there is an unsatisfactory disagreement. For all specimens the failure was located in the wood material but in a close connection to the bond line.

In Figs. 5.13 and 5.14 the stress state is all elastic below the level i. At this level the bond starts to soften at the inner end of the bond line at a load considerably lower for the straight than for the tapered joint. The point o denotes the force level at which softening also initiates at the outer end of the bond. In Figs. 5.15-5.22
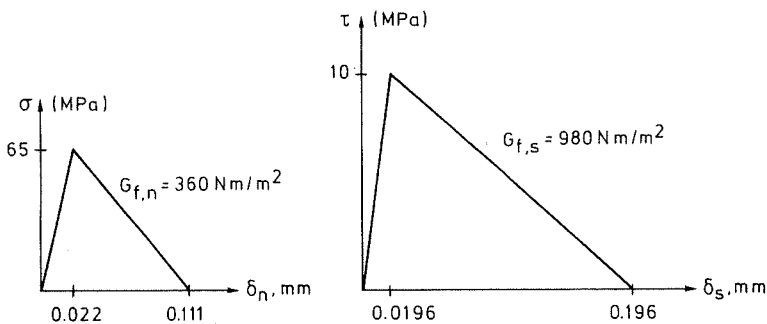
Figure 5.11: *Uniaxial bond line stress versus displacement curves of PU.*
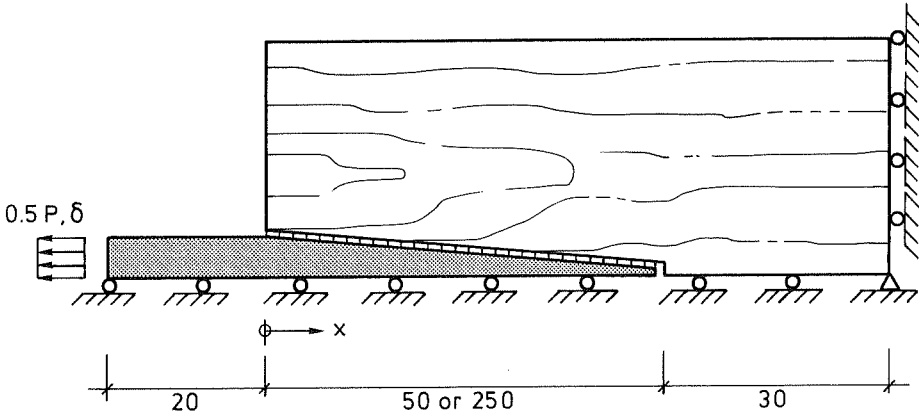
Figure 5.12: *Boundary conditions applied in the FE analysis.*

Table 5.4: *Calculated and recorded load carrying capacity of steel-to-wood joints.*

Joint shape	Joint length [mm]	Test result [kN]	Calculated result [kN]	Δ [%]
Straight	50	25.4 ± 2.7	44.5	+75
Tapered	50	50.3 ± 2.5	49.5	-2
Straight	250	119 ± 3	104	-12
Tapered	250	129 ± 6	130	+1

Figure 5.13: *Calculated load versus slip of steel-to-wood 50 mm joints.*
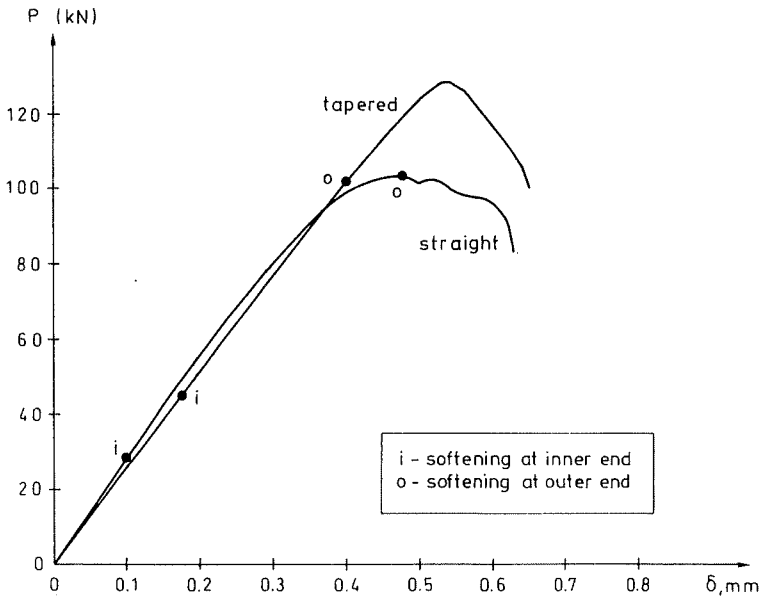
Figure 5.14: *Calculated load versus slip of steel-to-wood 250 mm joints.*

the stress distributions at the maximum elastic state, i, and at the maximum load level are given for the joints involved. The stress distribution at maximum load, in e.g. Fig. 5.14, where the softening has propagated from both sides, illustratively exhibits the coupling effect of the mixed-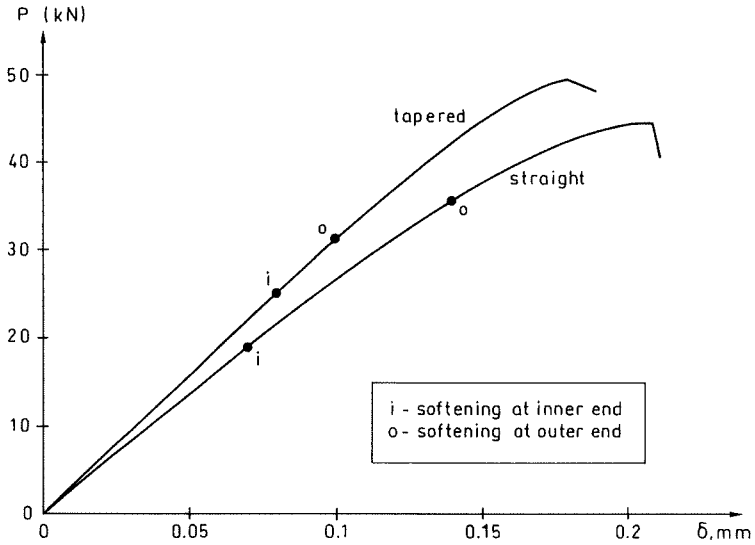mode model. The maximum shear stress is considerably higher to the right, where the peel stress is close to zero, in comparison to the left side where σ and τ are in the same range.

The compressive normal stresses at the inner bond end are considerably higher for the straight specimen. The mixed-mode model does not include σ-τ coupling at compressive normal stresses. This limitation may to some extent explain the difference between calculated and recorded maximum load capacity of the straight and tapered 50 mm specimens. In reality the softening will presumably initiate at a load level even lower than that indicated in Fig. 5.13.
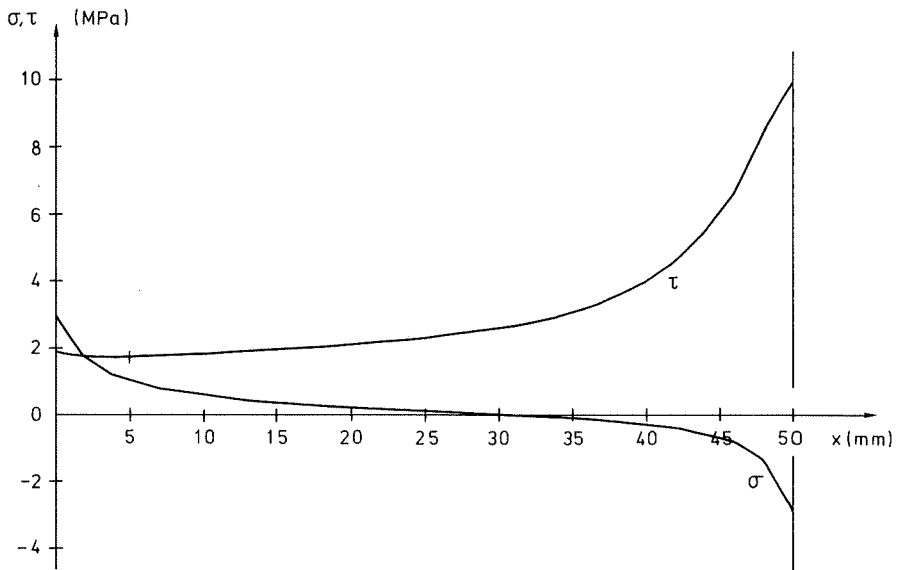
Figure 5.15: *Linear elastic stress state of straight 50 mm steel-to-wood specimen,* $P = 18.9$ *kN,* $\delta = 0.07$ *mm.*

Figure 5.16: *Stress state at maximum load of straight 50 mm steel-to-wood specimen,* $P = 44.5$ *kN,* $\delta = 0.21$ *mm.*

Figure 5.17: *Linear elastic stress state of tapered 50 mm steel-to-wood specimen,* $P = 24.9$ *kN,* $\delta = 0.08$ *mm.*

Figure 5.18: *Stress state at maximum load of tapered 50 mm steel-to-wood specimen,* $P = 49.5$ *kN,* $\delta = 0.18$ *mm.*

Figure 5.19: *Linear elastic stress state of straight 250 mm steel-to-wood specimen,* $P = 28.6$ *kN,* $\delta = 0.10$ *mm.*

Figure 5.20: *Stress state at maximum load of straight 250 mm steel-to-wood specimen,* $P = 104$ *kN,* $\delta = 0.4$ *mm.*
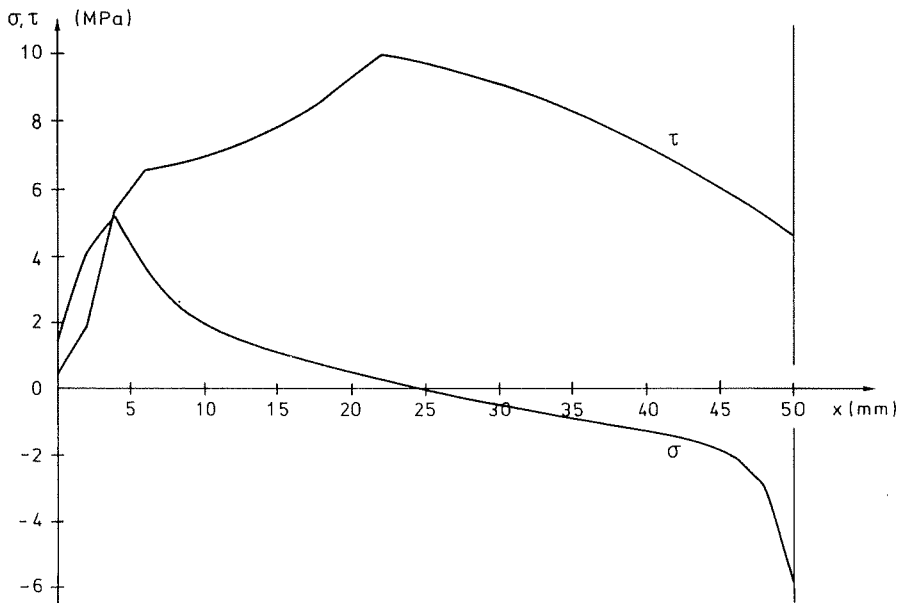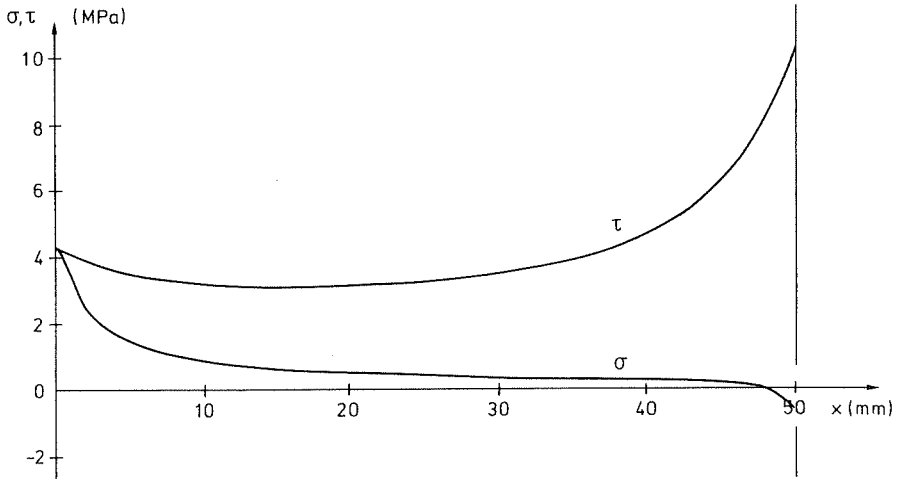
Figure 5.21: *Linear elastic stress state of tapered 250 mm steel-to-wood specimen,*
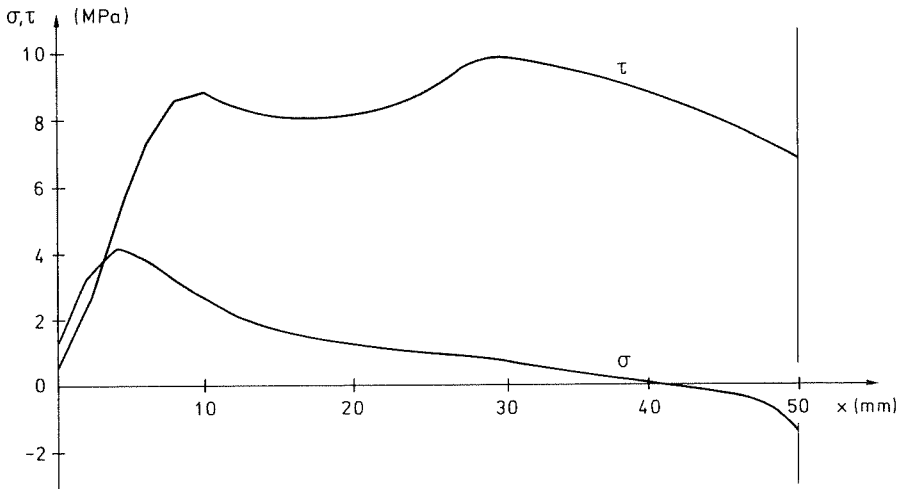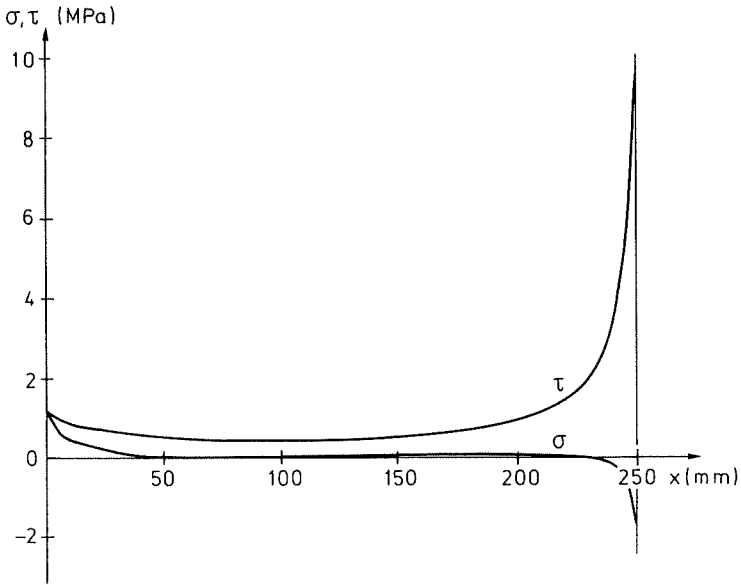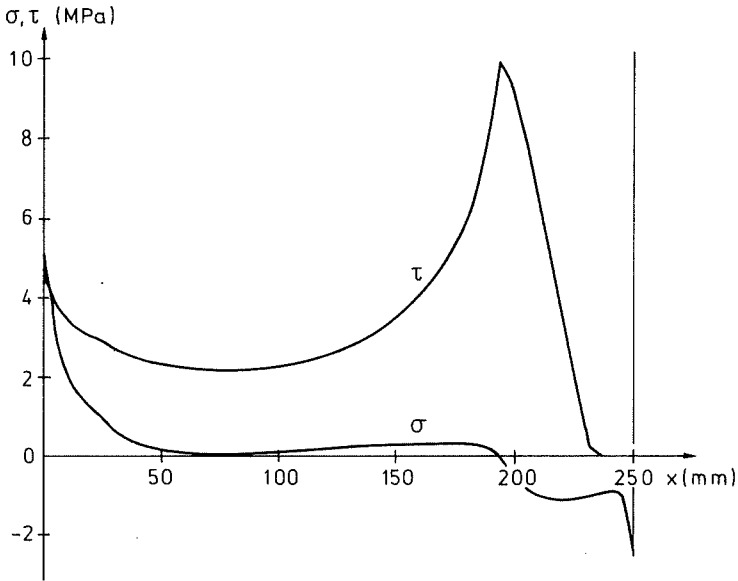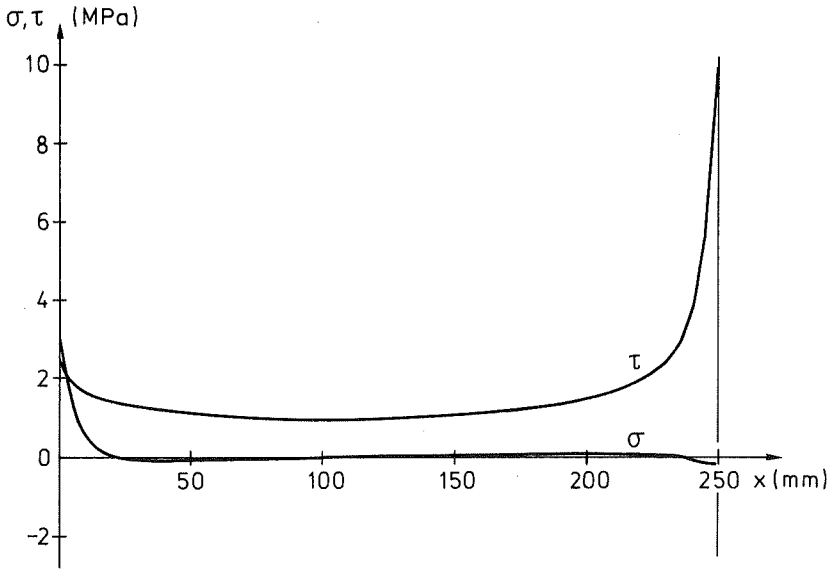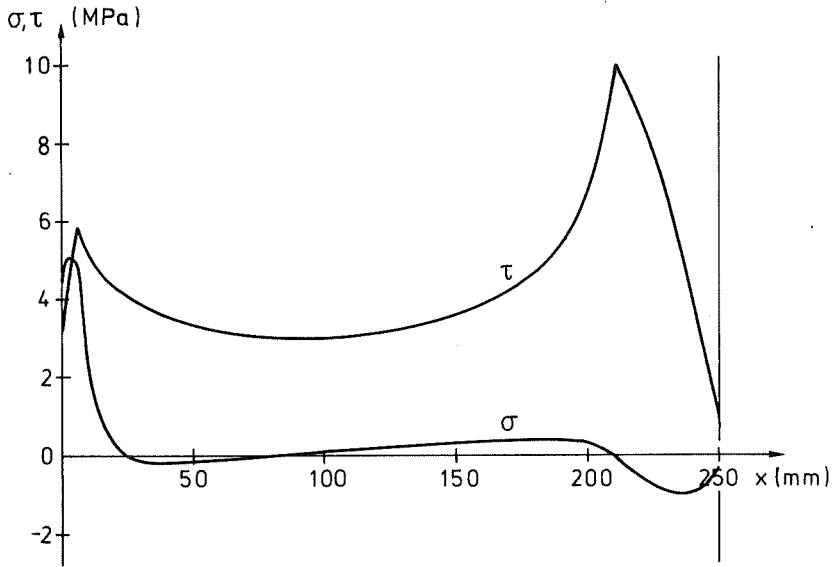$P = 45.6$ *kN,* $\delta = 0.175$ *mm.*

Figure 5.22: *Stress state at maximum load of tapered 250 mm steel-to-wood specimen,*
$P = 130$ *kN,* $\delta = 0.540$ *mm.*

6. CONCLUDING REMARKS AND DISCUSSION

6.1. Concluding remarks

6.1.1. General discussion

Adhesive bonding will most likely be a component of increasing importance in future development of wooden structural products and building concepts. However, to promote such development, adhesive bonding should be considered as high technological, demanding skilled design and craftsmanship. It is possible to produce adhesives with a large span of mechanical properties, still retaining sufficient resistance to long-term climatic effects, by modifying existing adhesives, e.g. rubber modified resorcinol [33], or by developing new adhesives.

The fabrication of adhesive bonds has to be done under controlled circumstances. Preferably structural bonds are made indoors in industries of wood components, prefabricated housing, etc. However, adhesive bonding at building sites has a large potential, as it would be beneficial from material saving and also from working environmental aspects. To facilitate such bonding, efforts must be invested in professional training as well as development of better-adapted adhesives.

With an accurate choice of adhesive, the bond may serve not only as a rigid connector but, in many situations also as a reinforcement, since a proper adhesive may provide increased fracture toughness to a bonded component. General design of adhesive joints should be made with regard to local strength as well as fracture energy. It may, however, be expounded that for many wooden joints, some measure of fracture energy rather than local strength is of major significance in joint design.

6.1.2. Summary and conclusions

A general objective of the present study has been to deepen the knowledge in the fields of adhesive joint design and bond line testing and, hence, to provide more realistic and accurate approaches for design of adhesive joints. The main topics have been to develop methods for general analysis of adhesive joints, with regard to a nonlinear fracture mechanics approach, and to develop and evaluate test methods to resolve the associated properties of wooden adhesive bond lines.

One-dimensional analysis such as Volkersen theory is appealing through its rather simple expressions and easily accessible solutions. The modification of Volkersen theory to include fracture energy and to involve adherend bending effects, proposed in this report, will improve the accuracy and widen the field of application

of this rather plain approach. However, for most regular joints, the stresses are indisputably in a mixed-mode state, which must be accounted for if a more accurate analysis is required.

Two main approaches are predominant in strength analysis of adhesive joints. Maximum stress analysis is applicable for tough joints while linear elastic fracture mechanics is relevant for brittle joints. For joints that can be considered as neither tough nor brittle, these methods often fail in the prediction of joint strength. The non-linear fracture mechanics approach, proposed in the present study, is a unified theory involving stress analysis and linear fracture mechanics as special cases. Hence, arbitrary joints can be analysed, and the properties strength and fracture energy, respectively, will affect the load capacity of the joint in relation to the brittleness of the joint. The brittleness is quantified as a brittleness ratio comprising the strength and fracture energy of the bond line, the stiffness of the adherends, and the geometric size and shape of the joint. For very tough joints, joint strength will only be proportional to the local strength of the bond line and the analysis will correspond to maximum stress analysis. For brittle joints, on the contrary, the single bond property to affect the load carrying capacity of the joint is fracture energy, and the analysis will agree with that of linear elastic fracture mechanics. In the case of joints of intermediate brittleness, the strength of the joint will not only be influenced by bond line strength and fracture energy, but also by the shape of the stress-deformation curve of the bond line material. It may also be argued that the local bond line properties are of great consequence to global joint load capacity, also at wood failure. Furthermore, it may be concluded that for many joints, optimal strength can be expected if the local failure process occurs in the bond line.

A *mixed-mode bond line model* is presented in this report. It is a two-dimensional expansion of the previously recorded uniaxial stress-deformation relations. The model is defined in a deformation space; the two stress components σ and τ are both described as functions of the corresponding deformations δ_n and δ_s. The concept is that the known $\tau - \delta_s$ relation will be reduced as the normal opening deformation, δ_n, increases and vice versa for the $\sigma - \delta_n$ relation. In other words, the coupling effect implies that the strength and the deformation capacity in shear decreases when the normal deformation increases, and contrariwise for the normal components. No failure criterion for normal compression is, however, included. The normal stresses are assumed to behave linear elastically in the compressive state. The model is path independent concerning stresses, but path dependent in the description of fracture energy.

There is a variety of more or less *standardized test methods* to be employed on adhesive joints. In general, these methods do not generate reliable material properties to be used in design of glued components. Tests are often of qualitative nature, to vouch for some minimum or relative strength of the tested specimens, commonly applied after some accelerated climatic exposure. In the present study three standard methods have been discussed. The CEN prEN 302 shear specimen was found to be proper for determination of local shear strength, but not applicable for record-

ings of fracture energy. For the ASTM D-905 shear specimen, the transformation from recorded load to shear strength is complicated and the result will be affected by other specimen properties than local shear strength. The evaluation of the DCB cleavage specimen is associated with large embroilments. Depending on the chosen method of evaluation, the estimated fracture energy or energy release rate will vary considerably. A major problem of all testing of wooden bonds, which is pronounced for tension testing, is the appearance of wood failure, implying that the resolved material properties will be a mixture of adhesive and wood characteristics.

New test methods are proposed in the present study for direct testing of material properties and for verification as well as for fracture mechanics testing. The small size material testing methods aim at determining the complete stress-deformation curves of bond lines, in pure shear, pure tension and at mixed-mode stress states. Hence, the local shear stress, fracture energy, and the shape of the stress-deformation curve can be determined in one single test. The concept is to use small specimens with a uniform and univocal stress state, tested in a stiff closed-loop testing machine with fast response which will facilitate stable test performance also during gradual softening. The presented methods are not suited for determination of initial Young's and shear modulus of the bond material. However, the linear elastic deformations are concluded to be of minor importance in joint design.

The verification test specimens are larger, including a nonuniform stress state which implies a propagating failure. For shorter specimens the maximum load capacity will be a function of local shear stress as well as fracture energy, while for sufficiently long joints the only significant bond line property is fracture energy.

As a major outcome from the test programme, it is concluded that wood adhesive bonds expose gradual softening, and with the proposed test methods it is possible to record this property.

Except for the small shear tests, the tests were carried out at certain constant climates and deformation rates. The test programme does not consider long-term effects such as creep and durability. Accordingly, the material properties presented in the report are valid for the given testing conditions and should be generalized except with a large portion of care. The adhesives involved in the test programme are activated through different chemical and physical principles and, consequently, they may be expected to exhibit diverse responses to exposure of long-term load, humidity, etc. Of the adhesives used, only resorcinol/phenol is, in most countries, accepted for outdoor structural use.

In the *small shear specimen test* programme, small scale investigations was performed to evaluate the effect of varying test conditions on the material properties of the tested bonds. The conditions included were rate of deformation, curing time, bond line thickness and content of formaldehyde. Decreased deformation rate tends to cause decreased bond strength and, for resorcinol/phenol and polyurethane, also decreased fracture energy, G_f, and bond line brittleness ratio, τ_f^2/G_f. Increased curing time, from 4 to 16 days, makes resorcinol/phenol bond lines somewhat more brittle, while the polyurethane and PVAc bonds are affected only to a minor ex-

tent. Increased bond line thickness does not have any significant influence on resorcinol/phenol, while for polyurethane the effect is severe due to improper curing conditions of the small specimens.

Bond line shear strengths are in the magnitude of 5-10 MPa and the fracture energies in shear are in the range of 1 kNm/m^2. The recorded slip transformed into corresponding mean strains indicates that the strain at peak stress is in the range of 100 % for some adhesives and, in general, the strains are several hundred percent when the shear stress capacity is completely expended.

The small shear specimen test may be considered to be a proper method for determination of the complete stress-slip curves for regular wooden bond lines in pure shear. Possibly, the wood volume of the specimen could be decreased to improve the stiffness of the setup and, hence, increase the probability of stable performance when testing brittle adhesives. In addition, the procedure of applying curing pressure on sensitive adhesives, such as polyurethane, should be improved. This can possibly be achieved by gluing larger sheets of wood, thus reducing the edge effects.

The *small tension specimen test* programme proved to be well adapted for determination of the complete stress-deformation curves of wooden bond lines in tension perpendicular to the bond line. Due to the low strength of pine perpendicular to grain, beech was chosen as adherend material.

The characteristic shape of the $\sigma - \delta_n$ curves is similar to the corresponding curves recorded in shear, but the magnitudes are lower over all. For the given test condition, the resorcinol/phenol exhibits bond strength, σ_f, of approximately 6 MPa, and fracture energy, $G_{f,I}$, of about 0.3 kNm/m^2. The polyurethane bonds revealed considerably lower values. Again, this is most likely due to improper curing pressure, which is emphasized by the less gluable beech surface.

The *small mixed-mode specimen test* programme involved tests on resorcinol/phenol and PVAc bonds and pure wood. Tests were made for different combinations of displacement rates in the $\delta_n - \delta_s$ field. The unique testing machine used in the test series was in a development phase, which implied some problems e.g. with noisy signals. However, stable stress-deformation curves have been determined for different mixed-modities. Resorcinol/phenol and wood expose similar characteristics, while PVAc may be characterized as more ductile, with large fracture energy in shear dominated failure.

From the presented stress-deformation curves, bond parameters strength and fracture energy are determined and compared to a failure criteria. Wood and resorcinol/phenol adopts a quadratic failure criterion, while PVAc reveals a better fit when the power on the normal stress component is set to be linear. Total fracture energy for wood and resorcinol/phenol is in a large span approximately independent of the mixed-mode angle. For large angles with predominating shear failure, the fracture energy exhibits a rapid increase. Also for PVAc, the total fracture energy increases rapidly as the mixed-modity converges toward pure mode-II, but the $G_f - \psi_G$ curve is more rounded, with a tendency of a minimum in the mixed-mode region.

The *large specimen shear test* programme was applied to two different types of adhesives, polyurethane and resorcinol/phenol, and for three different lengths, 25, 100 and 400 mm. The constitutive relations of resorcinol/phenol bonds obtained in the small specimen tests were verified by the tests. Good correspondence was obtained between calculated and experimental results, not only for the maximum load capacity but also for the slip performance. At bond length exceeding a good 100 mm, peak load carrying capacity is reached and the failure process will continue at increasing deformation but at constant load. The single bond parameter of significance is fracture energy, G_f, and, accordingly, sufficiently long specimens may serve as a method for determination of fracture energy of brittle adhesives.

For polyurethane specimens the conformity to the small specimen test was poor. This is, however, due to the dissimilar curing conditions for the small and the large specimens. A backwards evaluation of the large specimen results suggests that the strength is approximately 50 % higher and the fracture energy is almost 5 times as large, for the polyurethane bonds in the large specimens in comparison to that of the small specimens.

The *large specimen tension test, DCB,* programme is not well adapted for testing strong and brittle wood adhesive bonds. The recorded load-displacement curves are difficult to interpret; depending on the method of evaluation, the obtained fracture energy or energy release rate varies by as much as a factor of 3. One of the reasons is the partial wood failures, implying that the effective fracture energy changes during the propagation of the failure process. In addition, evaluation in accordance to linear fracture mechanics implies that the fracture zone is of zero size; digression from this assumption will have a large effect on the acquired energy release rate.

The *large specimen mixed-mode test, MMB,* programme, like the DCB specimen, suffers from the occurrence of wood failure. The amount of wood failure increases as the mode-I component becomes more dominant. Accordingly, testing in a span from pure mode-II to pure mode-I, the recorded fracture energy will increasingly be influenced by the wood perpendicular to grain properties and, in addition, wood failure often yields increased fracture surface which will imply that the fracture energy is overestimated.

Aside from the problems associated with wood failure, the MMB specimen may very well prove to be appropriate for sufficiently weak adhesives or for adherend materials for which the material properties vouch for the failure process to take place along the bond line.

The mixed-mode model has been implemented into the finite element code CALFEM, and several verifications and applications have been analysed. A parametric study of *finger joints* reveals that local strength is the bond line property of major significance. However, local bond strength has an upper limit at the strength of the wood material, while the fracture energy may be considerably increased, provided that bond failure is obtained. Four different finger joint geometries in the span 15-30 mm of finger length were analysed. The calculated load capacity was largest for the joint with 30 mm finger length. The rank of the different geometries

corresponds well to experimental values found in the literature. Analysis of straight and tapered in-glued steel plates in wood panels reveals good correspondence to test results except for a case where large compressive stresses occurred in the fracture zone.

As a major conclusion it is found relevant to consider the complete stress-deformation curve of bond lines in joint design. It is, furthermore, possible to record such curves with the test methods proposed in this study. The bond line has been considered as a layer, including the adhesive and the outer layer of the adjacent wood material. This assumption has advantages from an analysis point of view since the strains in the bond are replaced by relative displacements, and it also simplifies the evaluation of the test results.

6.2. Future Research Needs

The general objective of this report has been to apply non-linear fracture mechanics to wood adhesive joint design. The non-linear fracture mechanics approach facilitates arbitrary bonds, tough or brittle, being analysed in a unified manner. The methods of analysis developed are focused on short term behaviour and monotonic loading, not taking into account properties such as durability, creep and effects of unloading and fatigue. Durability is seldom included in analysis; instead it is accounted for by accelerated climatic tests which aim at guaranteeing a sufficient long-term behaviour. A common long-term test is to examine the long term strength of adhesive joints [56, 62], which may give qualitatively valuable information. Decreased long-term load capacity may be caused by material degradation and/or creep in the adhesive and the adherend material. The degradation is a matter of great importance but should be a task for chemists rather than structural engineers.

Creep may occur in the bonds as well as in the wood material. Creep may be beneficial as well as having a severe effect on joint strength. A small amount of bond line creep, in a sufficiently long joint, may entail reduced stress concentrations and, hence, increased joint strength. If, however, the creep mainly occurs in the adherends, the effect most likely will be the opposite. A common and rather simple approach to considering creep is to reduce the elastic modulus of the material. From this approach a reduction of stiffness does not necessarily imply reduced fracture energy and, consequently, not in the load carrying capacity of brittle joints either. However, decreased adherend stiffness will imply decreased load capacity of brittle joints, in accordance to the limit equations, $P_{max} \sim \sqrt{EG_f}$, in Fig. 2.14.

The mixed-mode model seems appropriate for analysis of adhesive joints. However, further studies should be performed on possible coupling effects on the compressive side. The model presumes that the softening initiates simultaneously in shear and in tension. Tests on wood in mixed-mode reveal that this assumption violates the true behaviour of wood. However, it is straightforward according to the mixed-mode modell to assume hardening in one direction during softening in the

other. This topic should be studied to determine the applicability of the model on the analysis of wood failure.

To increase the generality of the model it can be improved to account for nonelastic behaviour such as plastic dissipation and damage. This modification of the model is quite straightforward and the corresponding tests are also possible to perform on the testing machines used in this study.

In the present study an analysis, including a parametric study, of finger joint strength was performed. Finger joints are considered to be crucial components of glued laminated beams. For the global strength of glulam beams it is, however, not only finger joint strength that is of concern; the stiffness properties are also significant. A stiff finger joint will act as a magnet to stresses, implying large stress concentrations in the joint, while a softer finger joint will redistribute the stresses to the surrounding material.

As a first step in development of a composite model of a glue laminated beam, the global stiffness and strength of the finger joint may be established. These properties may be adopted into a finite element description, which can be used in an FE model of a full-size glulam beam. Correspondingly, a similar description may be performed for a knot. Hence, the influence of knots, finger joints, wood property deviations, etc., may be evaluated. This topic is of great consequence in the development of improved and more reliable glulam structures.

BIBLIOGRAPHY

[1] Adams R.D., Wake W.C. (1984), *Structural Adhesive Joints in Engineering.* Elsevier Applied Science Publisher Ltd., Barkling, U.K.

[2] Aicher S., Klöck W., *Finger Joint Analysis and Optimization by Elastic, Nonlinear and Fracture Mechanics Finite Element Computation.* Proc. 1991 International Timber Engineering Conference, Trada, vol 3, pp 3.66-76, London, U.K. (1991)

[3] Andersson G.P., Bennet S.J. and DeVries K.L. (1977), *Analysis and Testing of Adhesive Bonds.* Academic Press Inc, London, U.K.

[4] Aronsson C.-G., *Tensile Fracture of Composite Laminates with Holes and Cracks.* Report No 84-5, Royal Institute of Technology, Department of Aeronautical Structures and materials, Stockholm, Sweden 1984.

[5] Ashizawa M., *Fast Interlaminar Fracture of a Compressively Loaded Composite Containing a Defect.* 5th DoD/NASA Conf. Fibrous Composites in Structural Design, Naval Air Development Center, Report 81-096-60, New Orleans, LA, USA (1981).

[6] Bao G., Ho S., Suo Z. and Fan B., *The Role of Material Orthotropy in Fracture Specimens for Composites.* Int. J. Solid Structures, vol 29, no. 99, pp 1105-1116 (1992).

[7] Barak S., *FEM-Analysis of a Test Specimen for Shear Loaded Wood Adhesive Joints.* Master thesis. Report TVSM-5036, Lund University, Division of Structural Mechanics, Lund, Sweden 1990. (In Swedish).

[8] Bigwood D.A. Crocombe A.D., *Elastic Analysis and Engineering Design Formulae for Bonded Joints.* Int. J. Adhesion and Adhesives, vol 9, pp 229-242 (1989).

[9] Bigwood D.A. Crocombe A.D., *Non-Linear Adhesive Bonded Joint Design Analysis.* Int. J. Adhesion and Adhesives, vol 10, pp 31-41 (1990).

[10] Bleich F. (1924), *Theorie und Berechnung der Eisernen Brücken.* Verlag von Julius Springer, Berlin, Germany.

147

[11] Bodig J., Jayne B.A. (1982), *Mechanics of Wood and Wood Composites*. Van Nostrand Reinhold, New York, NY, USA.

[12] Boström L., *Method for Determination of the Softening Behaviour of Wood and Applicability of a Nonlinear Fracture Mechanics Model*. Report TVBM-1012, Lund University, Division of Building Materials, Lund, Sweden 1992.

[13] Bradley W.L. *Relationship of Matrix Toughness to Interlaminar Fracture Toughness*, in: Friedrich K. (ed), *Application of Fracture Mechanics to Composite Materials*. Elsevier Science Publishers B.V. (1989).

[14] de Bruyne N.A., *The Strength of Glued Joints*. Aircraft Engineering, pp 114-118, April (1944).

[15] Chai H., *Experimental Evaluation of Mixed-mode Fracture in Adhesive Bonds*. Experimental Mechanics, pp 296-303, Dec. (1992).

[16] Chai Y.S., *Interfacial Crack Initiation under Biaxial Loading*. EMRL Report No. 90/1, University of Texas at Austin, TX, USA 1990.

[17] Charalambides P.G., Lund J., Evans A.G., McMeeking R.M., *A Test Specimen for Determining Fracture Resistance of Bimaterial Interfaces*. J. Applied Mechanics, vol 56, pp 77-82 (1989).

[18] Charalambides P.G., Cao H.C., Lund J., Evans A.G., *Development of a Test Method for Measuring the Mixed Mode Fracture Resistance of Bimaterial Interfaces*. Mechanics of Materials, vol 8, pp 269-283 (1990).

[19] Chow S., *Adhesive Developments in Forest Products*. Wood Science and Technology, vol 17, pp 1-11 (1983).

[20] Colling F., *Tragfähigkeit von Biegeträgen aus Brettschichtholz in Abhängigkeit von den Festigkeitsrelevanten Einflußgrößen*. 4.Folge -Heft 22, Versuchsanstalt für Stahl, Holz und Steine der Universität Fridericiana in Karlsruhe, Germany 1990.

[21] Crocombe A.D., *Global Yielding as a Failure Criterion for Bonded Joints*. Int. J. Adhesion and Adhesives, vol 9, pp 145-153 (1989).

[22] Dahlblom O., Peterson, A., *CAMFEM - Computer Aided Modelling based on the Finite Element Method*. Report TVSM-3001, Lund University, Division of Structural Mechanics, Lund, Sweden 1982.

[23] Dahlblom O., Peterson, A., Petersson H., *Manual for CALFEM - a Program for Computer Aided Learning of the Finite Element Method, version 85*. Report TVSM-3007, Lund University, Division of Structural Mechanics, Lund, Sweden 1986.

[24] Dahlblom O., *Constitutive Modelling and Finite Element Analysis of Concrete Structures with Regard to Environmental Influence.* Report TVSM-1004, Lund University, Division of Structural Mechanics, Lund, Sweden 1987.

[25] Davis P., Benzeggagh M.L., *Interlaminar Mode-I Fracture Testing*, in: Friedrich K. (ed), *Application of Fracture Mechanics to Composite Materials.* Elsevier Science Publishers B.V. (1989).

[26] Desai C.S., Siriwardane H.J. (1984), *Constitutive Laws for Engineering Materials with Emphasis on Geologic Materials.* Prentice Hall, Englewood Cliffs, NJ.

[27] Edlund U., *Mechanical Analysis of Adhesive Joints: Models and Computational Methods.* Linköping Studies in Science and Technology. Dissertation no. 291, Linköping University, Department of Mechanical Engineering, Linköping, Sweden 1992.

[28] Ehlbeck J., Colling F., *Bending Strength of Finger Joints.* Proc. of IUFRO 5.02, Wood Engineering Group, St. John, NB, Canada (1990).

[29] Enquist B., *Testing of Fracture Properties of some Different Wood Adhesive Bonds.* Report TVSM-7062, Lund University, Division of Structural Mechanics, Lund, Sweden 1991. (In Swedish).

[30] Enquist B., Serrano E., *Arched Frames Built Up of Straight Wood Composite I-Beams.* Report TVSM-7087, Lund University, Division of Structural Mechanics, Lund, Sweden 1994. (In Swedish). Division of Structural Mechanics, Lund, Sweden 1993.

[31] Evans R.H., Marathe M.S., *Microcracking and Stress-Strain Curves for Concrete in Tension.* Matériaux et Constructions, no 1, pp 61-64 (1968).

[32] Fleck N.A., Hutchinson J.W., Suo Z., *Crack Path Selection in a Brittle Adhesive Layer.* Int. J. Solid Structures, vol 27, pp 1683-1703 (1991).

[33] Freidin A. S., *Perspective Adhesives and Protective Coatings for Wood Structures.* Paper 22-18-1, Proceedings of the CIB-W18A, Meeting 22, Berlin, GDR (1989).

[34] Glos P., Horstmann H., *Design of Glued Joints.* 1991 International Timber Engineering Conference, Trada, vol 3, pp 3.77-3.84, London, U.K. (1991).

[35] Goth H., Radović B., *Undersuchungen zur Keilzinkenverleimung von Holz mit Höheren Holzfeuchten als 15 % mit Einkomponenten-Polyurethanklebstoffen.* Forschungsbericht I,4-35847, FMPA Baden-Württenberg, Otto-Graf-Institute, Germany 1990.

[36] Groth H.L., *Analysis of Adhesive Joints.* Report No 87-17, Royal Institute of Technology, Department of Aeronautical Structures and Materials, Stockholm, Sweden 1987.

[37] Groth H.L., *Viscoelastic and Viscoplastic Stress Analysis of Adhesive Joints.* Int. J. Adhesion and Adhesives, vol 10, pp 207-213 (1991).

[38] Gustafsson P.J., *Fracture Mechanics Studies of Non-Yielding Materials such as Concrete.* Report TVBM-1007, Lund University, Division of Building Materials, Lund, Sweden 1985.

[39] Gustafsson P.J., *Analysis of Generalized Volkersen-Joints in Terms of Non-Linear Fracture Mechanics,* in: Verchery G., Cardon A.H.(ed), *Mechanical Behaviour of Adhesive Joints.* Edition Pluralis, Paris, France (1987).

[40] Gustafsson P.J., Enquist B., *Strength of Wood Beams with a Sharp Notch.* Report TVSM-7042, Lund University, Division of Structural Mechanics, Lund, Sweden 1988. (In Swedish).

[41] Hart-Smith L.J., *Stress Analysis: a Continuum Mechanics Approach,* in: Kinloch A.J. (ed), *Developments in Adhesives-2.* Applied Science Publishers, London (1981).

[42] He M.Y., Cao H.C., Evans A.G., *Mixed-Mode Fracture: The Four Point Shear Specimen.* Acta Metal. Mater., vol 38, pp 839-846 (1990).

[43] Hellan K. (1984), *Introduction to Fracture Mechanics.* McGraw-Hill International Edition, Singapore.

[44] Hillerborg A., Modéer M., Petersson P.E., *Analysis of Crack Formation and Crack Growth in Concrete by means of Fracture Mechanics and Finite Elements.* Cement and Concrete Research, vol 6, pp 773-782 (1976).

[45] Hong C.S., Yoon S.H., Kim H.J., *Mixed Mode Interlaminar Fracture of Laminated Composite Using Modified End-Notched Flexure Specimen.* Proc. 9th Int. Conf. on Experimental Mechanics, Copenhagen, Denmark (1990).

[46] Hu G.K., *Etude Theorique et Experimentale du Comportement, de L'endommagement et de la Rupture des Assemblages Colles.* Dissertation, Ecole Central Paris, LMSS/MAT URA 850, France 1991.

[47] Hu G.K., François D., Schmit F., *Non Linear Fracture Mechanics for Adhesive Lap Joints.* Journal of Adhesion, vol 37, pp 261-269 (1992).

[48] Jensen H.M., Hutchinson J.W., Kim K.S., *Decohesion of a Cut Prestressed Film on a Substrate.* Int. J. Solid Structures, vol 26, pp 1099-1114 (1990).

[49] Johansson C.-J., *Strength of Finger Joints for Glued Laminated Timber.* Report SP-RAPP 1983:10, Statens Provningsanstalt, Borås, Sweden 1983. (In Swedish).

[50] Johansson C.-J., *Strength of Finger Joints for Glued Laminated Timber.* Teknisk Rapport 1986:09, Statens Provningsanstalt, Borås, Sweden 1986. (In Swedish).

[51] Kanninen M.F., *A Dynamic Analysis of Unstable Crack Propagation and Arrest in the DCB Test Specimen.* Int. J. Fracture, vol 10, pp 415-430 (1974).

[52] Kaplan W. (1981), *Advanced Mathematics for Engineers.* Addison-Wesley Publishing Company, Inc., Philippines.

[53] Kinloch A.J. (1987), *Adhesion and Adhesives. Science and Technology.* Chapman and Hall, U.K.

[54] Knott J.F. (1973), *Fundamentals of Fracture Mechanics.* Butterworth, London, U.K.

[55] Komatsu K., Sasaki H., Maku T., *Estimating Fracture Toughness from Nonlinear Load-Deflection Relation.* Wood Research, no 61, pp 25-43 (1974).

[56] Kreibich R.E., Freeman H.G., *Effect of Specimen Stressing upon Durability of Eight Wood Adhesives.* Forest Production Journal, vol 20, no 4, pp 44-49 (1970).

[57] Krenk S., *Energy Release Rate of Symmetric Adhesive Joints.* Engineering Fracture Mechanics, vol. 43, pp 549-559 (1992).

[58] Kyokong B.,Keenan F.J., Boyd S.J., *Fracture Behaviour of Adhesive Joints in Poplar.* Wood and Fiber Science, vol 18, pp 499-525 (1986).

[59] Larsen H.J., *Strength of Finger Joints.* Report IFB/A 8002, Institute of Building Technology and Structural Engineering, Aalborg University, Denmark 1980.

[60] Liu Y., Chen K., *A Two-Dimensional Mesh Generator for Variable Order Triangular and Rectangular Elements.* Computers & Structures, vol 29, pp 1033-1053 (1988).

[61] Lotter R.E., Santare M.H., *Analysis of Mode I and Mode II Interlaminar Fracture Specimens by a Comparative Finite Element Method.* Composite Science and Technology, vol. 40, pp 87-107 (1991).

[62] Lundgren S. Å., *New Structural Gluing.* Report R85:1985, Swedish Council for Building Research, Stockholm, Sweden, 1985. (In Swedish).

[63] Magnusson B., Petersson H., *GENFEM-S, a Computer Program for Nonlinear Dynamic Analysis of Panel Structures by the Finite Element Method.* Publication 1983:16, Chalmers University of Technology, Division of Structural Design, Göteborg, Sweden 1983.

[64] Mall S., Murphy J.F., Shottafer J.E., *Criterion for Mixed Mode Fracture in Wood.* J. Engineering Mechanics, vol 109, pp 680-690 (1983).

[65] *MATLAB - High-Performance Numerical Computation and Visualization Software.* The MathWorks Inc, Natick, Ma, USA 1992.

[66] *Maple V.* Waterloo Maple Publishing, Waterloo, Ontario, Canada, 1992.

[67] Mostovoy S., Crosley P.B., Ripling E.J., *Use of Crack-Line-Loaded Specimen for Measuring Plane-Strain Fracture Toughness.* Journal of Materials, vol 2, pp 661-681 (1967).

[68] Ottosen N.S., Olsson K.G., *Hardening/Softening Plastic Analysis of an Adhesive Joint.* Journal of Engineering Mechanics, ASCE, vol 114, pp 97-116 (1988).

[69] Ottosen N.S., Petersson H. (1992), *Introduction to the Finite Element Method.* Prentice Hall, U.K.

[70] Paris P.C., *Fracture Mechanics in the Elastic-Plastic Regime.* ASTM STP 631, Flaw Growth and Fracture, pp 3-27 (1977).

[71] Petersson H., *On Design Criteria for Tension Perpendicular to Grain.* International Council for Building Research, Working Comision W18 - Timber Structures, CIB-W18/25-6-4, Åhus, Sweden 1992.

[72] Petersson P.E., *Crack Growth and Development of Fracture Zones in Plane Concrete and Similar Materials.* Report TVBM-1006, Lund University, Division of Building Materials, Lund, Sweden 1981.

[73] Popov E.P. (1978), *Mechanics of Materials.* Prentice/Hall Inc., Englewood Cliffs, NJ, USA.

[74] Qu Z., Fan C., *Tensile Strenth of Glued Finger Joints in Timber Structure and Recommendation for Their Series.* Proc. of 1988 International Conference on Timber Engineering, vol 1, pp 654-662, Seattle, Wa (1988).

[75] Rabiej R.J., Behm H.D., *The Effect of Clamping Pressure and Orthotropic Wood Structure on Strength of Glued Bonds.* Wood and Fiber Science, vol 24, pp 260-273, (1992).

[76] Radović B., Rohlfing H., *Untersuchungen über die Festigkeit von Keilzinkenverbindungen mit Unterschiedlichem Verschwächungsgrad.* Forschungsbericht I,4-34701, FMPA Baden-Württenberg, Otto-Graf-Institute, Germany 1986.

[77] Raknes E. (1987), *Wood Gluing, 2nd edition.* Universitetsforlaget, Oslo, Norway, (In Norwegian).

[78] Reeder J.R., Crews Jr J.H., *Mixed-Mode Bending Method for Delamination Testing.* AIAA Journal, vol 28, pp 1270-1276 (1990).

[79] Riberholt H., Enquist B., Gustafsson P.J., Jensen R.B., *Timber Beams Notched at the Support.* Report TVSM-7071, Lund University, Division of Structural Mechanics, Lund, Sweden 1992.

[80] Rice J.R., *A Path Independent Integral and the Approximate Analysis of Strain Concentration by Notches and Cracks.* Journal of Applied Mechanics, vol 35, pp 379-386 (1968).

[81] River B.H., Okkonen E.A., *A Contoured Wood Double Cantilever Beam Specimen for Adhesive Joint Fracture Test.* To be published in J. Testing and Evaluation.

[82] Roy S., Reddy J.N., Brinson H.F., *Geometric and Viscoelastic Nonlinear Analysis of Adhesive Joints,* in: Verchery G., Cardon A.H.(ed), *Mechanical Behaviour of Adhesive Joints.* Edition Pluralis, Paris, France (1987).

[83] Russel A.J., Street K.N., *Delamination and Debonding of Materials,* in: Johnson W.S (ed), *ASTM STP 937,* pp 349-370 (1985).

[84] Schellekens J.C.J., *Computational Strategies for Composite Structures.* Dissertation, Delft University of Technology, Faculty of Civil Engineering, Delft, The Netherlands, 1992.

[85] Scott C.T., River B.H., *Fracture Testing Wood Adhesive with Composite Cantilever Beams.* To be published in J. Testing and Evaluation.

[86] Selbo M.L., *Effect of Geometry on Tensile Strength of Finger Joints.* Forest Production Journal, sept 1963, pp 390-400 (1963).

[87] Sih G., Paris P.C., Irwin G.R., *On Cracks in Rectilinearly Anisotropic Bodies.* Int. J. of Fracture Mechanics vol 1, pp 189-203 (1965).

[88] Stigh U., *Initiation and Growth of an Interface Crack,* in: Verchery G., Cardon A.H.(ed), *Mechanical Behaviour of Adhesive Joints.* Edition Pluralis, Paris, France (1987).

[89] Stricklin J.A., Haisler W.E., von Riesemann W.A., *Evaluation of Solution Procedures for Material and/or Geometrically Nonlinear Structural Analysis.* AIAA Journal, vol. 11, pp. 292-299 (1973).

[90] Suo Z., *Delamination Specimen for Orthotropic Materials.* J. of Applied Mechanics, vol 57, pp 627-634 (1990).

[91] Suzuki N., Sasaki H., *Fracture of Notched Wooden Beams with Glue Lines.* Mokazai Gakkaishi, vol 33, pp 121-130 (1987).

[92] Ungsuwarungsri T., Knauss W.G., *The Role of Damage-Softened Material Behaviour in the Fracture of Composites and Adhesives.* International Journal of Fracture, vol 35, pp 221-241 (1987).

[93] Valentin G.H., Boström L., Gustafsson P.J., Ranta-Maunus A., Gowda S., *Application of Fracture Mechanics to Timber Structures RILEM State-of-the-Art Report.* Technical Research Center of Finland, Research notes 1262, Espoo, Finland (1991).

[94] Volkersen O., *Die Nietkraftverteilung in Zugsbeanspruchten Nietverbindungen mit Konstanten Laschenquerschnitten.* Luftfahrtforschung, vol 35, pp 41-47 (1938).

[95] Wang J.S., Suo Z., *Experimental Determination of Interfacial Toughness Curves using Brazil-Nut-Sandwiches.* Acta Metal. Mater., vol 38, pp 1279-1290 (1990).

[96] Wernersson H., Gustafsson P.J., *The Complete Stress-Slip Curve of Wood-Adhesives in Pure Shear*, in: Verchery G., Cardon A.H.(ed), *Mechanical Behaviour of Adhesive Joints.* Edition Pluralis, Paris, France (1987).

[97] Wernersson H., *Fracture Characterization of Wood Adhesive Joints.* Proc. 1991 International Timber Engineering Conference, Trada, vol 3, London, U.K., pp 3.383-3.390 (1991).

[98] Wernersson H., *Wood Adhesive Bonds - Fracture Softening Properties in Shear and in Tension,* Report TVSM-3012, Lund University, Division of Structural Mechanics, Lund, Sweden 1990.

[99] Williams J.G., Birch M.W., *Mixed Mode Fracture in Anisotropic Media.* ASTM STP 601, Cracks and Fracture, pp 125-137 (1976).

[100] Woo C.W., Chow C.L., *Mixed Mode Fracture in Orthotropic Media*, in: Sih G.C., Valluri S.R. (ed), *Fracture Mechanics in Engineering Application.* Sijthoff and Noordhoff, Rockville (1979).

[101] Wu E.M. *Application of Fracture Mechanics to Anisotropic Plates.* ASME J. of Applied Mechanics, vol 34, pp 967-974 (1967).

[102] Youngquist J.A., Laufenberg T.L., Bryant B.S., *End Jointing of Laminated Veneer Lumber for Structural Use.* Forest Production Journal, vol 34, no 11/12, pp 25-32 (1984).

[103] Yuuki R., Chung N.Y., Ishikawa, H., Nakano S., *Mixed-Mode Fracture Criteria on Adhesive Joints*. J. Soc. Mat. Japan, vol 39, pp 1095-1100 (1990).

[104] Zienkiewicz O.C., Taylor R.C. (1989), *The Finite Element Method, fourth edition*. McGraw-Hill, U.K.